

OPTICAL PROPERTIES AND ENCODING OF INFORMATION OF NONLINEAR AND ACTIVE PLASMONIC METASURFACES

Dissertation

zur Erlangung des akademischen Titels

doctor rerum naturalium

(Dr. rer. nat.)

vorgelegt

der Fakultät für Naturwissenschaften der Universität Paderborn

von Dipl. phys. Felicitas Walter

geboren am 19. Dezember 1986 in Lahr/Schwarzwald

ERKLÄRUNG DER SELBSTSTÄNDIGKEIT

Hiermit versichere ich die vorliegende Arbeit selbstständig verfasst und keine anderen als die angegebenen Quellen und Hilfsmittel verwendet, sowie Zitate deutlich kenntlich gemacht zu haben.

Paderborn, den

Felicitas Walter

ABSTRACT

Metasurfaces made of plasmonic nano antennas offer a great variety of applications in optics and photonics, as they can operate in the linear and nonlinear regime. In this work, metasurfaces with different purposes are investigated.

Plasmonic nanoantennas can influence nonlinear generation with different properties. Caused by the localized surface plasmon polaritons, they generate a high electric near field when illuminated with their resonance frequency. This can be used to enhance nonlinear generation processes in already nonlinear media, e.g. zinc oxide. It is shown that a second nanoantenna that is resonant at the nonlinear signal wavelength can increase this enhancement even further. Depending on their rotational symmetry, plasmonic antennas are even capable of generating their own nonlinear signal under illumination with circularly polarized light. Measurements on antennas with a five-fold symmetry are shown, as they are supposed to generate a fourth harmonic signal. A generated nonlinear signal by nano antennas can also convert a PIN diode into an infrared detector, as the second harmonic generation lies within the current generating band gap.

Another feature of plasmonic metasurfaces is their ability to change the phase of the incoming light. Two different forms of this phase variation are investigated. With the variation by resonances and the right material system it is possible to fabricate a metasurface that is able to generate two different holograms depending on the surrounding medium of the sample. The Pancharatnam-Berry phase, which also exist in the nonlinear regime, enables a metasurface that encodes an image that can only be read out in the nonlinear as the intensity of this signal can be varied locally.

KURZFASSUNG

Metaoberflächen, die aus plasmonischen Nanoantennen bestehen, können für viele verschiedene Anwendungen der Optik und Photonik verwendet werden, da sie sowohl im lineare als auch im nichtlinearen Bereich eingesetzt werden können. Dieser Arbeit untersucht Metaoberflächen mit verschiedenen Anwendungszwecken.

Plasmonische Nanoantennen können nichtlineare Prozesse durch verschiedene ihrer vielen Eigenschaften beeinflussen. Durch lokalisierte Oberflächenplasmonen, können sie unter Bestrahlung mit Licht ihrer Resonanzfrequenz ein hohes elektrisches Nahfeld erzeugen. Dadurch werden nichtlineare Prozesse in schon nichtlinearen Medien wie z.B. Zinkoxid erhöht. Es wird gezeigt, dass eine zweite Antenne, die an der Wellenlänge des nichtlinearen Signals resonant ist, diese Erhöhung noch weiter verstärkt. Abhängig von ihrer Rotationssymmetrie können plasmonische Nanoantennen auch selbst nichtlineare Signale erzeugen, wenn sie mit zirkular polarisiertem Licht bestrahlt werden. Es werden Messungen an Antennen mit einer fünfzähligen Symmetrie gezeigt, da diese ein Signal der vierten Harmonischen erzeugen sollen. Ein von Nanoantennen generiertes nichtlineares Signal kann auch dazu genutzt werden, eine PIN-Diode in einen Infrarotdetektor umzufunktionieren, da die zweite Harmonische innerhalb der stromerzeugenden Bandlücke liegt.

Eine weitere Eigenschaft plasmonischer Metaoberflächen ist die Fähigkeit die Phase des einfallenden Lichtes zu verändern. Es werden zwei verschiedene Arten dieser Phasen Anpassung untersucht. Mit der Variation über Resonanzen wird gezeigt, dass abhängig vom Materialsystem auch Metaoberflächen gefertigt werden könne, die abhängig vom Umgebungsmedium der Probe zwei verschiedene Hologramme erzeugen. Mit Hilfe der Pancharatnam-Berry Phase, die auch im Nichtlinearen existiert, kann eine Metaoberfläche realisiert werden, die ein Bild kodiert, das nur im Nichtlinearen ausgelesen werden kann, da die Intensität dieses Signals lokal veränderbar ist.

CONTENT

ERKLÄRUNG DER SELBSTSTÄNDIGKEIT.....	i
ABSTRACT	iii
KURZFASSUNG	iv
CONTENT	v
1 Introduction.....	1
2 Plasmonic nanoantennas and their nonlinear behavior	4
2.1 Plasmonics	4
2.1.1 Electromagnetism in metals.....	4
2.1.1.1 Maxwell equations	4
2.1.1.2 Dielectric function of the electron gas	5
2.1.1.3 Dielectric function of gold	7
2.1.2 Localized surface plasmon polaritons	8
2.1.3 Plasmonic field enhancement.....	11
2.2 Nonlinear plasmonics	15
2.2.1 Nonlinear optical effects	15
2.2.2 Optical parametric oscillator.....	16
2.2.3 Basic nonlinear plasmonic concepts	18
2.2.3.1 Enhanced nonlinear effects with structured plasmonic surfaces	18
2.3 Double resonant plasmonic nanoantennas.....	20
2.3.1 Experiment	20
2.3.2 Short conclusion.....	24
2.4 Nanoantennas on PIN-diodes.....	26
2.4.1 Working principle of PIN diodes with plasmonic nano antennas	26
2.4.2 Experiment	27
2.4.3 Discussion of results.....	34
2.5 Nonlinear selection rules.....	35
2.5.1 Fabrication	40
2.5.2 Fourier-transform infrared spectroscopy	41
2.5.3 Linear measurements.....	43
2.5.4 Nonlinear measurements.....	44
2.5.5 Discussion of results.....	47
3 Optical phase control with Metasurfaces	49

3.1	Phase manipulation with resonances	49
3.1.1	Switchable phase holography with hybrid v-shaped nanoantennas.....	51
3.1.2	Discussion of results	60
3.2	Pancharatnam-Berry phase	62
3.2.1	Linear P-B phase	62
3.2.2	Nonlinear P-B phase	63
3.2.3	Nonlinear optical image encoding.....	65
3.2.3.1	Experiment	67
3.2.3.2	Discussion of results.....	71
4	Conclusion.....	73
5	References	75
6	List of figures.....	80
7	List of tables	86
8	List of scientific contributions	87
	Danksagung.....	88

1 INTRODUCTION

In comparison to conventional optical components that rely on the light to propagate over distances much longer than the wavelength, metasurfaces provide a two dimensional alternative. These are very thin surfaces consisting of nanostructures with subwavelength dimensions. They can be made from different materials, dielectric or metallic. Here we want to concentrate on metallic or so-called plasmonic nanostructures. They serve different purposes as well and can work in either the linear or the nonlinear regime. In this work, various metasurfaces are investigated. Some use the strong near field enhancement of plasmonic nanoantennas and others the ability to modulate the phase of the incoming light as desired.

Plasmonic effects arise from the interaction of the electrons in metal with light. The conducting electrons near the surface can be excited to oscillate coherently. In the case of metal nanoparticles or structures localized surface plasmons arise, whose resonances depend on shape and size. These resonances result in a strong electromagnetic near field enhancement [Nov11, Zay05]. A very prominent example that relies on this near field enhancement is the surface enhanced Raman spectroscopy. Here plasmonic resonances enable the enhancement of the rather weak Raman scattering process by several orders of magnitude. This makes even single molecule detection possible [Sha12]. This strong near field can also be used for the enhancement of nonlinear optical effects. It is possible to enhance the harmonic generation in nonlinear materials such as in multi quantum wells by several orders [Lee14]. One part of this work concentrates on harmonic generation and its enhancement by plasmonic structures. Depending on the symmetry of the nanoparticles, they are even able to generate nonlinear harmonics themselves.

Metasurfaces offer a great variety of possible applications. In the following work, diverse properties of these surfaces are utilized to realize different tasks. The first part deals with the near field enhancement of plasmonic nanoantennas, which is used for two different applications. In one application, the antennas are used to create a second harmonic generation signal, which is used to generate a current in a PIN diode that works in the visible regime. This results in the use of the PIN diode as an infrared detector. Another experiment investigates the advantage of double resonant antennas compared to single dipole antennas. Those antennas consist of two, one long and one short antenna, which are resonant at the exciting and the second harmonic wavelength, respectively. As they are placed on a zinc oxide sample, which is highly nonlinear itself, the strong electric near field of the antenna is aimed to enhance the second harmonic generation. Furthermore, the small antenna shall help in out coupling the generated nonlinear light again.

Depending on the rotational symmetry of the plasmonic antennas, they can generate harmonic signals themselves. For example it has been shown that three-fold (C3) symmetric antennas, generate second harmonic, whereas a four-fold symmetry (C4) generates third harmonic signals [Che14b, Li15]. To generate fourth harmonic signals, a

sample with five-fold symmetric (C5) antennas has been fabricated. As the harmonic generation processes do not only depend on the symmetry on the microscopic level of the antennas, but also on the macroscopic symmetry of the antennas' arrangement, two different arrangements are investigated.

Next to the near field enhancement and the nonlinear generation, the ability of metasurfaces to modify the phase, amplitude and polarization of an incoming wavefront is of high interest and investigated in this work, as well. Conventional optical components work by refraction, diffraction, and absorption of light. The manipulation of the light is accomplished by passing through these components with a distinctive refractive index. This leads to a long propagation distance over which the changes of phase, amplitude, and polarization are accumulated. The main distinction of metasurfaces to such conventional components is the distance over which the wavefront shaping is accomplished, as they introduce abrupt changes to the optical properties [Yu11, Ni12]. For metasurfaces, this distance is even shorter than the wavelength of the incoming beam, which is reflected or transmitted by the metasurface.

These features of metasurfaces and the ability to even exhibit electromagnetic properties that cannot be found in nature lead to many applications, such as invisible cloaks [Sch06, Liu09], metalenses [Che12] or holograms [Che14a, Lar12, Zhe15]. This is achieved by engineering the interaction of light with the metasurfaces' nanoantennas. For many applications it is necessary to be able to have complete phase control over the range from 0 to 2π . This can be acquired by using the geometric Pancharatnam-Berry phase, which relies on the inversion of the electric field rotation [Pan56]. For transmission, this equals the inversion of the circular polarization state, whereas for reflection it remains the same. This technique enables a localized antenna-orientation controlled phase. Phases can also be modulated via different optical scatterers that cause phase discontinuities at interfaces between two different materials. This phase change can be explained by the generalized laws of refraction and reflection, which describe the behavior of phase and amplitude of light at interfaces.

The second part of this work deals with such phase modulating metasurfaces. As it is even possible to fabricate active metasurfaces that behave differently depending on their surrounding atmosphere, a metasurface is fabricated that is aimed to generate two different holograms. Magnesium for example reacts to magnesium hydride, while residing in a hydrogen atmosphere [Bal09]. Therefore, it then behaves like a dielectric and loses its plasmonic properties. If now the antennas of a metasurface consist of two metals, one that does react with hydrogen and one that does not, the metasurface provides different results for different surrounding atmospheres, as the acquired phase changes depend on the active part of the antennas. The described application is an active hologram that generates two different images for an air and a hydrogen atmosphere.

Furthermore, the geometric Pancharatnam-Berry phase that exists in the nonlinear regime as well is used for nonlinear optical encoding. It is possible to create metasurfaces

that control the amplitude, phase or polarization of the harmonic generation light signal. On this basis, nonlinear optical spin interactions and holography have been realized [Ye16a, Ye16b]. In both cases, linear and nonlinear, holography requires complex encoding algorithms and furthermore elaborate read-out techniques of the Fourier plane [Hua13, Mat04, Alm16]. Another form of optical encryption, as what holography can be seen as, is gray scale image encoding of the nonlinear harmonic light. This can be achieved by manipulating the interference of the harmonic generation light signals of two neighboring nanoantennas. Spatially variant nonlinear signals can be accomplished by locally controlling the phase of these two antennas. The generated harmonic signals of these two antennas interfere and depending on their rotation angle, the phase is adjusted. These phases then lead to a locally tunable intensity of the second harmonic signal, which can be used to encode messages into metasurfaces, whose signal can only be read out in the nonlinear regime.

2 PLASMONIC NANOANTENNAS AND THEIR NONLINEAR BEHAVIOR

2.1 PLASMONICS

As in the following work all investigated structures are based on plasmonic nanoantennas, it is of importance to fully understand their functionality. To be able to do this, one needs to look into some fundamentals of electrodynamics first.

2.1.1 Electromagnetism in metals

2.1.1.1 *Maxwell equations*

In the classical case, the interaction of electromagnetic fields can be described by the Maxwell equations. They describe the development in time and space of electromagnetic fields in matter in the presence of charges and currents.

The density of charge carriers in metals is quite high and, therefore, many densely staggered energy levels exist. In comparison to the thermal excitation energy $k_B T$ at room temperature, they have very small distances. Due to this, the classical theory described by Maxwell's equations can be used even for metals with very small features in the nanometer regime.

It makes sense to distinguish between external fields and fields that are generated by matter itself. The total charge density ρ_{tot} and current density \vec{J}_{tot} therefore consist of an external and an internal part and hence [Mar10]

$$\rho_{tot} = \rho_{ext} + \rho_{int} \quad (2.1)$$

$$\vec{J}_{tot} = \vec{J}_{ext} + \vec{J}_{int} \quad (2.2)$$

In their differential form the Maxwell equations (that is how they can be found in most textbooks e.g. [Jac99]), connect the external charge density ρ_{ext} and the external current density \vec{J}_{ext} with their macroscopic quantities such as the electric field \vec{E} , the electric displacement field \vec{D} , the magnetic field \vec{H} and the magnetic induction \vec{B} .

$$\nabla \cdot \vec{D} = \rho_{ext} \quad (2.3)$$

$$\nabla \cdot \vec{B} = 0 \quad (2.4)$$

$$\nabla \times \vec{E} = -\frac{\partial \vec{B}}{\partial t} \quad (2.5)$$

$$\nabla \times \vec{H} = \vec{J}_{ext} + \frac{\partial \vec{D}}{\partial t} \quad (2.6)$$

Furthermore the polarization \vec{P} , which describes the electric dipole moment in unit volume, and the magnetization \vec{M} can be used to characterize those field units.

$$\vec{D} = \varepsilon_0 \vec{E} + \vec{P} \quad (2.7)$$

$$\vec{H} = \mu_0^{-1} \vec{B} - \vec{M} \quad (2.8)$$

with ε_0 as the electric permittivity and μ_0 as the magnetic field constant. Since the polarization \vec{P} results of microscopic dipoles, which are induced by the electric field, it is proportional to them and can be expressed by

$$\vec{P} = \varepsilon_0 \chi \vec{E} \quad (2.9)$$

Putting this into equation (2.7) results in

$$\vec{D} = \varepsilon_0 \varepsilon \vec{E} \quad (2.10)$$

with ε as the relative permittivity and $\varepsilon = 1 + \chi$ applies.

ε defines the response of the material to electromagnetic fields and is generally independent of fields as well as of position and direction. However, it is frequency dependent. Considering a harmonic time dependent field with a frequency ω the relative permittivity can be expressed as a complex function of this frequency:

$$\varepsilon(\omega) = \varepsilon_r(\omega) + i\varepsilon_i(\omega) \quad (2.11)$$

with ε_r as the real part and ε_i as the imaginary part of the dielectric function.

2.1.1.2 Dielectric function of the electron gas

As the following work deals with the interaction of metals and light, the optical properties of metals are of high interest. Describing those properties the model of the free electron gas, especially the Drude-Sommerfeld model is an appropriate approach [Dru00]. Unfortunately, for noble metals at higher frequencies this approach is only limitedly valid (see 2.1.1.3). In the Drude-Sommerfeld model, a certain amount α of the electrons can be described as a free, non-interacting gas. There exists a constant potential background due to the positively charged atomic cores. However, the details of the lattice potential can be neglected. Due to collisions the movement of the electrons is damped. The collision rate can be expressed by $\gamma = \tau^{-1}$. After a collision, the electron loses all information about its former state of motion and in between those collisions, it is accelerated in

direction of the electric field. Therefore the motion equation for an electron in a free electron gas is [Mai07]

$$m_{eff}\ddot{\vec{x}} + m_{eff}\gamma\dot{\vec{x}} = -e\vec{E} \quad (2.12)$$

with m_{eff} as the effective mass of the electron and e as its elementary charge.

Under the assumption of an alternating electric field $\vec{E}(t) = \vec{E}_0 \exp(-i\omega t)$ with the frequency ω the approach of $\vec{x} = \vec{x}_0 \exp(-i\omega t)$ leads to the following solution of the differential equation

$$\vec{x}(t) = \frac{e}{m_{eff}(\omega^2 + i\gamma\omega)} \vec{E}(t) \quad (2.13)$$

By applying an electric field the electrons are deflected and generate a macroscopic polarization, which can be expressed as

$$\vec{P} = -ne\vec{x} = -\frac{ne}{m_{eff}(\omega^2 + i\gamma\omega)} \vec{E}(t) \quad (2.14)$$

with the real part of the charge density n . The electrons oscillate around the atomic cores with the so called plasma frequency ω_p which is defined by

$$\omega_p = \sqrt{\frac{ne^2}{\epsilon_0 m_{eff}}} \quad (2.15)$$

Putting equation (2.14) into equation (2.7) and using the definition of the plasma frequency (2.15) leads to the following formula for the electric displacement field

$$\vec{D} = \epsilon_0 \left(1 - \frac{\omega_p^2}{\omega^2 + i\gamma\omega} \right) \vec{E} \quad (2.16)$$

Comparing this with equation (2.10), one gains the dielectric function for a free electron gas

$$\epsilon(\omega) = 1 - \frac{\omega_p^2}{\omega^2 + i\gamma\omega} \quad (2.17)$$

Considering different frequency regions, one can check the validity of this model in regards of noble metals. If $\omega < \omega_p$ the response of the medium is given primarily by the electrons of the s-band, whereas the fully filled d-band near the fermi energy heavily polarizes its surrounding. Even under the consideration of the positively charged atomic cores, a residual polarization remains. A combination of both effects can be described by an additional polarization term

$$\vec{P}_\infty = \epsilon_0(\epsilon_\infty - 1)\vec{E} \text{ with } 1 \leq \epsilon_\infty \leq 10 \quad (2.18)$$

Adding this term to equation (2.7), the electric displacement field can be expressed by

$$\vec{D} = \epsilon_0 \vec{E} + \vec{P} + \epsilon_0(\epsilon_\infty - 1)\vec{E} \quad (2.19)$$

Here one has to keep in mind that \vec{P} stands for the polarization generated by the free electrons. For noble metals this results in

$$\epsilon(\omega) = \epsilon_\infty - \frac{\omega_p^2}{\omega^2 + i\gamma\omega} \quad (2.20)$$

2.1.1.3 Dielectric function of gold

As in this work nearly all plasmonic structures consist of gold, we will discuss the dielectric function of gold a bit more in detail. For a wide range, the description of the free electron gas is a good approximation for noble metals such as gold, silver and copper. The shape of their conduction band comes very close to the parable of free electrons. However, there exist intraband transitions in noble metals. These are transitions of electrons from filled bands below the fermi level into higher bands. Figure 2.1 shows the experimentally determined dielectric function of gold, silver and copper [Joh72]. By identifying the energy with the highest slope for ϵ_2 (the imaginary part of the dielectric function), it is possible to determine the energy, where the intraband transitions start. For gold and copper this is at around 2,5 eV, which equals a wavelength of approximately 500 nm and for silver around 4 eV, which equals approximately 300 nm. Therefore, silver has the advantage that it can be described by the Drude-Sommerfeld model in the complete visible optical range.

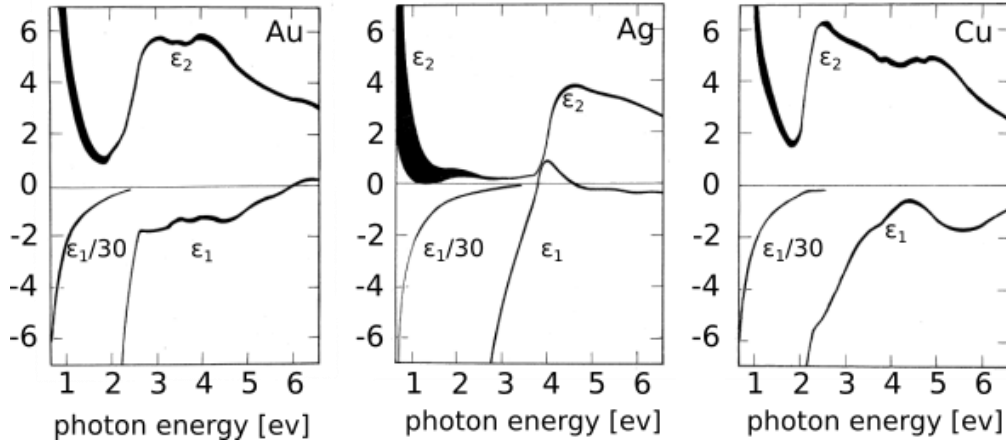


Figure 2.1: Imaginary ϵ_2 and real part ϵ_1 of the dielectric function of gold, silver and copper [Joh72.]

Figure 2.2 shows the calculated dielectric functions of gold in the Drude model compared to experimentally found data [Via05]. It is obvious that above 1,8 eV the Drude model does not describe the actual function anymore. Furthermore, it shows the calculations in the Drude-Sommerfeld model, where the motion equation (2.12) gets an additional term $m_{eff}\omega_0^2\vec{x}$, which describes the bound electrons [Mai07].

$$m_{eff}\ddot{\vec{x}} + m_{eff}\gamma\dot{\vec{x}} + m_{eff}\omega_0^2\vec{x} = -e\vec{E} \quad (2.21)$$

This describes the actual behavior far better than the Drude model, but for lower photon energies than 1,8 eV the Drude model is still a good approximation.

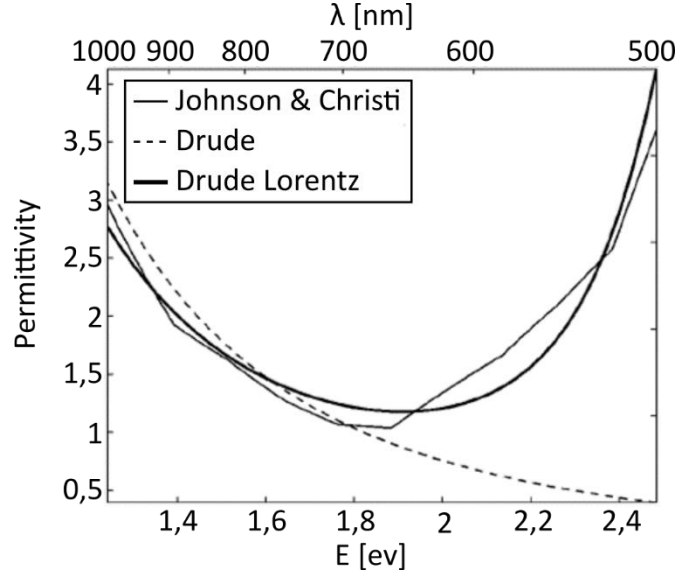


Figure 2.2: Dielectric function of gold, calculated with the Drude-Sommerfeld model and the Drude model and experimental data(Johnson & Christi) [Via05].

2.1.2 Localized surface plasmon polaritons

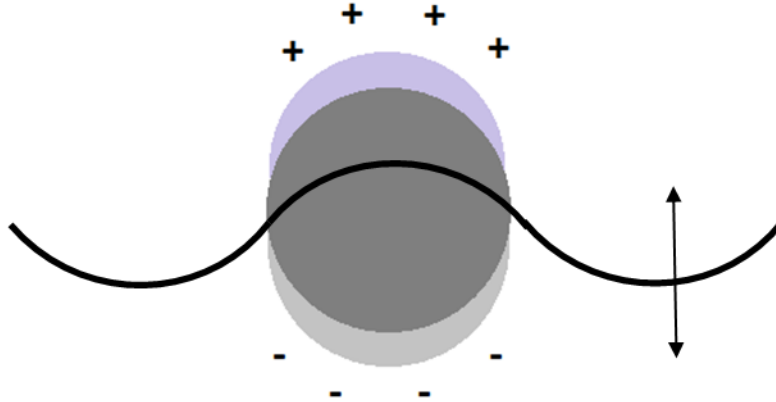


Figure 2.3: Schematic figure of excitation of LSPP.

With the descriptions of noble metals from above, it is now possible to describe plasmonic behavior. Surface plasmon polaritons (SPP) and localized surface plasmon polaritons (LSPP) are electromagnetic excitations, which can be generated by coupling of electromagnetic fields to oscillations of the free electron density in metals. Opposite to the SPP, which propagate in the metal as waves, the LSPP are localized at a nanoparticle. As in this work only LSPP are of interest, we concentrate on the description on their

behavior. The LSPP are generated by excitation of electron oscillations. The electrons are deflected out of their idle position, which leads to a recoiling force. The resulting resonance of the excitation is called localized surface plasmon resonance (LSPR).

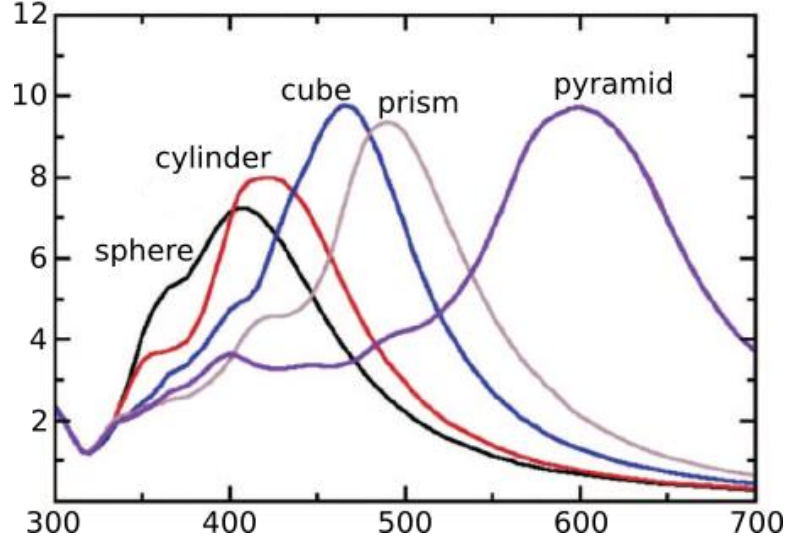


Figure 2.4: Dependence of the resonance to the form of a silver nanoparticle in vacuum. Every particle has got the same volume, in which the sphere has a diameter of 50 nm [Hae05].

For perfect spheres this resonance can be calculated exactly with the Mie theory [Mie08]. Under the assumption that the diameter d of the nanosphere is much smaller than the wavelength of light λ in the surrounding medium, the electromagnetic field around the nanoparticle can be considered static, as the phase over the complete volume of the structure is basically constant. With a constant electric field, the local field distribution can now be calculated. The resulting displacement of the conducting electrons regarding the ion lattice leads to a surface charge, which results in a recoiling force (see Figure 2.3). By exciting the electrons with their eigenfrequency, the resulting field enhancement can be maximized. This frequency depends on the strength of the recoiling force, which depends on the distance of the surface charges. That is why it is basically determined by the size and form of the nanoparticle. After the Mie theory the extinction cross section $F(\lambda)$ of a nanoparticle in relation to the wavelength λ of the exciting electromagnetic wave is given by [Wil07]

$$\varepsilon F(\lambda) = \frac{24\pi^2 N_A a^3 \varepsilon_m^{3/2}}{\lambda \ln(10)} \cdot \frac{\varepsilon_i}{(\varepsilon_r + \chi \varepsilon_m)^2 + \varepsilon_i^2} \quad (2.22)$$

Here ε_i and ε_r stand for the imaginary and real part of the dielectric function of the nanoparticle's material respectively. ε_m is the dielectric number of the nanoparticle's surrounding medium, N_A is the surface density of the nanoparticle and a its diameter. χ is a form dependent parameter, which can only be solved analytically for spheres and rotational ellipsoids. For every other form, it has to be approximated. In the case of a sphere, it is 1 but it can have values up until 20, which is the case for particles with a high

aspect ratio. Figure 2.4 shows the resonances for different nanoparticle forms that all have the same volume as a sphere with a diameter of 50 nm [Hae05].

The diameter of the nanoparticle defines the lifetime of LSPP. One differs between three different sizes, very small nanostructures with $a \lesssim 10$ nm, medium sized structures with $10 \text{ nm} < a < 100$ nm and big structures with $a \gtrsim 100$ nm. This differentiation has to be done, as for big structures the quasi-static approach is not valid anymore, because the electromagnetic field cannot be seen as constant over the complete structure. This leads to retardation effects. For really small structures, which are much smaller than the mean free path of electrons (30-50 nm), additional effects need to be taken into account.

First, we take a look on medium sized and big structures. Here two competing damping processes occur, the radiating and the absorbing one. The bigger the structure, the more important is the radiative damping process, where collective oscillations of the electron density decay into photons. Furthermore, electron hole pairs are generated by intraband transitions in the conducting band or by interband transitions from the energetically low lying d-bands into the sp-band. This leads to absorbing damping processes, which lose importance for bigger structures.

Using the dephasing time T_2 , which is given by

$$\frac{1}{T_2} = \frac{1}{2T_1} + \frac{1}{T_2^*} \quad (2.23)$$

(with T_1 as the decaying time through radiating as well as not radiating processes and T_2^* as the pure dephasing time due to elastic collisions), leads to a description of the line width Γ of the LSPP's resonance

$$\Gamma = \frac{2\hbar}{T_2} \quad (2.24)$$

Figure 2.5 shows experimental data, where the line width Γ in the resonant case was measured and compares it to the results of the Mie theory [Sön02]. It shows a good correlation.

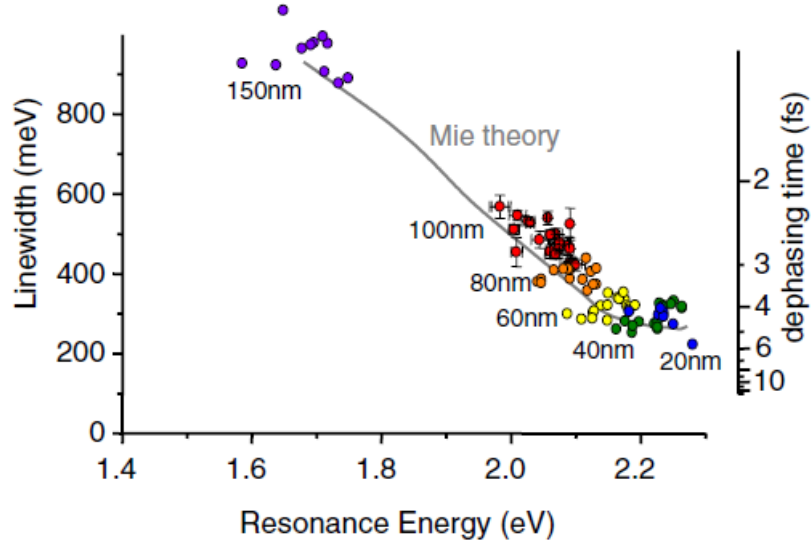


Figure 2.5: Experimentally found line widths of resonances compared to the Mie theory [Sön02.]

For very small nanostructures made of noble metals, the process of chemical interface damping becomes dominant. The coherent oscillation of the electron density scatters elastically at the surface of the structure, as the mean free path of the electrons is significantly bigger than the structure size. This leads to an acceleration of the dephasing. The broadening of the line width can be described as [Höv93]

$$\Gamma_{abs}(a) = \Gamma + \frac{Av_F}{a} \quad (2.25)$$

with Γ_{abs} as the observed line width, Γ the expected line width without chemical damping, v_F the Fermi velocity of electrons and A as the details of the scattering process.

2.1.3 Plasmonic field enhancement

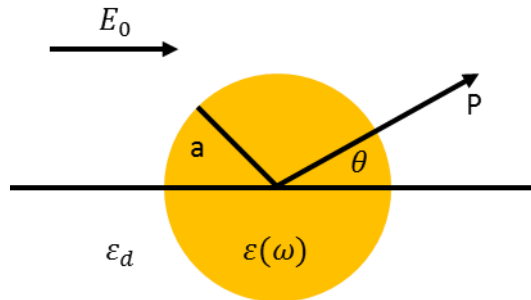


Figure 2.6: Homogenous sphere placed in an electric field.

An important feature of LSPPs is the strong near field enhancement. With a solution for the Laplace equation for the potential $\nabla^2\Phi = 0$, one can calculate the electric field $\vec{E} = -\nabla\Phi$ that is generated by LSPP. If we simplify the problem to a sphere as shown in Figure 2.6, the azimuthal symmetry can be used to find the solution [Jac99]:

$$\Phi(r, \theta) = \sum_{l=0}^{\infty} [A_l r^l + B_l r^{-(l+1)}] P_l(\cos \theta) \quad (2.26)$$

with the Legendre Polynomials $P_l(\cos \theta)$ of the order l , the angle θ between position vector \vec{r} at point P and the z-axis and the sphere radius r . As the potential is finite at the origin, the potentials inside Φ_{in} and outside Φ_{out} of the metal sphere are different [Mai07].

$$\Phi_{in}(r, \theta) = \sum_{l=0}^{\infty} A_l r^l P_l(\cos \theta) \quad (2.27)$$

$$\Phi_{out}(r, \theta) = \sum_{l=0}^{\infty} [B_l r^l + C_l r^{-(l+1)}] P_l(\cos \theta) \quad (2.28)$$

with the boundary conditions for $r \rightarrow \infty$ and at the surface of the sphere $r = a$. The coefficients A_l , B_l and C_l can be determined. $r \rightarrow \infty$ demands that $\Phi_{out} \rightarrow -E_0 z = -E_0 \cos \theta$, which leads to $B_l = -E_0$ and $B_l = 0$ for $l \neq 1$. The other two coefficients have to be determined with the condition at $r = a$. Here the tangential components of the electric fields in- and outside are equal as well as the normal components of the displacement field.

$$-\frac{1}{a} \frac{\partial \Phi_{in}}{\partial \theta} \Big|_{r=a} = -\frac{1}{a} \frac{\partial \Phi_{out}}{\partial \theta} \Big|_{r=a} \quad (2.29)$$

$$-\varepsilon_0 \varepsilon \frac{\partial \Phi_{in}}{\partial \theta} \Big|_{r=a} = -\varepsilon_0 \varepsilon_d \frac{\partial \Phi_{out}}{\partial \theta} \Big|_{r=a} \quad (2.30)$$

This leads to $A_l = C_l = 0$ for $l \neq 1$. With the calculation of the remaining coefficients the potentials are given by [Jac99]

$$\Phi_{in} = -\frac{3\varepsilon_d}{\varepsilon + \varepsilon_d} E_0 \cos \theta \quad (2.31)$$

$$\Phi_{out} = -E_0 r \cos \theta + \frac{\varepsilon - \varepsilon_d}{\varepsilon + 2\varepsilon_d} E_0 a^3 \frac{\cos \theta}{r^2} \quad (2.32)$$

Equation (2.32) describes the superposition of the applied field with that of a dipole, which is located at the center of the sphere. By introducing the dipole moment \vec{p} , the potential outside the sphere Φ_{out} can be rewritten as

$$\Phi_{out} = -E_0 r \cos \theta + \frac{\vec{p} \cdot \vec{r}}{4\pi\varepsilon_0\varepsilon_d r^3} \quad (2.33)$$

$$\vec{p} = 4\pi\varepsilon_0\varepsilon_m a^3 \frac{\varepsilon - \varepsilon_d}{\varepsilon + 2\varepsilon_d} \vec{E}_0 \quad (2.34)$$

The applied field therefore induces a dipole moment inside the sphere and its magnitude is proportional to $|\vec{E}_0|$. It is now possible to introduce the polarizability α

$$\alpha = 4\pi a^3 \frac{\varepsilon - \varepsilon_d}{\varepsilon + 2\varepsilon_d} \quad (2.35)$$

which is defined by $\vec{p} = \varepsilon_0 \varepsilon_d \alpha \vec{E}_0$. Figure 2.7 shows the absolute value α over the frequency ω of the incident field, which is given in energy units eV . The dielectric constant is varying as well with the frequency and is given by equation (2.17). In this special case it is fitted to the dielectric response of silver as described by [Joh72]. Figure 2.7 shows that the polarizability has a maximum, which corresponds to the resonant case and occurs when $|\varepsilon + 2\varepsilon_d|$ is at its minimum. This is the case for

$$Re[\varepsilon(\omega)] = -2\varepsilon_d \quad (2.36)$$

which is also known as the Fröhlich condition and the corresponding mode is called the dipole surface plasmon of the plasmonic nanoparticle. It shows the strong dependency of the resonant frequency on the dielectric medium. With the dielectric function of the Drude model (2.17) this leads to a resonance criterion $\omega_0 = \omega_p/\sqrt{3}$ for metals.

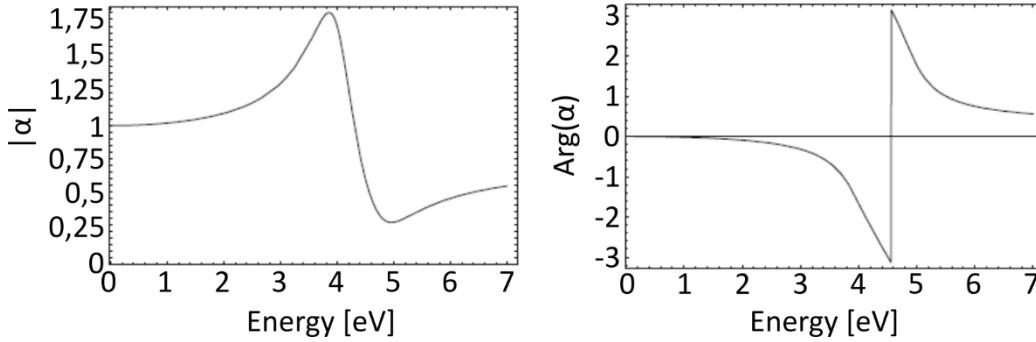


Figure 2.7: Absolute value and phase of the polarizability α of a metal nanoparticle with $d \ll \lambda$ dependent on the frequency of the incident field (here expressed in energy units). [Mai07]. $\varepsilon(\omega)$ is given here by a Drude fit to the dielectric function of silver [Joh72].

With the potentials (2.31) and (2.32) the electric field distributions can be calculated to

$$\vec{E}_{in} = \frac{3\varepsilon_m}{\varepsilon + 2\varepsilon_m} \vec{E}_0 \quad (2.37)$$

$$\vec{E}_{out} = \vec{E}_0 + \frac{3\hat{n}(\hat{n} \cdot \vec{p}) - \vec{p}}{4\pi\varepsilon_0\varepsilon_m} \frac{1}{r^3} \quad (2.38)$$

with the unit vector \hat{n} in direction of the point of interest P. In the resonant case for the polarizability, both electric fields experience a resonant enhancement. This field enhancement is the basis of many plasmonic applications and in the following, it is going to be of great importance, as well. Two examples are shown in Figure 2.8. It shows two

CST microwave studio simulations of the electric field enhancement, one of one gold dipole nanoantenna (a) and one of two gold nanoantennas with a gap of 50 nm (b) on a glass substrate. All antennas are 230 nm long, 50 nm wide and 30 nm high. The exciting light is polarized in direction of the long antenna's axis (x-axis). The single antenna already shows a quiet strong field enhancement on the ends of the dipole. However, in a small gap between two antennas this enhancement is increased even more, as the fields of both antennas overlap.

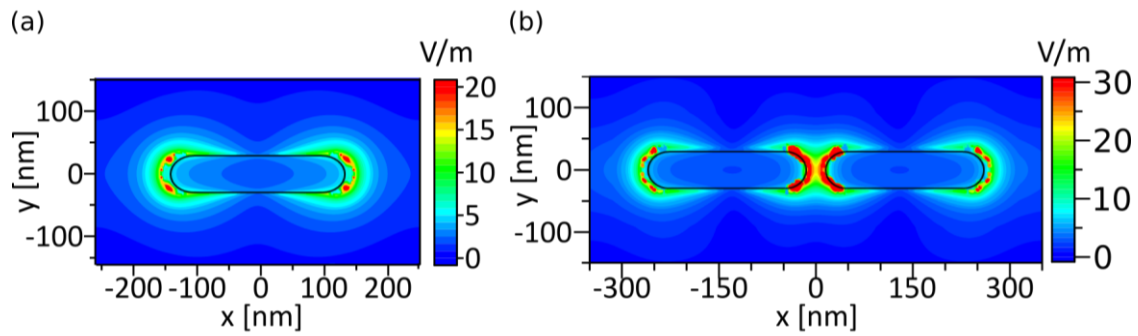


Figure 2.8: CST simulation of the electric field enhancement (a) of a gold nanoantennas with a length $l = 230$ nm, a width $w = 60$ nm and a height of $h = 30$ nm on a glass substrate (b) of two nano antennas with the same size parameters as in (a) that are separated by a gap of 50 nm

2.2 NONLINEAR PLASMONICS

Another important part of this work next to plasmonics is nonlinear optics. Both combined leads us to nonlinear plasmonics, which plays an important role in this work, as the majority of the investigated metasurfaces are based on nonlinear plasmonic effects, e.g. the enhancement of nonlinear signals by plasmonic nanoantennas or the generation of nonlinear signals by plasmonic metasurfaces.

2.2.1 Nonlinear optical effects

In 1961 Franken et al. discovered the second-harmonic generation, which is often seen as the beginning of the field of nonlinear optics [Fra61]. This field studies the optical phenomena, which occur when materials respond nonlinearly to an electrical field, which is applied during the interaction of said material with light. The material polarization P can describe this response of the material to the optical field.

$$P = \varepsilon_0 [\chi^{(1)}E + \chi^{(2)}E^2 + \chi^{(3)}E^3 + \dots] \quad (2.39)$$

Here ε_0 is the permittivity in vacuum and $\chi^{(n)}$ is the n 'th order susceptibility of the material [Boy08].

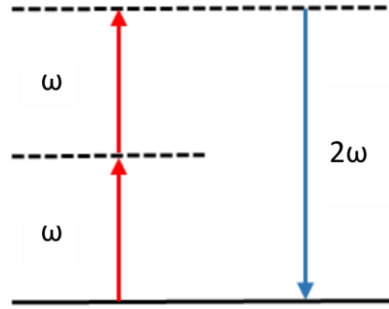


Figure 2.9: Photon diagram for SHG. Destruction of two photons with frequency ω and simultaneous generation of a photon with the doubled frequency 2ω .

As for moderate light intensities only the first term in equation (2.39) is important, which leads to conventional optical effects, one needs laser light that generates strong fields to generate any higher harmonic. Then the higher order terms ($n > 1$) need to be considered as well. These terms can contain sums and differences of the incident frequencies, which leads to radiation at new frequencies. Photon diagrams as seen in Figure 2.9 and Figure 2.10 help to visualize this different frequency combinations. Figure 2.9 explicitly shows a diagram for second harmonic generation (SHG). This is one of the second order processes ($n = 2$), such as sum- and difference frequency generation. For higher orders, there exist even more possibilities e.g. third harmonic generation or four wave mixing. According to Figure 2.9 the SHG process consists of the destruction of two photons with the frequency ω , and the simultaneous generation of a photon with the doubled frequency 2ω . The dashed lines in this image represent so called virtual states, which do not describe energy eigenlevels of a free atom. They represent the combination of the energy of one of the

energy eigenstates of the atom and of one or more photons of the incident field. The solid line however, corresponds to the atomic ground state.

Assuming a plane incident wave with the electric field given by

$$\vec{E}(t) = \vec{E}e^{-i\omega t} + \text{c.c.} \quad (2.40)$$

passes a nonlinear material with the second-order susceptibility $\chi^{(2)}$, and using equation (2.39) leads to the nonlinear polarizability [Boy08]

$$\vec{P}^{(2)}(t) = 2\varepsilon_0\chi^{(2)}\vec{E}\vec{E}^* + (\varepsilon_0\chi^{(2)}\vec{E}^2e^{-i2\omega t} + \text{c.c.}) \quad (2.41)$$

This shows that the second order polarizability consists of a term at the incident frequency and a term at the doubled frequency. This second term can lead to radiation with the SHG frequency.

Equation (2.39) is a simplified model, in which the electric field and the polarization are treated as scalar quantities. A complete description needs to take account of their vectorial character. Therefore, the susceptibilities are of tensorial nature and depend on the material symmetry. Considering the dipolar approximation, second harmonic processes are only allowed in non-centrosymmetric materials, whereas third-order processes can occur in all materials. Nevertheless, due to surface roughness, which can break the symmetry, even some centrosymmetric structures can generate SHG as well. A more detailed discussion will follow in chapter 2.5.

2.2.2 Optical parametric oscillator

One broadly used application of nonlinear optics is an optical parametric oscillator, which is also used in all following experiments. It uses a suitable nonlinear medium, which is pumped by a pump laser. With this technique two new frequencies, a signal ω_s and an idler frequency ω_i , are generated. Since momentum and energy have to be conserved, one obtains [Mol87]

$$\omega_p = \omega_s + \omega_i \quad (2.42)$$

and

$$k_p = k_s + k_i \quad (2.43)$$

which equals

$$n_p\omega_p = n_s\omega_s + n_i\omega_i \quad (2.44)$$

This means the difference frequency generation of the pump and the idler result in the signal, which is the desired output frequency (see Figure 2.10 for the corresponding

photon diagram). Compared to other difference frequency generations, the idler of the process in the OPO is a byproduct, while only the pump is supplied externally.

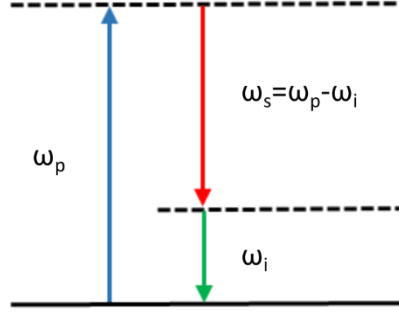


Figure 2.10: Photon diagram for difference frequency generation.

Combining equations (2.42) and (2.44) leads to

$$\omega_s = \omega_p \frac{n_p - n_i}{n_s - n_i} \quad (2.45)$$

Only with anisotropic crystals, this equation can be fulfilled. In those crystals equation (2.45) has two solution for any given $n(\omega)$. Therefore the laser light can be tuned by varying $n(\omega)$. This means either adjusting the incident angle of the light onto the crystal or the crystals temperature are suitable options to tune the output light.

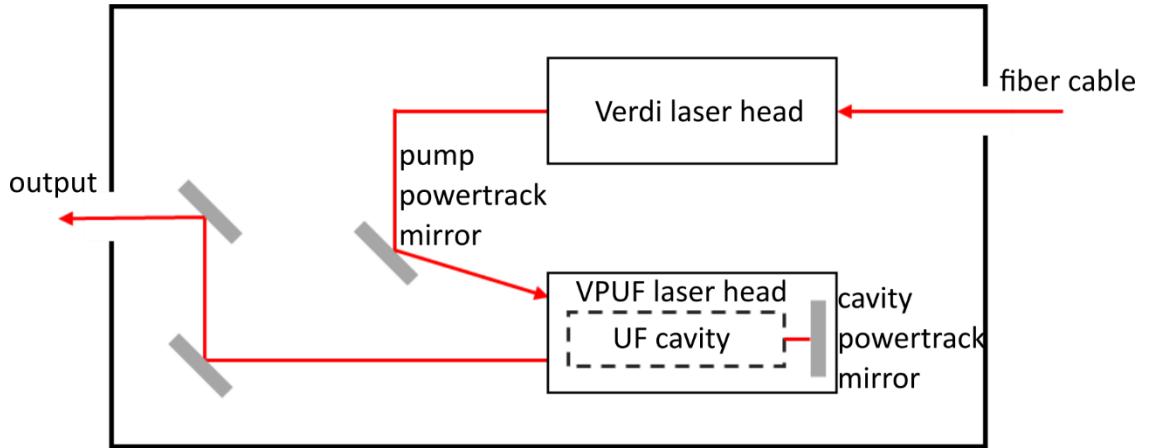


Figure 2.11: Schematic of pump laser head used in the experiments of this work (Chameleon Ultra II).

To gain a broader wavelength spectrum of the signal wavelength, it is also suitable if the pump laser is tunable as well. Figure 2.11 shows a schematic of the Coherent Chameleon Ultra II, which serves as the pump laser head in the following experiments. It consists of a Verdi solid state pump laser and the Ultra-Fast (VPUF) laser head. The Verdi laser head uses Neodymium Vanadate (Nd:YVO_4) as gain medium and Lithium Triborate (LiB_3O_5) as nonlinear wavelength doubling medium. The pump powertrack mirror guides the beam

to the VPUF laser head. This is a piezo-driven mirror and together with the cavity powertrack mirror it enables a perfect alignment into the VPUF cavity as well as an optimum alignment of the cavity itself. In operation, the laser head only uses one of these powertrack mirrors, never both at the same time. The ultra-fast VPUF cavity contains a Titanium: sapphire (Ti:Sa) crystal as gain medium. Not shown in the schematic is a build in spectrometer that reads out the laser wavelength directly. The Chameleon Ultra II has a pulse length of around 200 *fs* and a repetition rate of 80 *MHZ*. The wavelength can be tuned from 680 to 1080 *nm*.

This output laser beam is used as the pump laser for the Coherent Chameleon Compact OPO, which can tune the signal wavelength from 1000 to 1600 *nm*. There is also the possibility to use the output ports of the pump and the idler beam. The idler wavelength reaches from 1700 to 4000 *nm*.

2.2.3 Basic nonlinear plasmonic concepts

Now the concepts of plasmonics and nonlinear optics shall be combined. There are two ways, in which plasmonic structures can enhance nonlinear optical effects. As explained in chapter 2.1.3 the plasmonic structures generate a large near field enhancement at the metal-dielectric interface. Equation (2.39) shows that second order nonlinear processes dependent quadratically on the electric field. This means that the field of the plasmonic structures, which can locally enhance the nonlinear response, has a big effect. It is even possible to integrate this response over the whole sample, if the structures are designed carefully. With the same method, it is possible to increase the nonlinear response of the metal itself.

Furthermore, the plasmon resonance and the SPP wave vector, respectively, are highly sensitive to the refractive index of the surrounding material [Kau12]. That is why the resonance can be easily modified by a nonlinear change of the refractive index.

As we are dealing with metal structures, ohmic losses cannot be prevented. As in this work, only experiments with LSPP are shown, we will focus on their description. Here, these intrinsic losses lead to limited achievable field factors.

2.2.3.1 Enhanced nonlinear effects with structured plasmonic surfaces

Investigations of the effect of plasmonic structures on nonlinear effects started with a silver nano grating, which was designed to enhance the local field at the SHG wavelength. Here the SHG is emitted into the first diffraction order [Wok81]. L-shaped nanoantennas arranged in an array were the first non-centrosymmetric nanoparticles, which were investigated [Lam97]. This experiment used SHG autocorrelation measurements to determine the femtosecond plasmon dephasing time. Arrays of L-shaped nano antennas have also been used to study their SHG properties, especially their efficiency, which depends strongly on the order of the particles in the array, the study found out [Tuo02].

As expected, the enhancement was strongest, when the structures were excited with a fundamental wave at the resonance frequency.

Another example for symmetry breaking structures are split-ring resonators (SRR) [Lin12]. Here it was shown that in a square array the conversion efficiency of SHG is dependent on the lattice constant. Other studies suggest the interpretation of the SRR plasmonic resonance as having electric and magnetic character, even though the material itself is not magnetic [Sou11]. The assumption, that these magnetic resonances are favorable for SHG, are confirmed by measurements of Klein et al. [Kle06]. However, the inversed SRR structures, which are holes in a metal film, provide no significantly different results compared to the other SRRs [Fet08]. As in these structures the roles of the electric and magnetic resonances are reversed, the importance of the magnetic character of the resonance to SHG could not be confirmed.

Some works also investigate centrosymmetric structures for SHG, such as nanoparticles [McM06] and nano-apertures [Xu07]. The measured SHG is always strongest when either the fundamental or the SHG beam have an oblique incident angle.

As described in chapter 2.1.3, nanostructures can lead to strong local field enhancements [Ker12]. Furthermore, field confinements below the optical diffraction limit are possible [Ker12]. In many works, these properties are utilized to enhance the matter-light interaction, which in many cases is otherwise quite weak. This enhancement can be used for imaging beyond the diffraction limit [Bar03], plasmonic detectors and emitters or for frequency conversion with low excitation powers [Har12]. This work as well, will investigate this interaction.

2.3 DOUBLE RESONANT PLASMONIC NANOANTENNAS

As described before a lot of works achieved a strongly enhanced local electric field and therefore also increased the SHG efficiency [Ko11, Wal13]. However the problem remains, that the reemission of the SHG of the nonlinear material into the far field stays rather weak. One possible solution for this problem is an additional resonance of the nanostructures at the SHG frequency. This resonance enables a better radiation into the far field. Therefore, double resonant plasmonic antennas have been of great research interest in the last years [Cel15, Lee14, Lin16, Thy12].

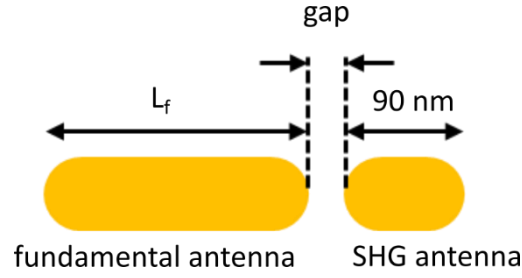


Figure 2.12: Design of double resonant antenna consisting of a long fundamental and a short SHG antenna with a small gap in between. Both are made of gold.

2.3.1 Experiment

In the work together with Nils Weber and Max Protte double resonant plasmonic antennas are put on top of two different zinc oxide substrates [Web17]. The antennas are fabricated via electron beam lithography (EBL) and a lift-off technique, which is explained in chapter 2.5.1. As in this case the substrate is not conductible, an extra layer of chromium has to be evaporated onto the resist before exposure with the electron beam. The antenna design of a dipole pair only separated by a gap of a few nanometers is based on the design used by Thyagarajan et al. [Thy12]. Figure 2.12 shows the design used in this this work. The double resonant antenna consists of two gold nanorods with a width of 50 nm and a height of 30 nm . The length of the SHG antenna is fixed to 90 nm , whereas the length of the fundamental antenna L_f varies from 160 to 320 nm in steps of 10 nm . These antennas are fabricated on a bulk ZnO substrate as well as on a 230 nm thin ZnO layer on a silicone substrate, which was grown via molecular beam epitaxy (MBE). The actual design is shown in Figure 2.13.

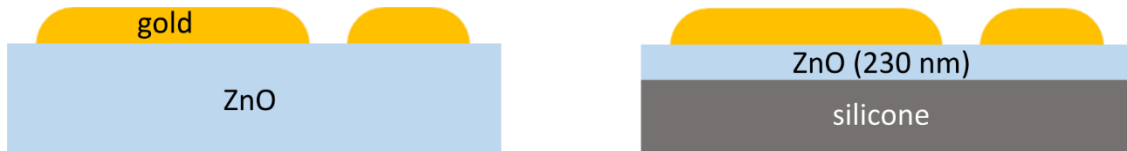


Figure 2.13: Schematic of the two different sample designs. On the left the gold antennas are put on a bulk ZnO substrate and on the right on a 230 nm thin ZnO layer on top of a silicone substrate

The fundamental antenna corresponds to the longer rod and is given this name, as the resonance is excited by the fundamental (or incident) wavelength. The shorter rod (the SHG antenna) is supposed to have a resonance at the SHG frequency, where the ZnO substrate generates light. ZnO is known for its large second order nonlinear coefficient $\chi^{(2)}$ and the described nanostructures are aimed to enhance the SHG itself as well as the reemission at normal incident into the far field. Such amplified nonlinear conversion efficiencies could improve many nonlinear optical applications that are based on ZnO or other nonlinear materials.

There are two mechanisms, which serve to enhance the conversion efficiency. First, the strong near field enhancement at the tips of the nanorods, especially in between the small gap where the fields of both antennas overlap as shown in Figure 2.8 (a) and (b). Those field hotspots enhance the nonlinear polarization of the material, as this is quadratically proportional to the electric field (see equation (2.39)) and therefore amplify the SHG signal itself. Second, the SHG antennas serves to gather SHG light, that is generated locally by the ZnO substrate and reemit it into the far field of the dipole.

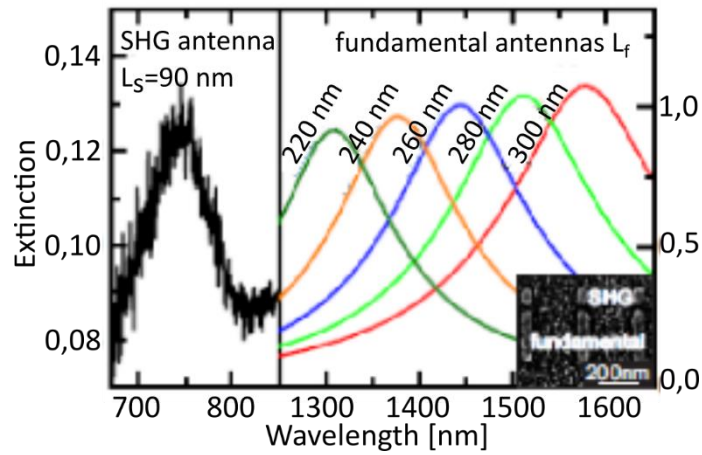


Figure 2.14: Experimental data of the measured and normalized extinction spectra over the wavelength and in dependence of the length of the fundamental antenna on bulk ZnO. For each array there appear two resonance, one for the fundamental antenna (which changes as the length changes) and one for the SHG antenna (which does not change) [Web17]

In the beginning, it is important to find the perfect length L_f of the fundamental antenna that leads to the doubled resonance frequency of the short SHG antenna. Therefore, the linear optical characteristics of the antennas are investigated by using a Fourier transform infrared spectrometer (FTIR) with a tungsten light source (see chapter 2.5.2). The transmission spectrum is measured for each antenna array with a linearly polarized incident beam, that was oriented parallel to the long axis of the antennas (see chapter 2.5.2 for detailed description). By measuring a transmission spectrum of the substrate itself, the results of the antennas are normalized. Figure 2.14 shows the measured extinction spectra of the fabricated nano antennas on the bulk ZnO substrate. The resonance of the SHG antenna stays always the same at 750 nm, as the antenna size does

not change. However, for the fundamental antenna, the resonance wavelength increases with increasing length. This occurs almost linearly with the antenna length and results in resonances from around 1200 nm to 1700 nm . For the sample with the thin ZnO layer the resonances experience a slight blue shift. That is caused by the refractive index of the ZnO. Whereas it is 1,94 for the bulk ZnO, it was determined to 1,8 via ellipsometry for the MBE-grown ZnO. Here the SHG antenna's resonance lies at 700 nm , which leads to a corresponding resonance of the fundamental antenna at 1400 nm . This is given for an antenna length of 240 nm .

As the fundamental resonance is supposed to be the doubled SHG frequency, the nonlinear measurements are performed on the array where this condition is fulfilled. This means for the bulk ZnO sample a fundamental wavelength of $1,5\text{ }\mu\text{m}$ is needed, which is given for an antenna length $L_f = 280\text{ nm}$. Figure 2.15 shows a schematic of the nonlinear measurement setup. For the incident laser beam an OPO is used (see chapter 2.2.2). The fundamental wavelength is varied from 1300 to 1600 nm in steps of 10 nm . With a fused silica lens with a focal length of 100 mm the laser beam is focused onto the antenna array from the backside of the thin film ZnO sample, as Silicone is transparent in the infrared but not in the visible range. For better comparison, this is also done with the bulk sample. A $20\times$ objective with a NA of 0,45 collects the transmitted SHG light. The light is then coupled into a spectrometer, which measures the intensity of the SHG signal. One expects this signal to increase when the resonance of the short antenna matches the SHG frequency of the resonance of the fundamental antenna.

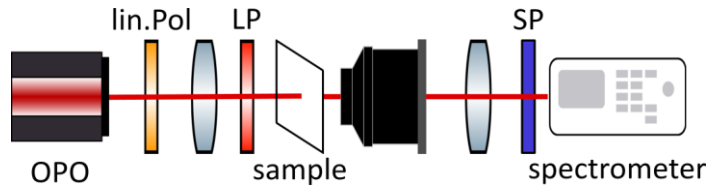


Figure 2.15: Experimental setup for the nonlinear measurements. The beam of the OPP passes a linear polarizer and is focused onto the antenna fields of the sample. A long pass filter in front of the sample filters out all the possible harmonic generation light, which is generated by other optical components beside the sample. Then a $20\times$ objective collects the light, that is coupled into a spectrometer in the end.

Both substrates generate SHG signals of their own. The signal of the bulk ZnO sample is naturally much bigger. Nevertheless, the signals of the antenna arrays are normalized to the corresponding substrate. Figure 2.16 (a) shows the data of the 280 nm long fundamental antenna on the bulk substrate. Surprisingly, the intensity shows a minimum at the wavelength, where a maximum was expected. This means, that the SHG of the antenna array is weaker than the signal of the bulk ZnO itself. Therefore, the antennas suppress the nonlinear signal of the substrate rather than enhance it as supposed. The reason behind this behavior is the strong resonant absorption and scattering of the gold antennas. These mechanisms reduce the SHG that is generated by the ZnO bulk material.

As this seems to be a problem of the bulk material, where the SHG intensity is quite high, and the antennas only contribute on the substrate's surface the measurement is repeated with the thin film ZnO sample. As the preferential orientation of the grown film is along the [001] direction, due to symmetry restrictions there should not be a nonlinear signal from the ZnO under normal incident. Therefore, the antenna array, if resonantly excited enhances the SHG signal from the sample, as the light is scattered into the directions, where the nonlinear susceptibility components are addressed. In Figure 2.16 (b) the enhancement can be observed for fundamental antennas with a length of 240 nm. In fact, it can be seen in all the measured arrays, even when the resonances of both antennas do not fit perfectly.

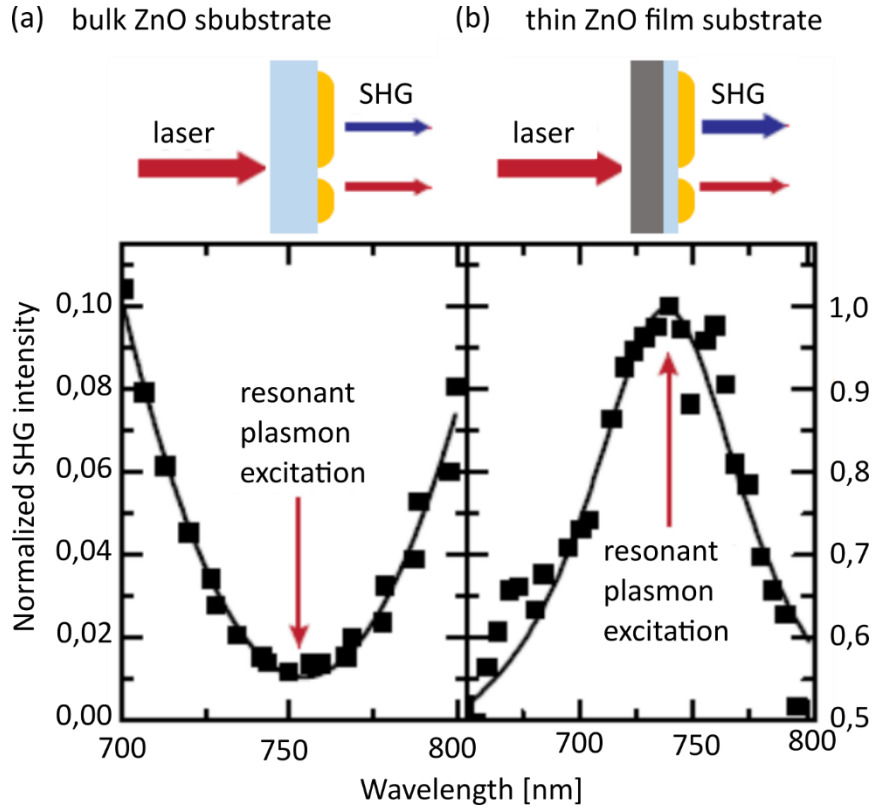


Figure 2.16: (a) Experimental data of the nonlinear measurements of antennas on a ZnO bulk substrate, where the SHG is suppressed by the nanoantennas (b) on a thin film ZnO substrate, where the antennas enhance the SHG signal. [Web17]

For a better evaluation, to see if this enhancement originates in the double resonant antennas, a comparison with single resonant antennas is necessary. Consequently, some arrays with only fundamental antennas are fabricated on the same thin film ZnO substrate. The resonance of the single antennas and the fundamental antenna is around 1400 nm and that of the SHG antenna is 700 nm. Then the same nonlinear measurement is performed and the comparison of single antennas and double resonant antennas can be seen in Figure 2.17. Here the SHG intensity is plotted for different excitation wavelength and then fitted with a Lorentz-curve. This shows the importance of the small SHG antenna. The SHG signal of the double resonant antennas is a least twice as high as that of the single antennas. This means that the purpose of the small SHG antenna, which

is better at decoupling of the generated nonlinear light into the far field, is fulfilled. As the single antennas only help in enhancing the nonlinear generation with its strong near field, they lack in actually coupling this light into the far field as well. That explains the higher SHG intensity of the double resonant antennas that is increased by roughly a factor of two.

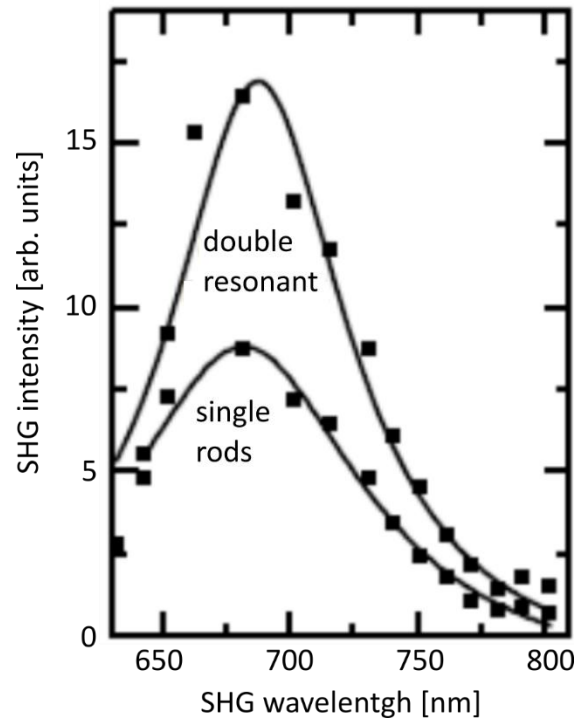


Figure 2.17: Comparison of SHG intensities from single dipole nanorods to double resonant nanoantennas (black squares). The double resonant antennas increase the intensity by a factor of two due to the second resonance of the short antenna at around 700 nm. The corresponding Lorentz fit is depicted by the two solid lines [Web17].

2.3.2 Short conclusion

It is shown that the fabricated double resonant gold nanoantennas do in fact enhance the SHG signal of a thin film ZnO substrate even more than single dipole nanoantennas. The double resonant nanoantennas consist of a long and short dipole antenna that are resonant at the excitation wavelength and the corresponding SHG wavelength, respectively. They are separated by only a small gap. To fulfill the criterion of two separate resonances at ω and 2ω the length of the long antennas was varied while the short antenna's length stayed constant.

On a bulk ZnO substrate an additional antenna field suppresses the SHG intensity compared to the bare substrate. This is caused by the resonant absorption and scattering of the antennas which leads to less generated SHG in the bulk ZnO. However, in a thin ZnO film on a silicon substrates the antennas enhance the SHG strongly. The bulk contribution of the thin film is negligible, whereas the strong near field of the antennas caused by LSPs dominates the SHG process.

By using double resonant antennas as described before, the SHG intensity can be increased by a factor of two compared to single dipole antennas that are resonant at the incident wavelength.

2.4 NANOANTENNAS ON PIN-DIODES

As mentioned before plasmonic nanoantennas cannot only help enhancing a signal at the incident wavelength, but can generate a harmonic signal as well. They can even generate harmonic signals themselves depending on their rotational symmetry (see chapter 2.5). Those antennas are put on PIN (positive intrinsic negative) diodes with a band gap in the visible range. PIN diodes are widely used as radiation detectors and the commercially available ones often work in the x-ray regime [Ram08]. Compared to other detectors such as ion chambers, they offer different advantages such as a smaller size and a better signal-noise ratio [Jac83]. Combining now PIN diodes that work in the visible regime with metasurfaces can turn the diodes into infrared detectors.

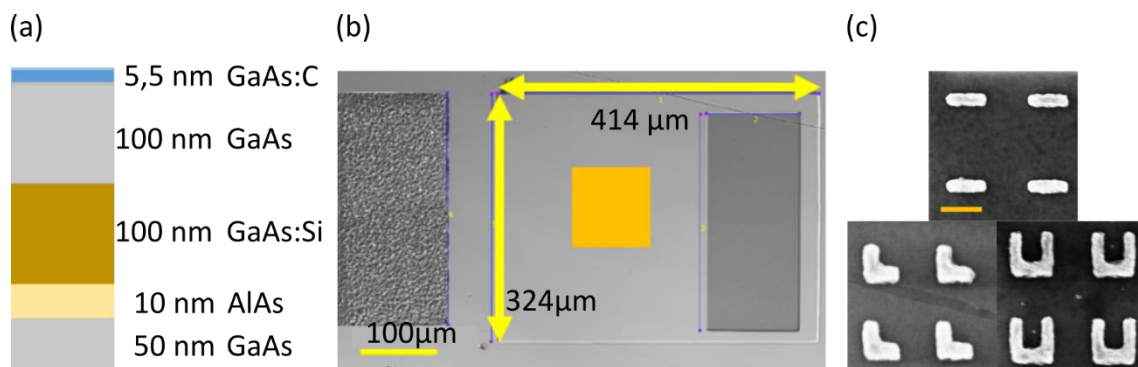


Figure 2.18: Design of the Pin diode and the nanoantennas (a) Cross section of the layers of the diode, the Si doped GaAs is the negative part of the diode and the C doped the positive one. (b) SEM image of the surface of the diode. The diode itself is $414\mu\text{m}$ long and $324\mu\text{m}$ wide. On the right a gold patch is visible which contacts the p-doped layer. On the left the sample is etched to the n-layer what enables contacting of the n-doped layer. The orange square in the middle of the diode depicts the nano antenna field, which is fabricated on top. (c) Exemplary SEM images of used gold nano antenna arrays (dipoles, L-shaped and split rings) (scale bar: 150 nm)

2.4.1 Working principle of PIN diodes with plasmonic nano antennas

The working principle of a PIN diode is similar to that of a p-n diode. A PIN diode consists of a p-type and a n-type semiconductor, which are separated by an intrinsic one. Figure 3.5 (a) shows the cross section of the PIN diode that is used in the following. The semiconductor is gallium arsenide (GaAs) (intrinsic), which is doped with either silicon (Si) (n-type) or carbon (C) (p-type). Both the n- and the p-type regions are highly doped, as they are used for ohmic contacts. The sandwiched intrinsic layer can increase the breakdown voltage for the application of high voltages significantly. That makes the diode suitable as attenuator, fast switch and photo detector.

If voltage is applied to a normal p-n diode in reverse direction, a charge carrier depletion area is generated. The thickness of this area is dependent on the applied voltage and the mobility of the charge carriers in the semiconductor material. If a photon passes this area, the generated electron-hole pairs separate and cause an electric impulse. If no voltage is

applied an illumination of the diode causes a photo voltage, which is used in solar cells. An additional intrinsic layer between p- and n-region enlarges the depletion area. This increases the volume where a photon can generate electron-hole pairs and therefore leads to a better performance compared to a p-n diode.

In the case described in the following the diode is operated unbiased and the current generated by an incident laser beam is measured. The diodes energy gap lies at $1,3\text{ eV}$ ($\approx 950\text{ nm}$).

2.4.2 Experiment

First, the antenna arrays are fabricated on different PIN diodes (on top of the p-type GaAs:C layer) that are all on one sample. Figure 2.18 (b) shows the design of one PIN diode with an antenna array on top. The area of the diode is $414\text{ }\mu\text{m}$ long and $324\text{ }\mu\text{m}$ wide, which is covered by an antenna array of $100\times 100\text{ }\mu\text{m}^2$ (yellow field). On the right, a gold patch is placed to contact the p-type GaAs:C and on the left the sample is etched to the n-doped GaAs:Si layer to enable a contact as well. The complete sample consists of ten PIN diodes, of which some are covered by an antenna array. These arrays are fabricated as described in chapter 2.5.1. Figure 2.18 (c) shows SEM images of the three different antenna designs that are used (dipoles, L-shaped antennas and split-rings). All three are fabricated with different arm length. The arm width is fixed to 50 and the height to 30 nm . The contacts are then bonded and the sample is put into a metallic box (Figure 2.19), to avoid possible currents generated by the surrounding light. The bonding wires lead to the contacts outside of the sample box, which makes it possible to measure the currents.

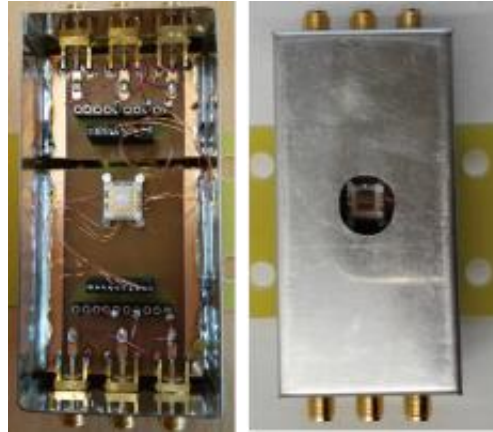


Figure 2.19: *Measurement box opened and closed.* The sample is placed in the middle of the box and the contacts on the sample are bonded to the contacts seen on the outside of the box. A whole in the lid enables the laser beam to illuminate the sample.

For all diodes a power dependent measurement is performed. Figure 2.20 shows the measurement setup. The laser beam of the OPO first passes a half wave plate and then a linear polarizer. With these two components, it is possible to control the power of the

incident beam by simply rotating the half wave plate. With the linear polarizer the needed polarization can be set. The laser light is then focused onto the sample with a fused silica lens with a focal length of $f = 75 \text{ mm}$. A long pass filter (LP) with a cut-off wavelength of 1000 nm assures that no light with a shorter wavelength reaches the sample. This is of great importance as the energy band gap of the PIN diode lies at 950 nm and no light at that wavelength is supposed to generate any current, as only the generated current by SHG is of interest. The whole sample box is turned by a small angle, which makes it possible to install an imaging system consisting of a lens with a focus length of 25 mm and a CCD camera perpendicular to the sample. This imaging system allows the user to align the laser spot directly on the antenna array that is located on top of each PIN diode. For this alignment, the box is placed on a three dimensional translation stage. By short outing the contact of the n-doted GaAs it is possible to measure the current at the contact of the p-dotted semiconductor. A hinged mirror in front of the sample box enables a power measurement.

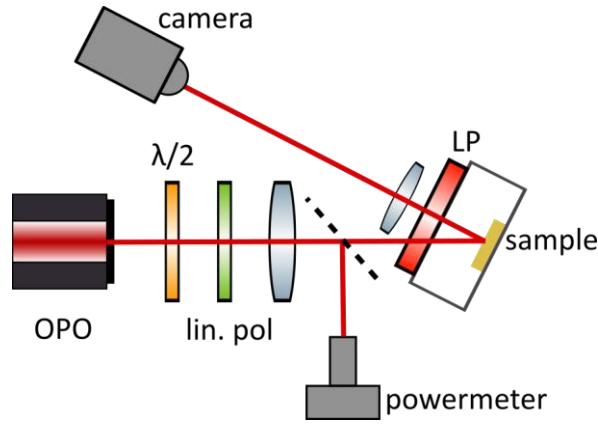


Figure 2.20: Measurement setup. With a half-wave plate and a linear polarizer, it is possible to control the power of the passing laser beam. A lens focuses the light onto the sample surface. A long pass filter ensures that only light with a wavelength above 1000 nm passes to the sample. An imaging system consisting of another lens and a CCD camera enables the user to align the laser on the antenna arrays. With a foldable mirror (dotted line), it is possible to measure the beam power.

Before using the above described setup the reflection spectra of the antenna arrays on top of the PIN diodes are measured with the FTIR as described later in chapter 2.5.2. The spectra of the antenna arrays are normalized by dividing them with the spectrum of only the PIN diode. The resulting reflection is given by

$$R = \frac{I}{I_0} \quad (2.46)$$

with the measured intensity of the structured fields I and the reference intensity I_0 of the PIN diode. The spectra are measured with linear polarized light. The direction of x - and y -polarization can be seen in Figure 2.21 (a) –(c) next to the SEM images of the antennas. Figure 2.21 also shows the measured spectra for dipole (a), L-shaped (b) and split-ring (a)

antennas. The dipole antennas shown in Figure 2.21 (a) are 115 nm long, 50 nm wide and 30 nm high. The resonance wavelength in x -direction (long antenna axis) is 1100 nm . As the resonance in the direction of the short axis is supposed to be much shorter, it cannot be seen in this spectrum and is of no importance. The L-shaped antennas shown in Figure 2.21 (b) have two arms with the same length of 130 nm . The width and height are fixed to the same values as for the dipole antennas. As the arms have the same length, the spectra for both polarization directions along the arms are nearly identical. This means that also the resonance wavelengths are identical at 1500 nm .

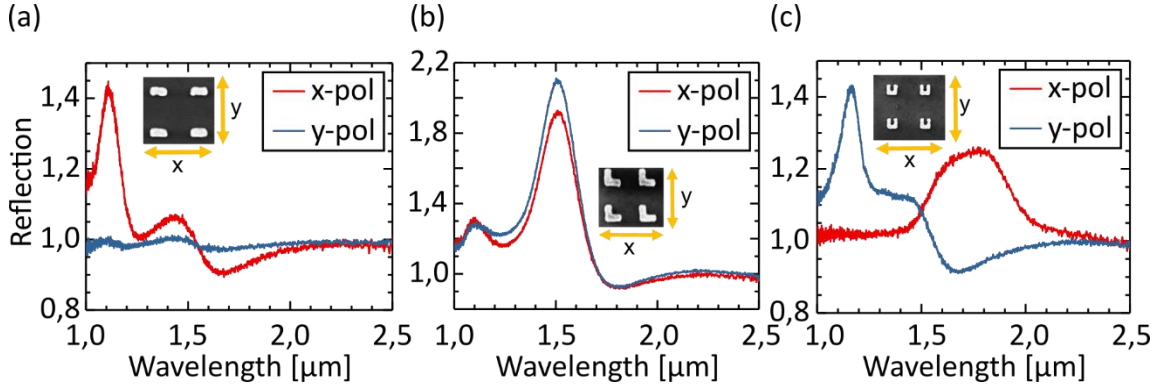


Figure 2.21: FTIR spectra of different antenna arrays on PIN diodes. (a) Spectrum of dipole antennas with light polarized along the long (x -direction) and short (y -direction) axis (b) spectrum of L-shaped antennas in both polarization directions along the arms (c) spectrum of split-ring antennas with linear polarized light in two directions.

In plasmonic split-ring resonators, higher modes can be excited depending on the polarization of the incident light. If the laser beam is polarized perpendicular to the gap (x -direction) the internal fields in both legs are in phase whereas for a polarization along the legs (y -direction) the internal fields of the legs have opposite flow directions which causes a phase difference of π [Roc06]. This is why the resonance for an incident polarization in y -direction appears at a higher energy than for a polarization in x -direction, which is equivalent to a shorter wavelength.

Figure 2.21 (c) shows exactly this behavior, for the resonators that are depicted there as well, which have arm lengths of 125 nm and a base length of 120 nm . Width and height are the same as for the antennas described above. For an incident polarization in y -direction the split-rings are resonant at 1150 nm and in x -direction at 1750 nm .

In the following, the nonlinear photo detector measurements are being discussed on the example of the L-shaped antennas. With the above described measurement setup, the laser beam is focused onto the sample and the power is varied in 1 mW steps. The wavelength of the incident beam is set to 1200 and 1500 nm (Figure 2.22). The polarization of the beam can be set via the linear polarizer and measurements are performed under both polarizations parallel to the arms of the L-antennas. The laser beam is focused on the antenna array on top of the PIN diode. To be able to see the effect of

those antennas a reference measurement is performed on the pure PIN diode next to the antennas.

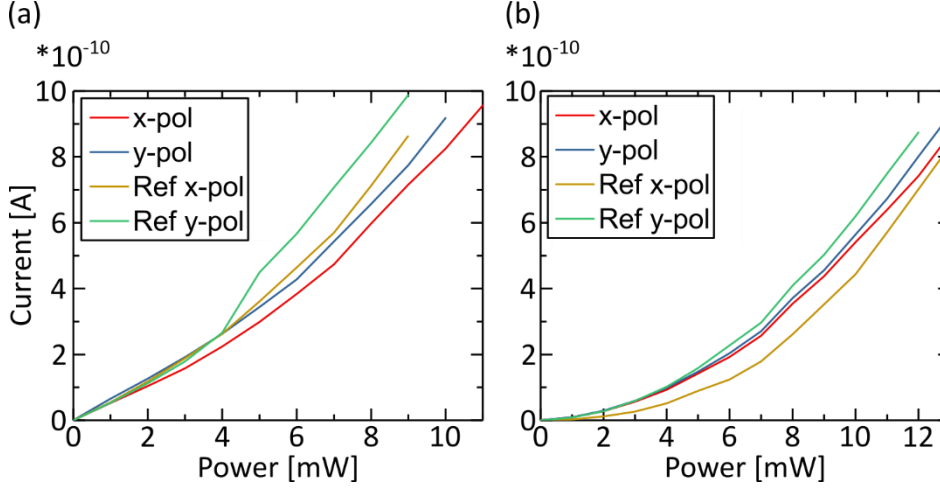


Figure 2.22: Power dependent measurement of L-shaped antennas. (a) at an incident wavelength of 1200 nm (b) at 1500 nm.

Figure 2.22 shows these measurements for the two different exciting wavelengths 1200 nm (a) and 1500 nm (b). It is obvious that in both cases the behavior of the generated current is nonlinear to the applied power of the laser beam. However, there does not seem to be a clear difference between the measurements on the antenna array and the pure PIN diode. As the ampere meter saturates at $10 \cdot 10^{-10}$ A the data is plotted until the possible power setting. For the 1200 nm measurement, both the current for x - and y -polarized incident light is slightly higher on the pure PIN diode compared to the antenna array. For x -polarized light at 1500 nm the antenna array generates more current than the pure diode. However, y -polarization produces an opposite result. As the PIN diode does not have a predominant direction, every linear polarization should generate the same current, which is not the case. For both imaged wavelengths, the current for y -polarized light is higher than for x -polarization. Concerning the antenna array, the generated current should be the same for both polarizations, as the arms of the L-shaped structures have the same length, and therefore the electric field enhancement is the same. The measurements, however, show a different behavior. If the incident light is polarized in y -direction the generated current is higher. This can be explained, with the already higher current for this polarization by illuminating just the PIN diode without antennas.

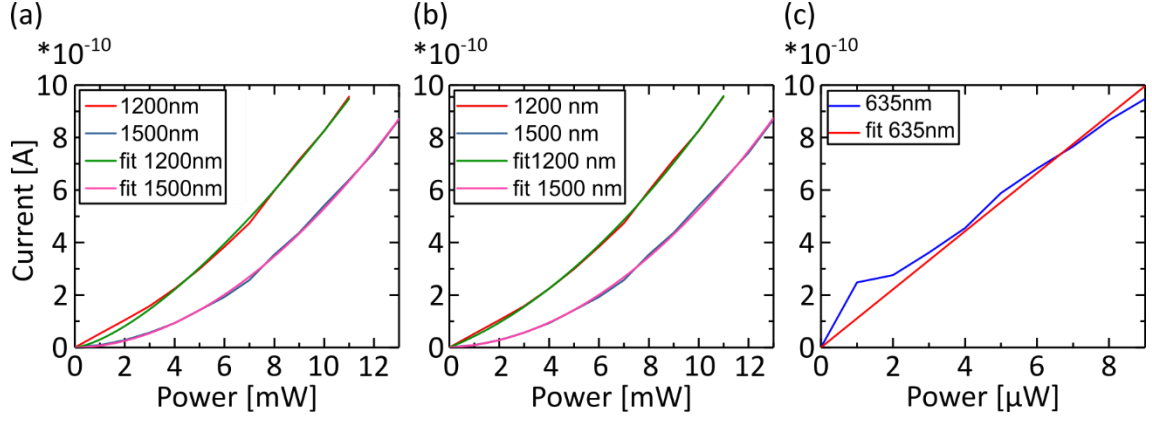


Figure 2.23: Fitted power dependent current measurements. (a) Current measurements of the L-shaped antennas on a PIN diode with linear polarized light in x-direction with fundamental wavelengths 1200 and 1500 nm fitted with $y = a \cdot x^b$ (b) The same measurements fitted with $y = ax + bx^2$ (c) Measurement with linear polarized visible light at 635 nm fitted linearly, which is performed at power intensities three orders of magnitudes lower than the measurements of (a) and (b)

Admittedly, the current in all four measurements of both wavelength behaves nearly equally. It can be seen that there is no linear dependency to the applied power. At the example for x -polarized incident light on an antenna array. Figure 2.23 (a) shows fitted curves to the measured data. For the fits the function

$$y = a \cdot x^b \quad (2.47)$$

is used, to see if the dependency might be quadratic as this is the expected behavior for SHG processes. Regarding the wavelength of 1200 nm the fit formula is

$$y = 2,99 \cdot 10^{-11} \cdot x^{1,44} \quad (2.48)$$

This is obviously not quadratic, but not linear as well. As the wavelength is still quite close to the band gap of the PIN diode the process is probably a mixture of a linear and a SHG process, where the linear one seems a bit more dominant. The fit function for the 1500 nm measurement is

$$y = 6,75 \cdot 10^{-12} \cdot x^{1,89} \quad (2.49)$$

Here the dependency is closer to a quadratic one than before at 1200 nm, but still there seems to be a linear term. But as 1500 nm is further away from the energy gap wavelength of the PIN diode, the linear factor does not contribute as much as in the measurement with the fundamental wavelength of 1200 nm. Since in both cases linear and second harmonic processes seem to be present a second fit of the form

$$y = ax + bx^2 \quad (2.50)$$

is performed and is shown in Figure 2.23 (b). This leads to

$$y = 3,85 \cdot 10^{-11}x + 4,42 \cdot 10^{-12}x^2 \quad (2.51)$$

for the fundamental wavelength 1200 nm and

$$y = 4,49 \cdot 10^{-12}x + 4,83 \cdot 10^{-12}x^2 \quad (2.52)$$

for 1500 nm .

In both cases, the second order terms have the same order of magnitude (10^{-12}), but for the shorter fundamental wavelength the linear term is one order higher as the second harmonic term and as the linear term of the longer wavelength. As mentioned before this can be explained with the energy band gap of the PIN diode at 950 nm , which is quite close to 1200 nm and therefore linear processes are more likely to appear than for 1500 nm . The longer the wavelength the less linear processes are generated.

To be able to compare these measurements to the actual performance of the diode, the beam of a laser diode in the visible regime (635 nm) is focused onto the diode. Figure 2.23 (c) shows the measured result and the fitted curve. It is important to notice that the power of the laser beam used here is set to powers three orders of magnitude lower than in the measurements before. The linear fit for this measurement is

$$y = 1,11 \cdot 10^{-10}x \quad (2.53)$$

The fit to the data points shows that the current almost increases linearly with the power, which was expected. This shows that for higher wavelength in the infrared regime there is indeed SHG generated that do not appear for shorter wavelengths in the visible regime.

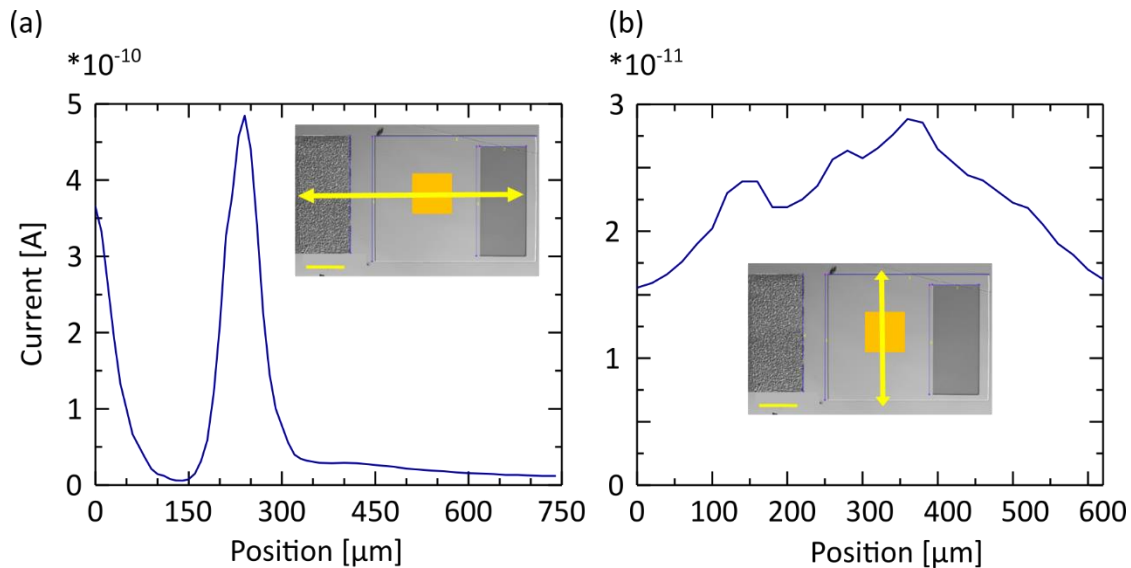


Figure 2.24: Current measurement of local scan over PIN diode including contacts and antenna field (a) Scan from n-type contact to p-type contact (b) scan perpendicular to previous one.

As this still does not explain why there is no clear difference between the measurements on the antenna fields and on the pure PIN diode a local scan over the diode is performed. A line scan over one diode from contact to contact and in the perpendicular direction is executed. In both cases, the beam passes the antenna field. To realize the scan the sample is moved via the translation stage in steps of $10\ \mu\text{m}$ in x - and y -direction respectively. The exciting wavelength is set to $1200\ \text{nm}$ with a power of $5\ \text{mW}$.

Figure 2.24 shows the results of both measurements. In Figure 2.24 (a) $0\ \mu\text{m}$ on the position axis corresponds with the left edge of the n-type contact, whereas $730\ \mu\text{m}$ corresponds approximately with the right edge of the p-type contact. There are two steep risings of the current, which seem to correspond to the n-type contact. Towards the p-type contact, the current is constantly decreasing. Figure 2.24 (b) shows the scan in the perpendicular direction. Here the current decreases towards the edges of the diode, but the nano antenna field does not seem to have any influence. As the current rising in figure (a) cannot be explained a larger scan is performed, which is depicted in Figure 2.25. Again $0\ \mu\text{m}$ on the position axis refers to the left edge of the n-type contact of the contacted PIN diode. For a better understanding, the sample's design is sketched under the position axis correspondingly. Only the diode depicted on the right is contacted. The sample is scanned over a not contacted diode as well that is on the left of the sample. In the figure it lies approximately between -1250 and $-800\ \mu\text{m}$ (blue area). In between the two diodes, there are four fields that are etched to the n-type layer, which are depicted in black. The light grey fields on the blue depicted diodes correspond to the gold contacts on the p-type semiconductor.

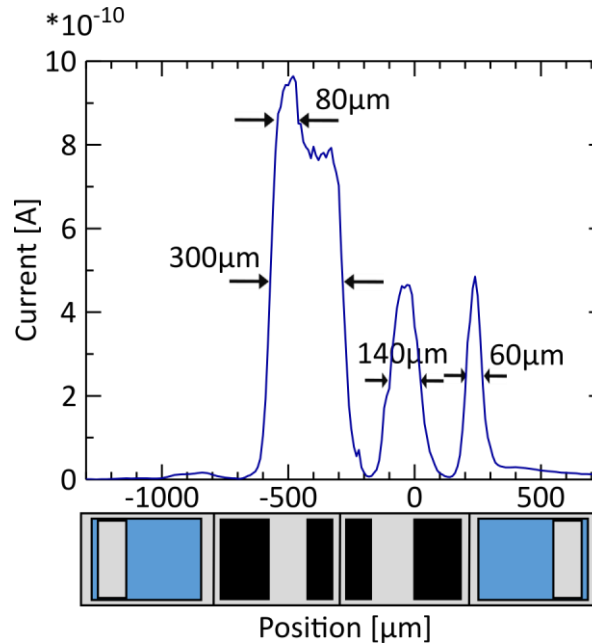


Figure 2.25: Current measurement scan over two diodes (blue areas). Only the diode on the right is contacted. The black areas are etched to the n-type GaAs. The grey areas on the blue diodes are gold contacts.

Again the exciting wavelength is set to 1200 nm with an average power of 5 mW . The stage is moved in steps of $10\text{ }\mu\text{m}$. The measured current shows three peaks, where the current is approximately one order higher compared to the rest of the measurement. The two peaks to the right (at around 0 and $250\text{ }\mu\text{m}$) seem to correspond to the areas where there is neither contact nor diode, as their FWHM (full width half maximum) corresponds to the widths of these areas (compare with Figure 2.18 (b)). However, the peak to the left (from around -600 to $-300\text{ }\mu\text{m}$) does not seem to have this correspondence. It seems to arise after the first n-type contact from the left and ends between the two middle n-type contacts and therefore one contact lies in between. Whereas the other two current peaks on the right end at n-type contacts respectively. Additionally the current there is around a factor two smaller compared to the left peak.

In short conclusion, it is not clear what causes those peaks that arise in the current measurement of the scan over the sample. Not only do they not appear on areas that have the same components, but furthermore arise even though the area that is illuminated should not influence the contacted PIN diode at all.

2.4.3 Discussion of results

To be able to use a PIN diode with a band gap energy at around $1,3\text{ eV}$ (equals $\sim 950\text{ nm}$) as an infrared detector gold nano antennas are fabricated on top of said diode. These antennas are designed to be resonant in the infrared and vary in form and size. Their strong electric near field is supposed to enhance any nonlinear effect and partially their design generates SHG itself (see chapter 2.5).

After the current measurement of the contacted diode with and without antenna fields, no obvious difference can be seen. However, the signal is not linear but rather a composition of linear and SHG effects.

A scan over the diode and the whole sample shows that the measured current signal is highly dependent on the position that is illuminated. Even regions that do not belong to the contacted diode can induce high currents when excited. As for this behavior, the interpretation of the data is difficult. At wavelengths close to the band gap the linear behavior of the measured current dominates and the higher the wavelength the higher the second harmonic term. Nevertheless, this behavior is the same for illumination of the pure PIN diode and an additional antenna field fabricated on top of the diode.

2.5 NONLINEAR SELECTION RULES

Plasmonic nano antennas do not only enhance nonlinear generation processes in other materials with their strong electric near field enhancement, but they can generate nonlinear light by themselves. However, as mentioned before, like in crystals the nonlinear processes underlie some selection rules based on the symmetry of the crystal lattice or of the nanoantennas, respectively. Second harmonic generation for example needs antennas that break symmetry [Blo99]. Furthermore, there are differences concerning the polarization of the incident light. Hence, the two cases, circularly and linearly polarized light, have to be described differently.

To fully understand the problem, equation (2.39) can be written in its components in a general coordinate system [Bha72]

$$P_i = \chi_i^j E_j + \chi_i^{jk} E_j E_k + \chi_i^{jkl} E_j E_k E_l \quad (2.54)$$

Summation over repeated indices is implied. The electric field and the polarization are covariant vectors, what leads to mixed susceptibility tensors. χ_i^{jk} for example, is covariant in one and contravariant in the other index. For linear polarized light, the most convenient choice is a Cartesian coordinate system. The z -axis is chosen to be parallel to the propagation direction of the incident light and the polarization is parallel to either the x - or y -axis. Considering a nonlinear crystal, the propagation direction of the incident light is supposed to be along the symmetry axis. In the following, observations are made in forward direction.

Neumann's principle says that all physical crystal properties should show the symmetry of the crystal [Neu85]. For a nonlinear generation tensor of a distinct order, this means that a certain point group symmetry has to be invariant under all symmetry operations of said point group. Therefore, a particular harmonic generation is either present or absent, depending on the value of the appropriate tensor (non-zero or zero). In centrosymmetric crystals for example, all tensor components of χ_i^{jk} are zero, which leads to an absent second harmonic generation.

Using a transformation equation like

$$x'_i = A_i^j x_j \quad (2.55)$$

the tensor components in a general coordinate system x_1, x_2, x_3 transform to

$$\chi_i^{jk} = A_i^p A_q^j A_r^k \chi_p^{qr} \quad (2.56)$$

For a Cartesian coordinate system, there is no distinction between co- and contravariant indices, which leads to

$$\chi'_{ijk} = A_{pi}A_{qj}A_{rk}\chi_{pqr} \quad (2.57)$$

With this transformation and the Neumann's principle, it is now possible to determine the non-zero components of the corresponding tensor. For particular problems, not all non-zero components are of interest. Taking for example the simplest problem of SHG. Here, only the components χ_{111} , χ_{122} , χ_{211} and χ_{222} need to be studied. If now $\chi_{111} \neq 0$ and remains invariant for all generating operations of the point group, incident light polarized in x -direction generates a second harmonic signal with the same polarization. For $\chi_{211} \neq 0$ the same applies for polarization in y -direction.

Cyclic group C_p	Other groups akin to C_p	Order of harmonic					
		2	3	4	5	6	7
C_1	C_p	X					
C_2	C_i C_{2h}	0	X				
	C_{2c} D_2 D_{2h}	0	+				
	T T_h						
C_3	C_{2h}	X	X	X			
	C_{3v} D_3 D_{3h}	+	+	+			
C_4	C_{4h} S_4	0	X	0	X		
	C_{4v} D_4 D_{4h}	0	+	0	+		
	D_{2d}						
	T_d O O_h						
C_6	C_{6h} C_{3l}	0	X	0	X	0	X
	D_{3d} C_{6v}	0	+	0	+	0	+
	D_6 D_{6h}						
	$3D$	0	+	0	+	0	+

Table 2.1: Presence (+) or absence (0) for 32 crystal classes under illumination with linear polarized light [Bha72.]. "X" signifies elliptical polarization. After the harmonics of the order $p + 1$ results repeat themselves.

These considerations can be made for different crystal classes and harmonics of any order. Table 2.1 shows the possible and not possible harmonics for 32 different crystal classes. "0" signifies that the particular harmonic is forbidden for the corresponding crystal

structure."+" means that the harmonic is present and polarization of the incident light is preserved. Harmonics marked with "X" show an additional polarization to the one parallel to the incident light, which is perpendicular to it and therefore generally exhibits an elliptical polarization. For all cyclic groups C_p results are only given for harmonics of the order $p + 1$, as results repeat themselves thereafter. The results for isotropic media (3D) are also shown. Considering the cyclic groups C_2, C_4, C_6 and 3D one can see that they do not exhibit even harmonics.

Concerning right or left circular polarized incident light with propagation direction along the symmetry axis, the coordinates 1, 2 and 3 can be defined as

$$x + iy, x - iy \text{ and } z \quad (2.58)$$

With this the components of the incident light vector are

$$E_1 = E_x + iE_y; E_2 = E_x - iE_y; E_3 = E_z \quad (2.59)$$

and therefore describe left and right circular polarized light, respectively. A rotation of the angle φ around the z-axis transforms the coordinates to

$$E'_1 = e^{-i\varphi} E_1; E'_2 = e^{i\varphi} E_2; E'_3 = E_3 \quad (2.60)$$

For these coordinates, the transformation matrix is diagonal, which leads to a distinction between co- and contravariant indices. Considering again the easiest case of SHG, only the components like $\chi_1^{11}, \chi_2^{11}, \chi_1^{22}$ and χ_2^{22} are of interest. For higher harmonics, this means that only components of this kind are important. For the n 'th harmonic (given by the component $\chi_{1or2}^{11...}$ n times) this leads to the following transformations

$$\chi_1'^{11...} = e^{i\varphi} e^{-in\varphi} \chi_1^{11...} = e^{-i(n-1)\varphi} \chi_1^{11...} \quad (2.61)$$

$$\chi_2'^{11...} = e^{-i\varphi} e^{-in\varphi} \chi_2^{11...} = e^{-i(n+1)\varphi} \chi_2^{11...} \quad (2.62)$$

Therefore, the n 'th harmonic exists with the same circular polarization state as the incident light when $\chi_1^{11...}$ survives. The polarization state changes when $\chi_2^{11...}$ survives.

Table 2.2 shows the results for circular polarized light. As before "0" indicates that the corresponding harmonic is forbidden. Crystal structures marked with "+" generate the corresponding harmonic with the same polarization state as the incident light, whereas "-" signifies that the polarization state changes for example from left to right circular. Both states are present for structures that are marked with "X" resulting generally in an elliptically polarized state.

The following transformation rules for the tensor components apply for the cyclic groups

$$n - 1 = 2l \pi/2 \quad (2.63)$$

$$n + 1 = 2l \pi/2 \quad (2.64)$$

with l as an integer. If equation (2.63) is satisfied the polarization state is preserved, whereas it changes in equation (2.64). If neither of the two equations can be fulfilled, the harmonic is forbidden. Again even harmonics are absent for the cyclic groups C_2, C_4, C_6 and $3D$.

Cyclic group C_p	Other groups akin to C_p	Order of harmonic					
		2	3	4	5	6	7
C_1	C_p	X					
C_2	$C_i \quad C_{2h}$ $C_{2c} \quad D_2 \quad D_{2h}$ $T \quad T_h$	0	X				
C_3	$C_{3v} \quad C_{3h}$ $D_3 \quad D_{3h}$	-	0	+			
C_4	$C_{4h} \quad C_{4v}$ $S_4 \quad D_4 \quad D_{4h}$ D_{2d} $T_d \quad O \quad O_h$	0	-	0	+		
C_6	$C_{6h} \quad C_{6v}$ $D_6 \quad D_{6h}$ $C_{3i} \quad D_{3d}$ $3D$	0	0	0	-	0	+
		0	+	0	+	0	+


Table 2.2: Presence (same polarizaiton “+”, opposite polarization “-”) or absence (0) for 32 crystal classes under illumination with circular polarized light [Bha72]. “X” signifies elliptical polarization. After the harmonics of the order $p + 1$ results repeat themselves.

Transferring this concept onto plasmonic nanoantennas Alon et al describes the selection for high harmonic generation for centrosymmetric structures for circularly polarized light [Alo98] with

$$n = ml \pm 1 \quad (2.65)$$

with the order of the nonlinear process n , the order of symmetry m and an integer l . “+” and “−” correspond to the harmonic generation of the same or different polarization state, respectively.

Table 2.3 shows possible harmonic generations for different centrosymmetric nano-antennas under illumination with circularly polarized light. “ σ ” implies that the polarization state of the harmonic generation is the same as the that of the incident light. “ $-\sigma$ ” inverses the polarization for example from left to right polarized light. In the following experimental part, we focus on fourth harmonic generation with inverted polarization, which out of the depicted antennas is only possible with a five-fold rotational symmetry (C5).



	C2	C3	C4	C5
2 nd harmonic generation				
		3 θ ($-\sigma$)		
3 rd harmonic generation	2 θ (σ)			
	4 θ ($-\sigma$)		4 θ ($-\sigma$)	
4 th harmonic generation		3 θ (σ)		5 θ ($-\sigma$)
5 th harmonic generation	4 θ (σ)		4 θ (σ)	
	6 θ ($-\sigma$)	6 θ ($-\sigma$)		
6 th harmonic generation				5 θ (σ)

Table 2.3: Possible harmonic generations for different antennas symmetries under illumination with circular polarized light [Li15].

The above described selection rules only concentrate on the symmetry on the most fundamental level, the symmetry of one single antenna. For plasmonic structures a macroscopic symmetry is of importance as well, as LSPP are very sensitive to size, shape and surrounding material [Kau12]. If the antennas are now arranged in a lattice with the same rotational symmetry, the same selection rules apply as the ones on the microscopic level [Che14b]. For example, third harmonic can only be generated under illumination with circular polarized light when the single antennas (meta-atoms) are arranged in two- or fourfold symmetry. For a threefold symmetry it is forbidden. These are the same selection rules as the ones on a microscopic level.

2.5.1 Fabrication

For measurements of the fourth harmonic generation, several different arrays are fabricated. On the one hand, the arm length of the star like C5 antennas varies and on the other hand, the arrangement of the antennas differs. In some arrays, the antennas are arranged quadratically with periods of $1\ \mu\text{m}$ in both x - and y -direction. The size of the fields is $100 \times 100\ \mu\text{m}^2$. The other arrangement is designed after a Penrose lattice, as this corresponds to a five-fold macroscopic symmetry, as nonlinear processes are not only governed by selection rules that are imposed by the molecular configuration (which means the antenna design itself) but as well by the macroscopic symmetry of the investigated structures as mentioned before.

On the first sample, the antennas are made of gold and the arm length of the antennas varies from 190 to 240 nm. All lengths are fabricated with two different arm width 40 and 50 nm. The height is fixed to 30 nm.

The antennas are fabricated via electron beam lithography (EBL) (see Figure 2.26). For this purpose a glass substrate with a 20 nm thick Indium Tin Oxide (ITO) layer on top, is spin coated with PMMA 950k. The ITO layer serves as a conducting layer, which is necessary for EBL. The positive electron beam resist is exposed with a dose of $280\ \mu\text{C}/\text{cm}^2$ and an acceleration voltage of 20 keV. After the development, 2 nm of chromium and 30 nm of gold are evaporated onto the sample via electron beam evaporation. The chromium serves mainly as an adhesive layer and due to its marginal thickness it can be neglected in the following evaluation. After the evaporation, the samples are put into acetone where the so-called lift off takes place. The acetone removes the resist and with it, every metal that was on top of it, is detached from the substrate. Only the metal that is located on the exposed areas of the electron beam remains.

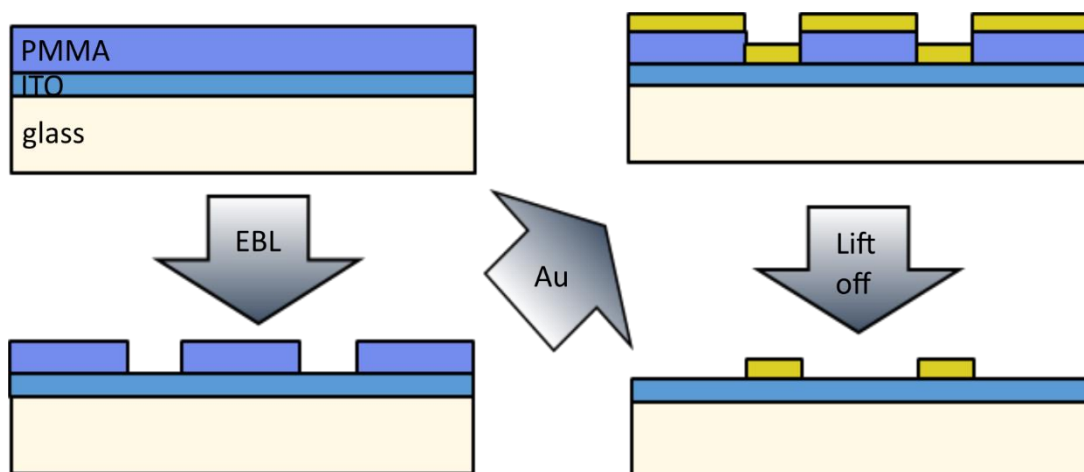


Figure 2.26: Schematic of the EBL and lift off process for the fabrication of the C5 gold antennas on a glass/ITO substrate.

As an example Figure 2.27 shows some SEM images of the quadratically arranged antennas. Image (b) and (c) show that the structures' widths are actually wider than

expected. This results in a slightly blue shifted resonance wavelength. However, as in our nonlinear measurement setup the fundamental wavelength is tunable it is not of importance for the experiment.

Later a second sample is produced with silver antennas instead of gold. As silver tends to react with the sulfur in air quite quickly, a passivation layer of hafnium oxide (HfO) is evaporated on top of the silver. As the use of silver results in different resonance frequencies as well, the arm length of the C5 antennas is changed to 180 to 220 nm. On this sample the antennas are again arranged either quadratically or in a Penrose lattice like symmetry.

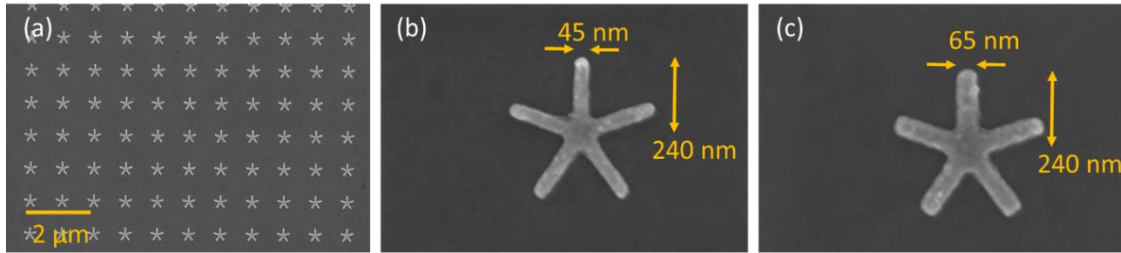


Figure 2.27: SEM images of quadratically arranged C5 gold antennas on a glass/ITO substrate (a) antennas with a period of 1 μm in x- and y direction. (b) and (c) Close up of 240 nm long gold antennas with different arm width (45 and 65 nm).

2.5.2 Fourier-transform infrared spectroscopy

Before the nonlinear measurements, one needs to know the linear properties of the sample. For that purpose, the antennas are analyzed with a Fourier-Transform Infrared Spectrometer (FTIR). This technique is widely used for the investigation of transmission and reflection spectra in the infrared as well as in the visible spectral region. In the following its working principle will be discussed.

In contrast to a dispersive spectrometer, where the different wavelengths of light have to be separated with diffraction gratings or prisms, the FTIR is based on a Michelson-Interferometer. The main components of this interferometer are two mirrors and a 50/50 beam splitter. The light source needs to be as broadband as possible and often tungsten or xenon lamps are used. First, the beam that has to be analyzed passes the beam splitter and one part is deflected onto a locally constant mirror. The other part passes through the beam splitter onto a second mobile mirror. Afterwards both beam parts recombine and interfere. The movement of the second mirror leads to an alternating constructive and destructive interference of particular wavelengths of the exiting beam. This intensity of the interfered light beam is detected with a photo diode in dependence of the movement of the mirror. In the end, the corresponding reflection or transmission spectra can be calculated with the Fourier transformation of this interferogram [Sal91, Smi11].

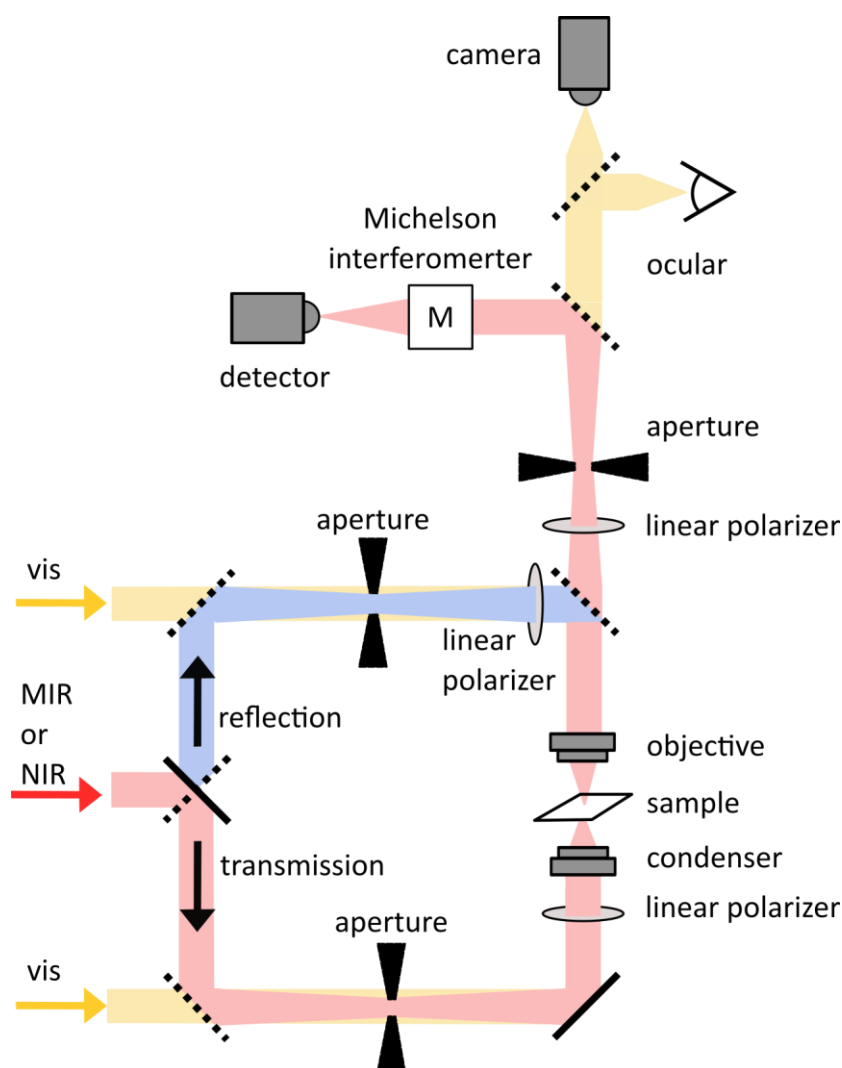


Figure 2.28: Schematic of the used FTIR setup, a combination of the Bruker Hyperion 1000 and the Vertex 70. The dotted lines refer to foldable mirrors that serve to adjust the beam path.

The FTIR measurements of this work are executed on a commercially available device by the company Bruker Corporation. It is a combination of the spectrometer “Vertex 70” and the microscope “Hyperion 1000”, which enables the user to locally investigate the transmission and reflection properties of selected parts of the sample. There are three light sources available, a silicon carbide source for the Mid-infrared spectral range, a tungsten light source for the near infrared spectral range and a halogen light source for the ultra violet and the visible spectral range. With a hinged mirror, the user can choose between reflection or transmission measurements (see Figure 2.28). In both beam paths, a linear polarizer can be used to polarize the incident light. The condenser in the transmission path enables the user to focus from below onto the sample’s surface. The microscope objective above the sample with a numerical aperture of 0,5 (which corresponds to a detection angle of around 60°) collects and parallelizes the transmitted light. The same objective is used for excitation and detection in the case of a reflection measurement. After passing this objective both possible light beams pass an aperture that can confine the analyzed area on the sample. Then a set of parabolic mirrors transfers the

signal to a Michelson interferometer. For the detection of the interferogram a few different detectors can be installed, depending on the analyzed wavelength range. In the case of measurements in the infrared spectral range, a liquid nitrogen cooled MCT-detector is used (quicksilver-cadmium-tellurite-detector). There is also a silicon-diode available that is used in the visible range. By turning the mirror that leads the beam to the detector, the user is able to switch to the imaging mode, through either the microscope ocular or a camera. A visible light source illuminates the sample that can be moved in x - and y -direction with a motorized stage. With the afore mentioned aperture the structured areas of the sample can be analyzed.

2.5.3 Linear measurements

For the later nonlinear measurements, it is important to know the resonance frequencies of the antenna fields. That is why the structures' transmission is measured with the above described FTIR method. In this case, the tungsten NIR source and the MCT detector are used. The beam is unpolarized. The aperture is set to around $80 \times 80 \mu\text{m}^2$ and ensures that only the selected antenna field is illuminated. The transmission of the pure substrate is measured as well and serves as a reference for the transmission of the structured fields. The resulting transmission is then calculated by

$$T = \frac{I}{I_0} \quad (2.66)$$

with the measured intensity through the structured fields I and the reference intensity I_0 of the substrate.

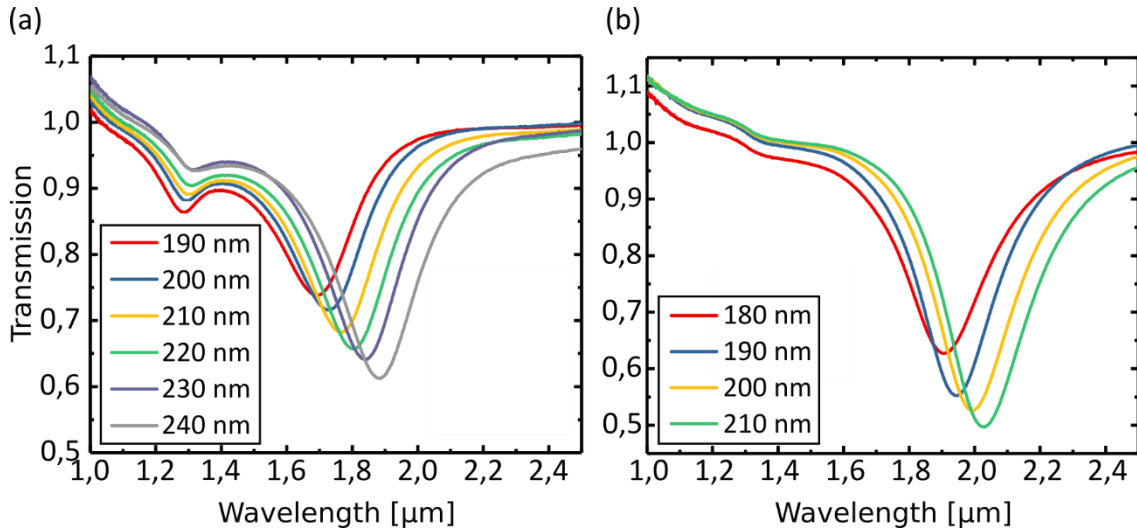


Figure 2.29: Measured transmission spectra of C5 nano-antennas (a) made of gold with an arm width of 65 nm and (b) made of silver with an arm width of 80 nm on a glass/ITO substrate.

Figure 2.29 shows transmission spectra of gold antennas with an arm width of 65 (a) and of silver antennas with a width of 80 nm (b) with varying arm lengths from 190 to

240 nm and 180 to 210 nm, respectively. As the resonant excitation of SPPs results in a redistribution of the electric field, the transmitted intensity is reduced. Therefore, the dip in each spectrum corresponds to the resonance frequency of the antennas. As expected the wavelength redshifts with increasing arm length. As the period remains constant, the total coverage of the substrate increases with increasing arm length. That is why the transmission at the resonance frequency drops with increasing arm length. As depicted in Figure 2.30 the resonance wavelength increases approximately linear with the length, as it is the case in the classic antenna theory as well [Stu12]. Comparing two different arm width of gold nanoantennas the resonance wavelength of the 65 nm wide antennas is always a bit shorter than that of the 45 nm wide antennas with the same arm length. This corresponds with the analytical approximation for optical nanoantennas of Novotny [Nov07] that states that the resonance wavelength of a metallic and cylindrical dipole antenna is inverse proportional to its diameter. It also states that is proportional to the antenna length, which also corresponds with the measured results.

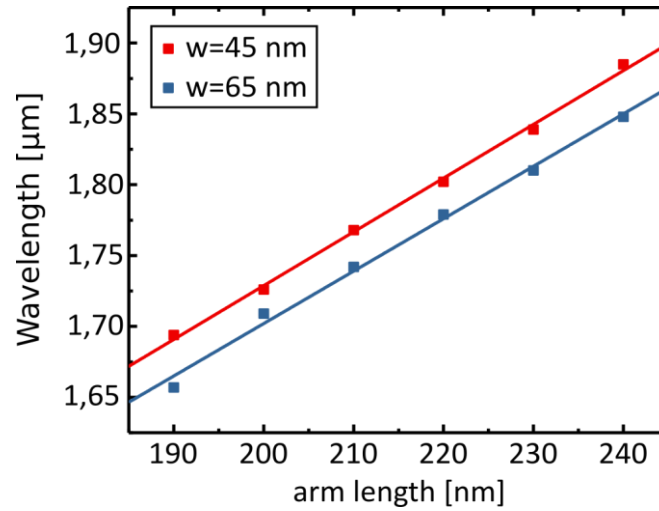


Figure 2.30: Plasmon resonance wavelength over the arm length of C5 nano antennas with an arm width of 45 and 65 nm. The squares depict the experimentally determined results and the lines the corresponding linear fit.

2.5.4 Nonlinear measurements

With the knowledge of the resonance wavelength, it is now possible to measure the nonlinear behavior of the nanoantennas. As all resonances lie in the infrared spectral range, the OPO is used. As described in chapter 2.2.2 the signal laser light lies in the range from 1000 to 1600 nm, but as the resonance wavelengths are even longer, the idler has to be used, whose range is from 1600 to 4000 nm. The exiting laser beam of the OPO is normally already linear polarized and with a $\lambda/2$ -waveplate this polarization can be changed to the preferred direction (see Figure 2.31). An optional $\lambda/4$ -waveplate can convert the linear polarization into a circular state. A lens with a focal length of $f = 100$ mm focuses the beam onto the sample, after passing a long pass filter (LP) that eliminates eventually generated nonlinear signals by optical components in front of the

sample. Behind the sample the signal is collected and parallelized by a 20 x microscope objective with a numerical aperture $NA = 0,45$ (which corresponds to a detection angle of around 52°). A second lens then couples the laser beam into the spectrometer that uses a 150 *lines/mm* lattice and a Newton EMCCD camera for the spectral analyses. A short pass filter (SP) in front of the spectrometer blocks the laser light that might disturb the measurement. Furthermore, a hinged mirror behind the objective enables imaging of the sample's surface with a CCD-camera while it is illuminates with an additional white light source.

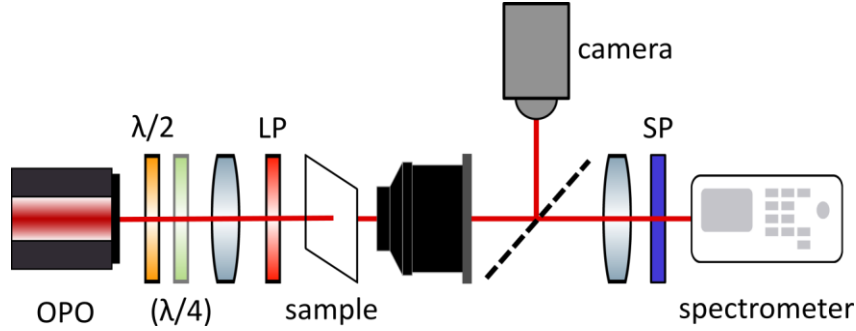


Figure 2.31: Schematic experimental setup for the nonlinear characterization of the C5 nano antennas. After passing a half wave plate and if needed a quarter wave plate, which adjust the desired polarization state, the laser beam is focused onto the sample. A long pass filter in front of the sample filters out all possibly generated nonlinear signals by the optical components in front. An objective collects the light, which is then coupled into a spectrometer after passing a short pass filter. With a hinged mirror behind the objective and a CCD camera, the laser spot's position on the sample can be determined.

As the resonance wavelengths of the different antenna fields are known from chapter 2.5.3, the antennas can now be excited resonantly with a laser power of 55 *mW*. The OPO is set to the desired wavelength and the signal is measured for the different gold antennas. Figure 2.32 (a) shows the nonlinear spectra of gold antennas with an arm width of 45 and length of 240 *nm* for four different incident wavelength (1710, 1860, 1900 and 2000 *nm*). Figure 2.30 shows that the resonance wavelength lies around 1880 *nm* which is why the overall signal for an exciting wavelength of 1860 *nm* is the highest. In this measurement a high peak appears at around 620 *nm*, which corresponds unexpectedly to a third harmonic generation (THG). Even though not resonantly excited this third harmonic signal appears for the other three wavelengths as well, due to the fact, that plasmon resonances are quite broad (see Figure 2.29). As this signal was not expected to arise from the antennas (see Table 2.3), a spectrum of the substrate itself is recorded. Figure 2.32 (b) shows this spectrum next to the one with antennas and one of just the laser without a sample. It can be seen, that THG is already generated in the substrate itself, but it is enhanced by the antennas. As the signal of the laser, which passes all the optical components except for the sample does not show a nonlinear signal, it is safe to say, that the THG arises from the substrate and the antennas.

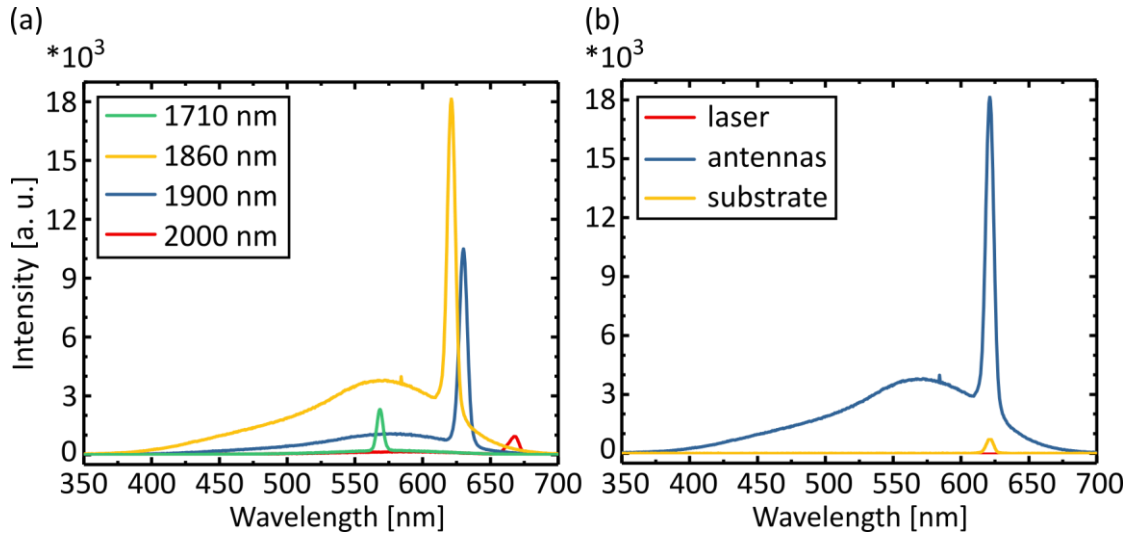


Figure 2.32: Experimental data of the nonlinear characterization of C5 gold nano antennas with an arm length of 240 nm and width of 45 nm (a) for different excitation wavelengths (b) compared to the signal of the pure substrate and the laser itself.

However, the expected fourth harmonic signal, which should be generated for the yellow line (Figure 2.32 (a)) at around 470 nm, does not appear. Yet there is a broad signal from 400 to 700 nm. As this signal is quite strong it is possible, that it covers the fourth harmonic signal, as this is expected to be rather weak.

This signal is caused by interband transitions in the gold antennas. In gold as in other metals conduction and valence band overlap. Yet some of the inner levels do not overlap these bands, as they do not split wide enough. This leads to possible interband transitions in the system that are comparable to those in semiconductors [Dre62]. These transitions between the conduction band and the inner levels cause an absorption edge such as in semiconductors. In some metals, electron decay in these bands induce a weak luminescence. In bulk materials, however, these transitions are quite unlikely. The emission and absorption that are induced by these transitions are extremely weak [Moo69]. In plasmonic antennas, as they are very small and therefore have a reduced number of atoms, the interband transitions are more important.

As this problem is caused by the material, gold is changed to silver, which does not show such signals in this wavelength range. As described before, again samples with two different antenna arrangements are fabricated. The fields' nonlinear characterization is carried out as described before with circular polarized light, only the power is set to 70 mW this time. Figure 2.33 shows the measured signal for antennas with an arm length of 200 nm for two different arrangements and polarization states and an excitation wavelength of 1980 nm. Again only THG is generated at 660 nm. It is a lot stronger at the quadratically arranged fields and the left circular polarization state generates a higher signal for both arrangements. As Table 2.3 shows, THG can be generated by C4-structures and, therefore, the macroscopic symmetry that favors THG is the quadratic arrangement. This explains why the signal in both polarization states is stronger for this arrangement

compared to the Penrose lattice like one. The figure also shows that the silver sample does not generate additional photoluminescence. Unfortunately, a fourth harmonic signal, which should appear at 495 nm , cannot be detected, either.

As the fourth harmonic signal is expected to be quite weak, a higher excitation power might help to generate a detectable fourth harmonic signal. However, as the antennas are made of silver or gold respectively, the pulse duration of 200 fs does not allow the power to be too high, as the metal starts to melt and the antennas are damaged (see Figure 2.33 (b)). With shorter pulses, it would be possible to use a higher excitation power.

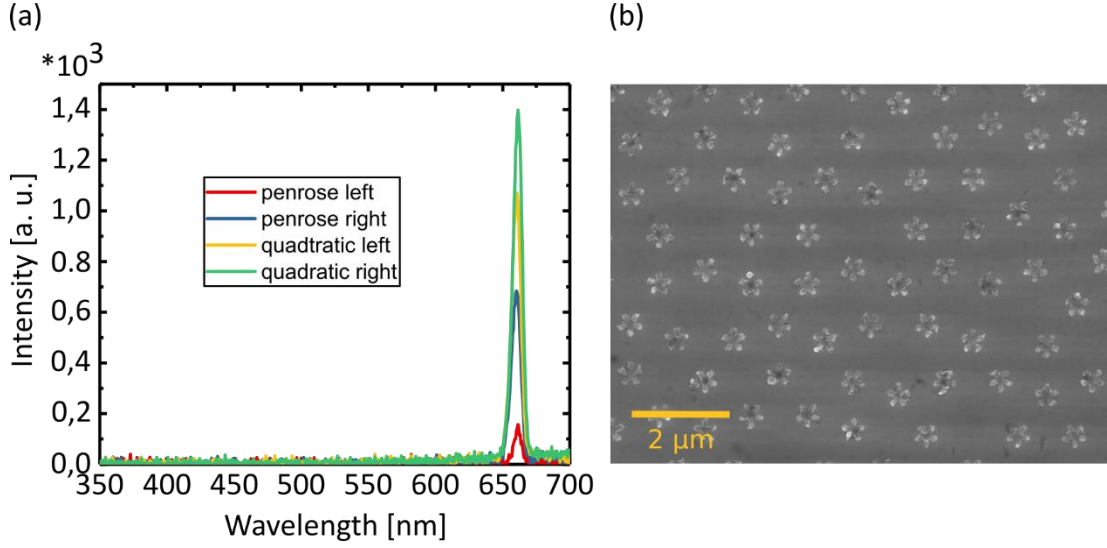


Figure 2.33: (a) Experimental data of the nonlinear characterization of C5 silver nano antennas with an arm length of 200 nm and width of 85 nm with left and right circular polarized light at an excitation wavelength of 1980 nm for different antenna arrangements. (b) Damaged silver antennas after an exposure with an excitement power of 100 mW .

2.5.5 Discussion of results

Concerning the selection rules for harmonic generation the order of centrosymmetry of crystal lattices or plasmonic nanoantennas determines the order of the nonlinear signal. Fourth harmonic signals are therefore supposed to be generated by five-fold symmetric (C5) nanoantennas. A macroscopic symmetry, which for C5 antennas is a Penrose lattice, can even enhance that harmonic signal.

As gold nanoantennas also generate photoluminescence in the range from 400 to 700 nm , where the fourth harmonic signal is supposed to be for the designed antennas, silver is used instead. However, still no fourth harmonic signal can be detected. Instead a third harmonic signal appears which is generated by the substrate material and enhanced by the nanoantennas.

As the antennas start to melt at high laser beam powers of the OPO, which has a pulse duration of 200 fs , the only possible way to detect fourth harmonic signals is to decrease

the pulse duration. Then it would be possible to increase the laser beam power, as the time in which the systems (here the antennas) heats up, is shorter and therefore the antennas would not melt. Unfortunately, such a laser was not available.

3 OPTICAL PHASE CONTROL WITH METASURFACES

Metasurfaces cannot only enhance optical effects with their strong near field or generate harmonic nonlinear signals they are also able to modulate the phase of the incident light and therefore can shape the light either linearly or nonlinearly. One common approach for this manipulation is based on optical subwavelength resonators and the phase discontinuity they cause at an interface between two media [Yu11, Ni12], another one is based on the accumulation of a geometrical phase the so called Pancharatnam-Berry (P-B) phase [Ber84, Pan56].

3.1 PHASE MANIPULATION WITH RESONANCES

Many optical components such as prisms and lenses rely on shaping the wavefront of light. This is achieved by gradually changing the phase along the optical path. Gratings and traditional holograms are based on this principle as well. Metasurface enable abrupt phase changes over the rather short scale of the wavelength. Fermat's principle states that light travelling from point A to point B always takes the shortest optical path $\int_A^B n(\vec{r}) d\vec{r}$ with the local refraction index $n(\vec{r})$. This leads to the laws of refraction and reflection between two media. If the accumulated derivative phase along the optical path is zero $\left(\int_A^B d\varphi(\vec{r}) = 0\right)$ the Fermat's principle exists in its most general form, which is known as the principle of stationary phase. If an abrupt phase shift $\Phi(\vec{r}_s)$ is introduced, it depends on the coordinate \vec{r}_s along the interface. This phase shift can be achieved by engineering the interface with optical resonators. This means that the total phase shift $\Phi(\vec{r}_s) + \int_A^B \vec{k} d\vec{r}$ is stationary for the optical path taken by the light [Yu11] (\vec{k} is the wave vector of the propagating light). This leads to a generalization of the laws of refraction (equations (3.1)) and reflection (equations (3.2)) [Yu11, Yu14]

$$\begin{aligned} n_t \sin(\theta_t) - n_i \sin(\theta_i) &= \frac{1}{k_0} \frac{d\Phi}{dx} \\ \cos(\theta_t) \sin(\theta_t) &= \frac{1}{n_t k_0} \frac{d\Phi}{dy} \end{aligned} \quad (3.1)$$

$$\begin{aligned} \sin(\theta_r) - \sin(\theta_i) &= \frac{1}{n_i k_0} \frac{d\Phi}{dx} \\ \cos(\theta_r) \sin(\theta_r) &= \frac{1}{n_i k_0} \frac{d\Phi}{dy} \end{aligned} \quad (3.2)$$

The definitions of the angles are displayed in Figure 3.1. n_i and n_t are the refractive indices of the incident medium and the transmitting medium, respectively. k_0 is the magnitude of the wave vector \vec{k} and $\frac{d\Phi}{dx}$ and $\frac{d\Phi}{dy}$ are the components of the phase gradient parallel and perpendicular to the plane of incidence. These formulas lead to the

conclusion that light that is either reflected or transmitted at an interface can be bent in any desired direction in their corresponding half space.

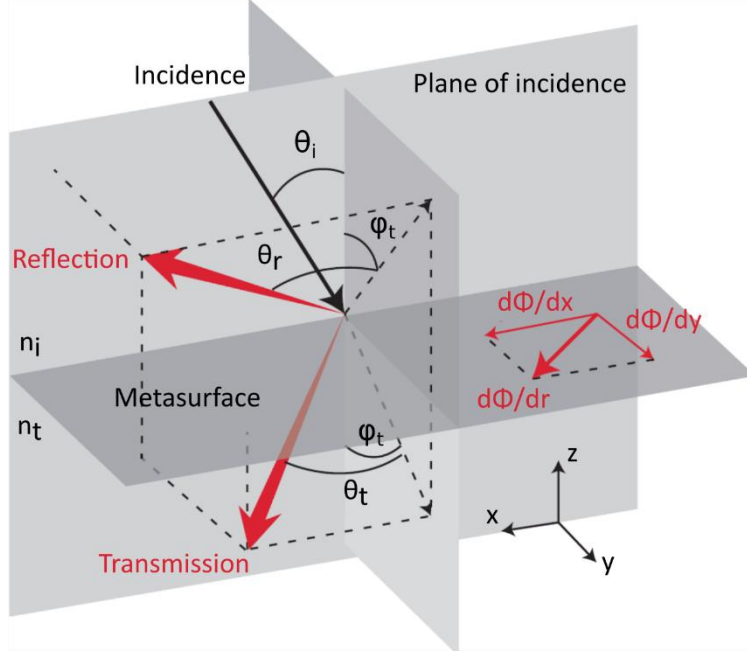


Figure 3.1: Schematics to derive the generalized Snell's law The structured metasurface introduces an abrupt phase shift [Yu14].

To engineer such a surface that follows the generalized laws of refraction and reflection one can use optical scatterers. Those scatterers have to be put into an array to manipulate the whole wavefront. As the scattering amplitudes of the scatterers should be the same and the spacing of the array should be smaller than the incident wavelength, plasmonic nanoantennas are ideally suited. As described in chapter 2.1.2 the energy of the incoming light couples into electromagnetic waves in the metallic antenna, which lead to charge oscillations. These LSPP of the antennas can induce the abrupt phase shifts of the incoming light, as they interact strongly with the light. Considering a dipole nanoantenna and a fixed incident wavelength, the resonance occurs at an antenna length $L_{res} \approx \lambda/2$ with the LSPP wavelength λ that causes the metal's dispersion. This means the excited current in the antenna is in phase with the optical field. By varying the antenna length, one can control the induced antenna current and therefore the resulting phase of the scattered light as well. With dipole antennas with only one resonance the tuning range reaches from 0 to π [Yu14].

Among the many applications of metasurfaces that use the ability to control the phase, they are used to generate holograms [Zhe15, Lar12, Che14a]. It is possible to generate the needed phase profile with different kinds of antenna geometries. As we need a phase tuning range from 0 to 2π dipole antennas are not suitable. In this case, we will concentrate on v-shaped antennas. Contrary to the dipole antennas, they are double resonant [Yu11]. They consist of two arms with an equal arm length h , which enclose an

angle Δ at the end where they connect (Figure 3.2). Defining two unit vectors \hat{s} and \hat{a} perpendicular to each other with \hat{s} is oriented along the symmetry axis of the antenna, one is able to describe the orientation of the v-antenna. As shown in Figure 3.2 the v-antennas have a symmetric and an antisymmetric mode that are excited by components in \hat{s} and \hat{a} direction of the incident electric field, respectively. Concerning the symmetric mode, the current distribution in both arms equals the distribution of individual straight antennas of the same length h . This leads to the first-order resonance at $h = \lambda_{eff}/2$, with the effective wavelength λ_{eff} . [Nov07]. Concerning the antisymmetric mode, the current distribution in each arm comes close to the distribution of the half of a straight antenna with the arm length $2h$. Therefore, the condition for the first-order resonance is $2h = \lambda_{eff}/2$.

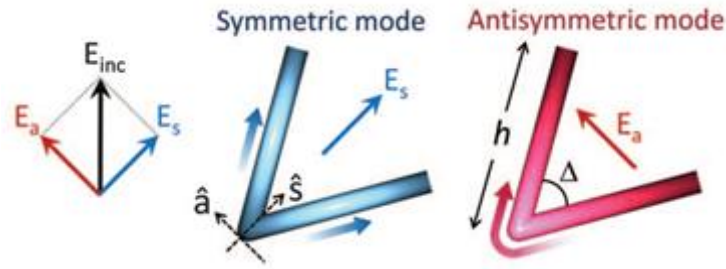


Figure 3.2: V-shaped antennas can be described by their arm length h and the enclosed angle Δ . They support symmetric and antisymmetric modes, which can be excited by components of the incident electrical field along the unit vector axis \hat{s} and \hat{a} [Yu11].h

If the incident light is polarized in \hat{s} or \hat{a} direction, the polarization of the scattered light is the same as the one of the incident light. Every other polarization excites both modes but with different phases and amplitudes caused by their characteristic resonance conditions. Hence, the scattered light can be differently polarized than the incident light. With these modal properties, it is possible to design the polarization state, amplitude, and phase of scattered light with v-shaped antennas. If in the depicted case the incident polarization is 45° and with all the freedoms in choosing antenna geometries (h and Δ), the phases and amplitude of the cross polarized scattered light is designable within a large range for a given excitation wavelength λ_0 . By simply mirroring the antenna, the phase of the cross polarization receives an additional shift of π . Therefore it is possible to achieve a phase coverage of 2π with v-antennas and with a high scattering amplitude as well, what makes them perfect for the use of holograms [Yu11].

3.1.1 Switchable phase holography with hybrid v-shaped nanoantennas

This concept of the v-shaped antennas has been widely used for various holograms [Alm16, Zho13]. In this work, a new approach is investigated, which enables us to fabricate a metasurface that can generate two different, switchable holograms, only depending on the surrounding atmosphere of the sample. This principle relies on the ability of magnesium (Mg) to easily form a hydride (MgH_2) when put into a hydrogen environment,

which results in a phase transition of plasmonic antennas consisting of a gold (Au) and a Mg part. A metasurface that uses this hydrogenation can generate two different holograms, one while residing in air and one while in hydrogen. Mg can absorb up to 7,6 wt % of hydrogen what means that it undergoes a transition from metal to dielectric and forms MgH_2 [Bal09]. With this ability, it is possible to change the plasmonic behavior of an antenna made of Au and Mg.

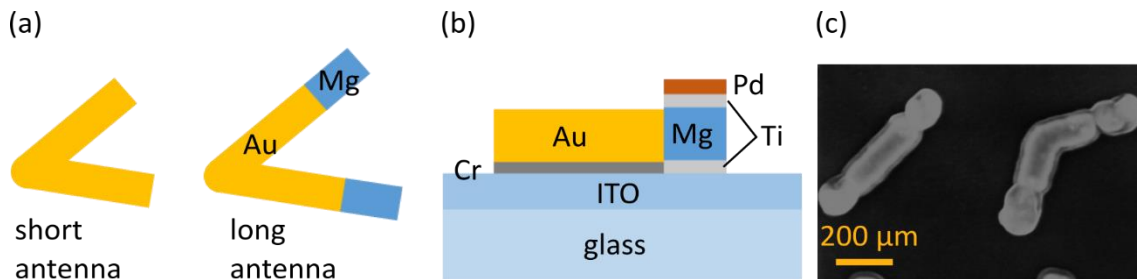


Figure 3.3: Design of v-shaped antennas made of gold and Mg. (a) In air the complete antenna behaves like metal, but putting it into a hydrogen environment, the Mg part of the antenna becomes dielectric and only the here shown short antenna stays actively plasmonic. This leads to a phase shift of the scattered light of $\pi/2$. (b) Side view of antenna. Short antenna is made of 2 nm Cr adhesion layer and 50 nm Au. Dynamic part of the antenna consist of a 2 nm Ti adhesion layer, 50 nm Mg, another 2 nm Ti layer and 5 nm of Pd. The Ti layer between Mg and Pd prevents the two from alloying (c) SEM image of short Au antennas with Mg extension.

Figure 3.3 shows the used design of the v-antennas. They consist of a Au part (here: short antenna) and at the end of both arms some Mg extends the arm length. In normal air environment, the Mg shows plasmonic behavior that means the long plasmonic antenna (Au + Mg) determines the resonance and phase. If put in a hydrogen environment, the Mg becomes MgH_2 and loses its plasmonic properties. Therefore, only the small antenna is responsible for plasmonic resonance and phase of the scattered light. As mentioned before v-shaped antennas offer many possibilities to design resonance, phase and polarization. Therefore, the antennas of the hologram metasurface are designed in a way that the short and long antenna have the same resonance wavelength. Furthermore, the design ensures that the long antenna with the Mg exhibits an additional phase of $\pi/2$ compared to the short antenna, which leads to two different holograms for the hybrid Au/Mg and pure Au antennas.

The corresponding metasurface to the hologram is determined by simulations with a finite difference time domain (FDTD) method. Figure 3.4 shows a flow chart of the program that is characterized by the construction of an iterative loop between two hologram planes and two reconstruction planes. The key aspect of this iterative algorithm is to set quantified phase relations between two holograms. By selecting random pixels (equal to half of the total number of the hologram), we can achieve phase conversion between the two hologram planes, which will result in the reconstruction of two totally different holographic images. This means, that half of all pixels in the hologram are selected randomly before the iteration and then only these pixels change their phase at the

hologram plane, which means that a delay of $\pi/2$ is added or subtracted in conversion steps I or II, respectively. This ensures that the optimized phase profiles of the two holograms have a phase difference of $\pi/2$ on half of the pixels while the rest of the pixels stay the same. This is a requirement for the construction of a dynamic tunable metasurface that is able to generate two different holograms with high quality and uniformity.

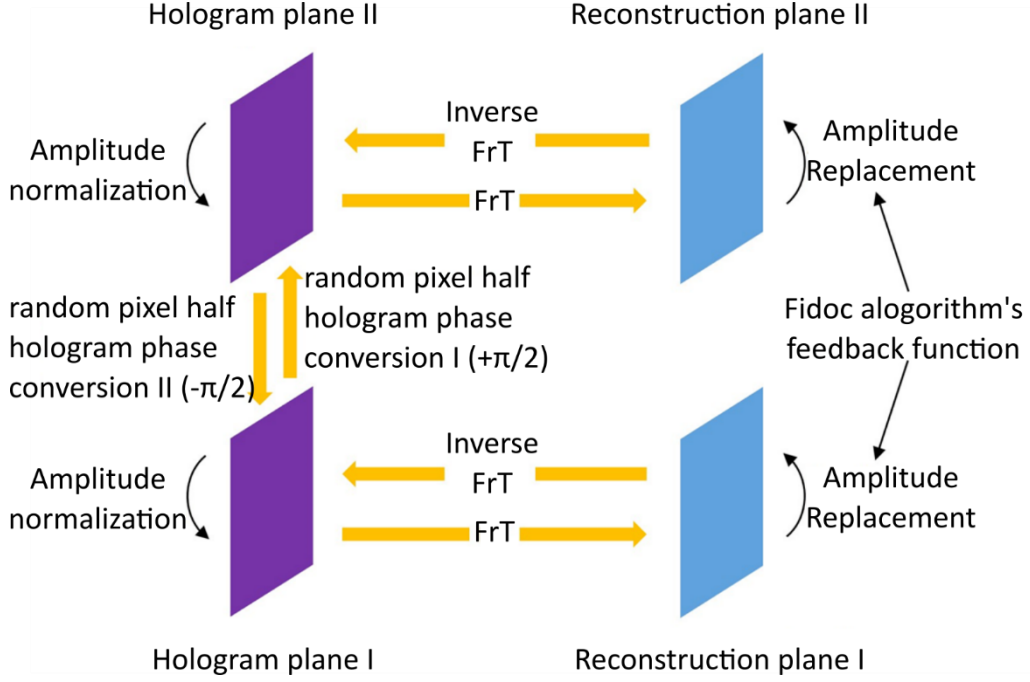


Figure 3.4: Flow chart of the used iterative algorithm to simulate the metasurface and the generated hologram.

As the hologram is chosen to be reconstructed in the near field, the light propagation during the iteration is simulated by the Fresnel diffraction formula

$$U_d(x, y) = \frac{\exp(jkd)}{jkd} \exp\left[\frac{jk}{2d}(x^2 + y^2)\right] \times \iint \left\{ U_0(x_0, y_0) \exp\left[\frac{jk}{2d}(x_0^2 + y_0^2)\right] \right\} \times \exp\left[-j2\pi\left(x_0 \frac{x}{\lambda d} + y_0 \frac{y}{\lambda d}\right)\right] dx_0 dy_0 \quad (3.3)$$

with the complex amplitude in the hologram and the object plane U_o and U_d , the wave vector k , the coordinates of the metasurface hologram (x_0, y_0) and the coordinates of the reconstruction plane (x, y) . With a Fourier transformation, this formula can be optimized for a faster calculation time.

$$U_d(x, y) = \frac{\exp(jkd)}{jkd} \exp\left[\frac{jk}{2d}(x^2 + y^2)\right] \times F\left\{ U_0(x_0, y_0) \exp\left[\frac{jk}{2d}(x_0^2 + y_0^2)\right] \right\} \quad (3.4)$$

With the use of the Fresnel diffraction formula the propagation of light can be the simulated conveniently.

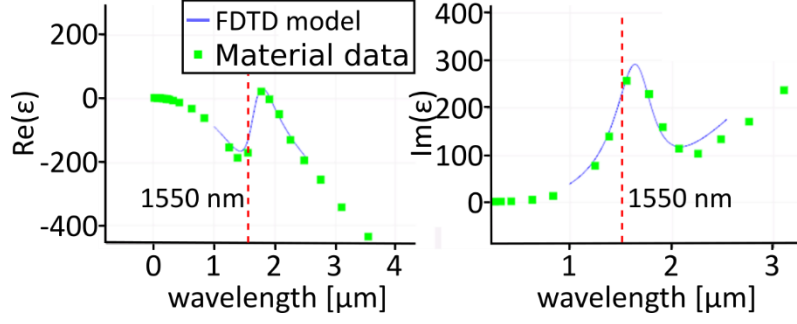


Figure 3.5: Real and imaginary part of the dielectric function of magnesium.

To fabricate the calculated metasurface, suitable antenna length have to be determined. For the simulation one needs the material properties of Mg. Figure 3.5 depicts the real and imaginary part of the dielectric function of Mg, with data retrieved from the Lumerical FDTD database. Compared to the dielectric function of Au in the Drude model (see Figure 2.2 (a)), the material is more lossy especially in the infrared regime. Nevertheless, as the antennas are supposed to be resonant at 1550 nm ($\approx 0,8\text{ eV}$) only the behavior at this point is of importance. Using equation (2.17) with the parameters for Au ($\omega_p = 1,366 \cdot 10^{16}$ and $\gamma = 3 \cdot 4,75 \cdot 10^{13}$) leads to

$$\varepsilon_{Au}(\omega) = -124 + 15i \quad (3.5)$$

The data for Mg retrieved from Figure 3.5 leads to

$$\varepsilon_{Mg}(\omega) = -155 + 210i \quad (3.6)$$

As the real parts of the dielectric function for Au and Mg are quiet similar, one can assume that the plasmonic properties of Mg are similar to that of Au as well and therefore only the data of Au is used for the simulation. Figure 3.6 (a) and (b) show these simulations of amplitude and phase for v-shaped antennas with different lengths L and different angles θ for an incident wavelength of 1550 nm , which are executed via a parameter sweep. Here, points with approximately the same amplitude and a phase shift of $\pi/2$ are chosen. Four examples are marked in Figure 3.6 with the numbers 1 to 4. The yellow dots represent the short, while the red dots represent the long antennas. For the reconstruction of a hologram, it is essential to be able to control the phase over 2π . In this special case, this controllability needs to be present for the short and the long antennas. Figure 3.6 (c) shows some examples how the antennas need to look like to generate the chosen phases. The long and short antennas naturally always have the same angle, as this cannot be changed. Only the length difference shifts the phase by $+\pi/2$.

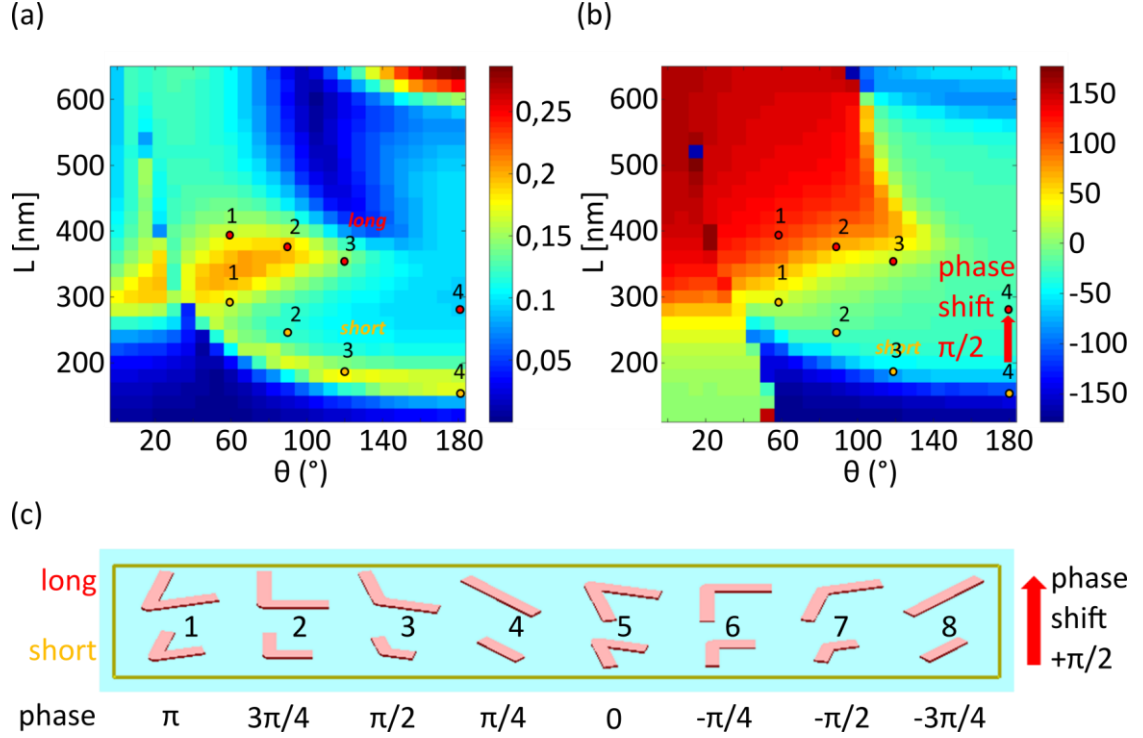


Figure 3.6: Simulation of (a) the amplitude of v-shaped antennas with different length L and angles θ (b) of the phase of the same antennas (c) Designs for short and long antennas with different geometric P-B phases from π to $-3\pi/4$ and $\pi + \pi/2$ to $-3\pi/4 + \pi/2$, respectively.

Table 3.1 shows the corresponding length and angle for the antennas shown in Figure 3.6 (c). Next to the angle θ that is enclosed by the two antenna arms, the angle β plays an important role. This is the angle between the symmetry axis of the antenna and the y -axis, which is perpendicular to the electrical field in y -direction. With these calculated values, the needed phase profile of the desired holograms can be reconstructed into a metasurface design.

antenna		1	2	3	4	5	6	7	8
length L [nm]	long	396	378	355	282	396	378	355	282
	short	293	239	187	156	293	239	187	156
angle θ [°]		60	90	120	180	60	90	120	180
β [°]		45	45	45	45	135	135	135	135

Table 3.1: Lengths for short and long antennas for antennas that generate different phase shifts. The numbers 1 - 8 correspond to the antennas and phases shown in Figure 3.5. The angle θ needs to be unchanged for short and long antennas, as this is given by the design of the metasurface.

The simulated metasurface is then fabricated with a two-step EBL process and lift-off technique. Each step is performed as described in chapter 2.5.1. In the first step the gold part of the antennas is fabricated and an additional marker system is written on the sample as well. With these markers the sample is aligned in the second step to perfectly place the Mg ends next to the gold antennas. To actually transform Mg to MgH_2 a catalyst is necessary [Ste15]. That is why a layer of 5 nm palladium (Pd) is evaporated onto the 50 nm thick Mg layer. To prevent those two materials from alloying 2 nm titanium (Ti) separates them. It also serves as 2 nm thick adhesion layer below the Mg (Figure 3.3 (b)).

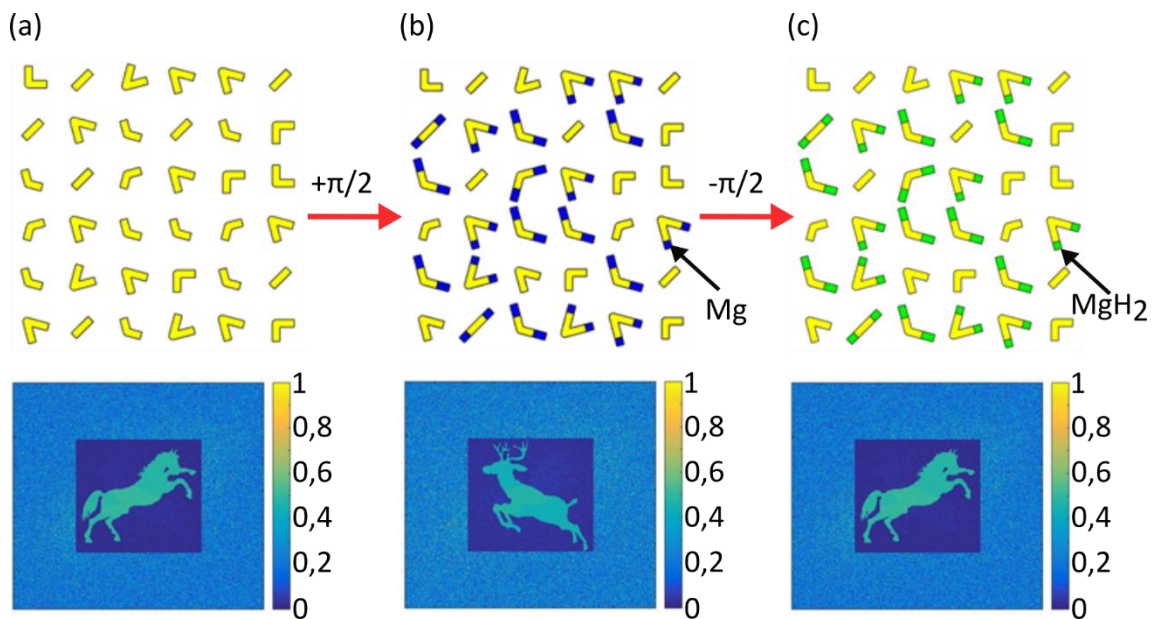


Figure 3.7: Functionality principle of metasurface. (a) pure gold short antennas generate a hologram that depicts a horse (b) additional Mg at the ends of the antenna adds a phase of $+\pi/2$ and the hologram image changes to a deer (c) Putting the metasurface in a hydrogen turns the Mg into MgH_2 with dielectric properties. Only the short gold part of the antenna behaves plasmonic and the hologram depicts a horse again.

Figure 3.7 shows the basic functionality principle of the metasurface. If only the short Au antennas are fabricated the generated hologram depicts a horse (Figure 3.7 (a)). By adding the additional Mg ends to the v-antennas the phases shift by $+\pi/2$ and a deer is visible in an air environment (Figure 3.5 (b)). If those antennas are now put into a hydrogen environment, the hydrogen diffuses into the Mg and forms MgH_2 that means only the short Au antennas are plasmonic and the hologram depicts a horse again.

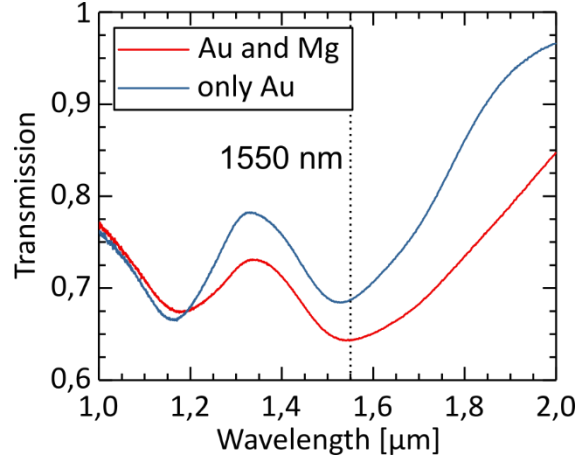


Figure 3.8: Transmission spectra of hologram metasurfaces, one consisting of hybrid antennas made of Mg and Au, the other only of pure Au antennas, both fabricated on a glass/ITO substrate.

First, the linear transmission spectrum of the antenna fields is taken; to make sure that the resonance wavelength is indeed at 1550 nm as it was designed to be. There is also an antenna field with pure Au antennas on the sample, to later have a comparison of the performance of the metasurface. This metasurfaces consist of the same (short) Au antennas as used for the hybrid antennas only without the Mg attachment. The transmission of both, the hybrid (Au and Mg) and the pure Au antennas can be seen in Figure 3.8. The resonance wavelength of the hybrid antennas is at 1550 nm and is only slightly redshifted compared to the gold antennas. As described before, the antennas are designed to have the same resonance wavelength independent of being made only of Au or of Au and Mg. This is now experimentally verified.

For the hologram measurement, the sample is put into a gas cell, as this enables the user to create a hydrogen atmosphere around the sample. This cell is placed on a three dimensional translation stage. The OPO is set to 1550 nm , since the antennas are resonant at this wavelength. A Glan-Taylor prism polarizes the laser beam linearly in horizontal (x -) direction and a lens with a focal length of $l = 300\text{ mm}$ focuses the light onto the metasurface (Figure 3.5). This lens is chosen as it produces a focal spot big enough to illuminate the complete metasurface, which is $200 \times 200\text{ }\mu\text{m}^2$ big. After the sample, there is a hinged mirror, which leads the beam to an imaging setup consisting of a lens and a CCD camera. That enables the user to align the laser beam spot on the metasurface by moving the sample via the translation stage. If the mirror is not in use, the scattered light passes a linear polarizer in vertical (y -) direction. The generated hologram is then displayed on a screen. As the hologram is generated in the NIR a camera with an InGaAs detector is used to capture it. First, the hologram is imaged with the sample in air, later the gas cell is filled with hydrogen and another snapshot of the hologram is taken.

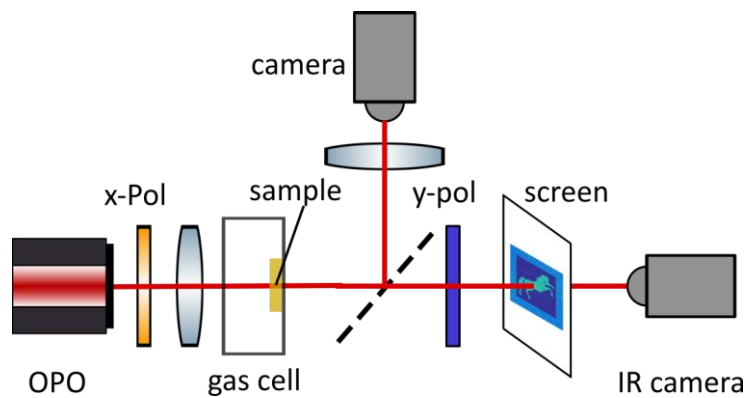


Figure 3.9: Hologram measurement setup. x -polarized light is focused onto the sample that resides in a gas cell. The scattered light then passes another linear polarizer, through which only y -polarized light can pass. On a screen behind the polarizer, the image occurs and is captured by an IR camera. An additional hinged mirror behind the sample enables an imaging setup to locate the laser beam spot on the sample.

As mentioned before, one metasurface only consist of the short Au antennas, which are supposed to generate the hologram of a horse. Figure 3.10 (a) shows the captured image. The horse is clearly visible. The bright spot in the middle is the unscattered fundamental beam, which should be filtered out by the cross polarization that is used (excitation with polarization in x -direction, detection of polarization with y -direction). However, the two linear filters probably do not work perfectly and some light still comes through. It is suppressed enough that it does not overshadow the hologram, and a detection is still possible.

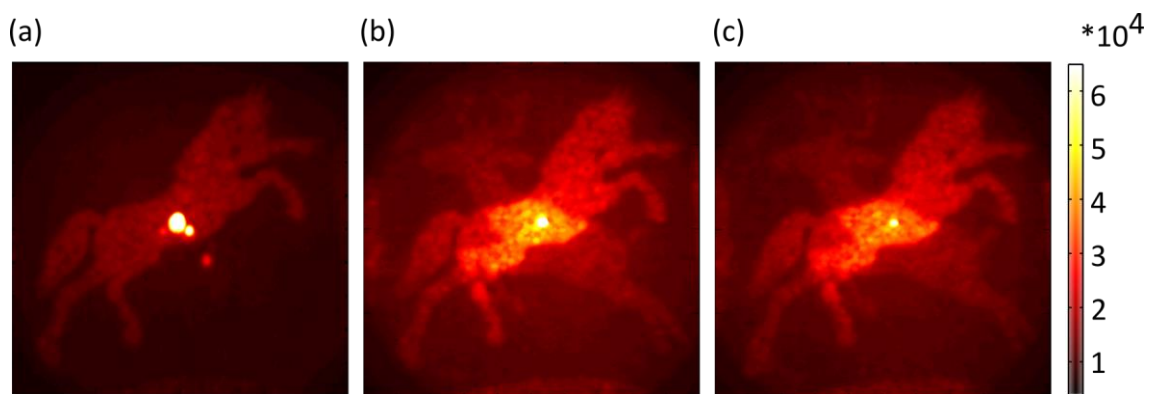


Figure 3.10: Images of holograms of two different metasurfaces (a) Metasurface only consisting of short gold antennas, which generate a hologram of a horse. (b) Active hologram of metasurface of hybrid antennas made of gold and magnesium in air. (c) Hologram after the hybrid metasurface of (b) resided 25 min in hydrogen.

Figure 3.10 (b) shows the captured image of the hologram generated by the metasurface consisting of hybrid Au and Mg antennas (as shown in Figure 3.3 (c)). The design is supposed to generate the hologram of a deer, while the sample resides in an air environment. Here, however, a deer and a horse are visible. Simulations show that this

can be caused by a gap between the Au and the Mg. This gap can cause the phase of the long antennas to be shorter than expected. Figure 3.11 shows the corresponding simulations. The first image on the top left shows the simulation for pure Au antennas, which depicts a horse and a phase of φ_0 . The last image on the bottom right shows the hologram of the perfectly working hybrid antennas depicting a deer with a phase of $\varphi'_0 = \varphi_0 + \frac{\pi}{2}$. If the phase shift is smaller than $\frac{\pi}{2}$, the horse becomes visible. The figure on the top right and bottom left show this behavior. The smaller the phase, the higher the intensity of the horse. Even a small gap of only 1 nm can cause these problems. Therefore, a gap between Au and Mg has to be avoided.

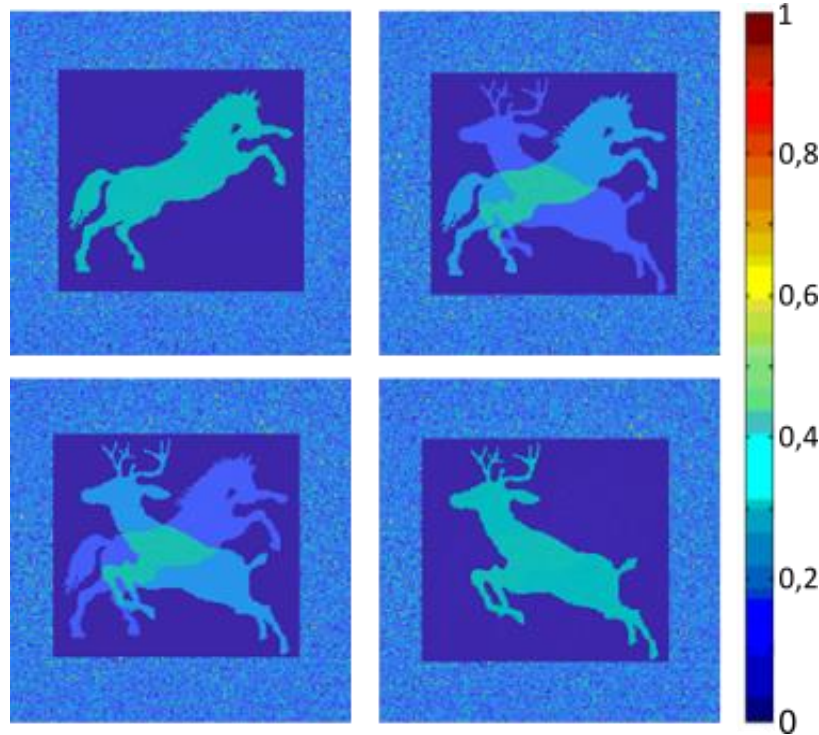


Figure 3.11: Simulation of generated hologram by a metasurface with hybrid antennas for different additional phases caused by improper alignment of the two parts of the hybrid antennas. From top right to bottom right the additional phase increases from $0,2 \cdot \pi$ to $0,5 \cdot \pi$. On the top left, the simulation with no additional phase is shown.

Despite not fulfilling the expectations completely, the metasurface is put into a hydrogen atmosphere, as the Mg still reacts to MgH_2 . Therefore, the deer in Figure 3.10 (b) should disappear, while the horse should become brighter. After the metasurface resided 25 min in the hydrogen environment the image of the hologram is taken again and is shown in Figure 3.10 (c). The deer is still visible, but it is less intense than before. The intensity decreases around 21%. This is especially visible in the overlap region, where the intensity is obviously decreased compared to the measurement in air atmosphere. As the deer does not disappear completely, that means that the reaction from Mg to MgH_2 does not work as wished. As the Ti layer between the Mg and the Pd layer is only 2 nm thick, it might be possible, that it is not a complete film. This can cause the Mg and Pd to form an

alloy, which would prevent the Mg to react with the hydrogen and, therefore, the antennas would still be the same as before, and hence create the same hologram. With 5 nm the Pd layer is also quite thin. As it serves as a catalyst for the reaction from Mg to MgH₂ it might be possible, that this layer also is too thin and the Mg only partly reacts to MgH₂. That is why the deer hologram does not disappear completely. Another sample with a thicker separating layer of Ti and a thicker catalyst layer of Pd might solve these problems.

All the images in Figure 3.10 show a circle around the hologram. This circle is caused by the polarizer's dimensions, as it stands very close to the imaging plane and therefore cuts off everything outside this circle.

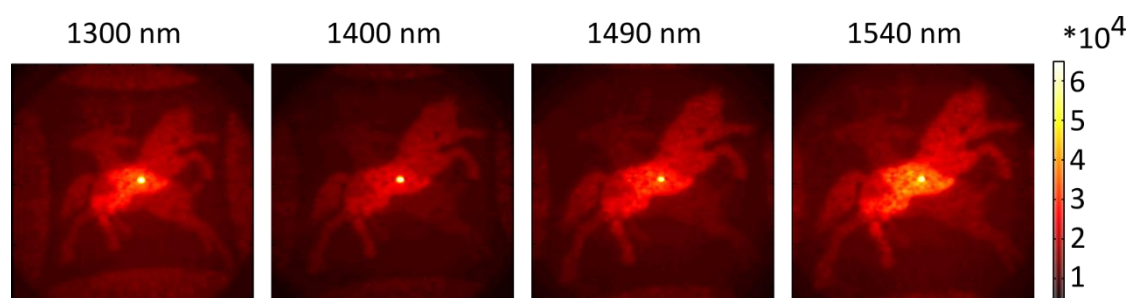


Figure 3.12: Images of the hologram taken for four different incident wavelength (1300, 1400, 1490 and 1540 nm). The metasurface works broadband, but due to the scattering properties and the resonance of the nanoantennas, the hologram appears in different sizes and intensities.

To characterize the metasurface further, the hologram is captured for different wavelengths. These images for incident wavelengths of 1300, 1400, 1490 and 1540 nm can be seen in Figure 3.12. For all wavelengths, both holograms are visible. Depending on the wavelength, the intensity and size varies, but this was to be expected. The intensity difference is caused by the detector sensibility and of course by the resonance wavelength of the nanoantennas. The closer the incident wavelength is to the resonance, the better is the performance of the metasurface. The resonance also causes the size difference. As the metasurface is designed for 1550 nm the hologram appears in the expected size. As the antennas scatter differently for other wavelength, the hologram can appear smaller, like one can see for 1300 nm. However, this wavelength scan shows that the metasurface can operate for a broadband wavelength range.

3.1.2 Discussion of results

To generate an active hologram a metasurface of hybrid nanoantennas made of Au and Mg is fabricated. As the Mg reacts to MgH₂ in a hydrogen atmosphere, the Mg part loses its plasmonic properties. This means that the metasurface can generate two different holograms. One while it resides in air, one while in hydrogen.

The produced metasurface in an air atmosphere however, generates both holograms, the horse and the deer, simultaneously. This is caused by a phase shift smaller than $\frac{\pi}{2}$, that is generated when the Mg and Au parts are not properly connected, that means, when there is a small gap. The smaller this phase is the more intense becomes the hologram that is not supposed to be generated, in our case the horse.

Still the deer should disappear in hydrogen. The experiment, however, still shows both images, but the deer's intensity is decreased compared to the measurement in air. This means that the Mg does not react completely to MgH_2 . This is probably caused by the layer of Pd, which is too thin and, therefore, does not fulfill its function as a catalyst. The Ti between Mg and Pd with a thickness of only 2 nm might not form a complete layer, which leads to the Mg and Pd to form an alloy. This might hinder the Mg to react to MgH_2 .

A new sample with new parameters of the layer thicknesses and a better alignment of the two antenna parts can fulfill the desired requirements and therefore produce an active hologram.

3.2 PANCHARATNAM-BERRY PHASE

Next to the phase manipulation via different resonances of optical scatterers, it is common to use the geometrical Pacharatnam-Berry (P-B) phase, which exists in the linear and nonlinear regime.

3.2.1 Linear P-B phase

In general, the P-B phase is a phase difference, which appears in the cycling of an adiabatic process and the system does not return to its initial state. During this process, the wave function gains an additional phase factor that leads to the phase difference. That means that such a phase can be obtained when two light beams propagate the same distance but their polarization state varies differently. This behavior was discovered by S. Pancharatnam in 1956 [Pan56]. To quantify the P-B phase one commonly uses the Poincaré sphere as within its frame work it is possible to describe the polarization states of light. Assuming a metasurface consisting of nano rods with different orientations, the P-B phase is laterally induced by different polarization variations caused by the orientation of the nanoantennas.

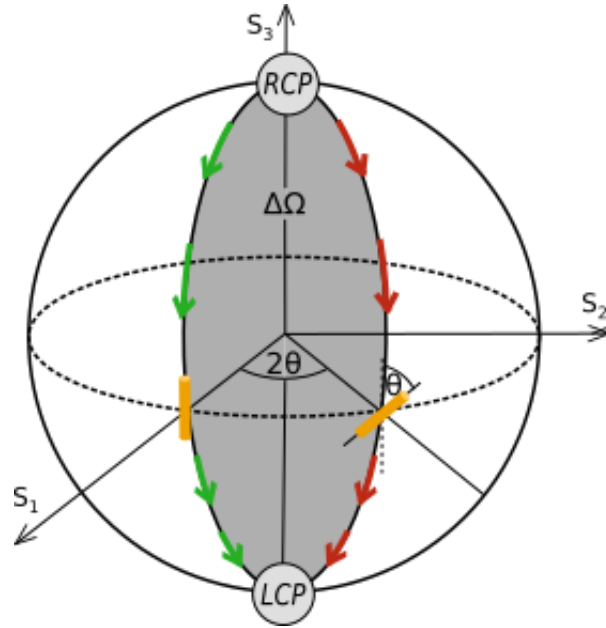


Figure 3.13: P-B phase depicted on a Poincaré sphere.

Figure 3.13 depicts right circular polarized (RCP) light shining on such a metasurface with two different antenna orientations. One of the antennas is tilted by an angle θ , whereas the other one is parallel to the x -axis (S_1). Using a linear polarizer and a quarter wave plate only left circularly polarized light (LCP) is measured. The green and red arrows depict two beam paths that have experienced different polarization changes, due to the different tilting angles of the nanorods. With the area encompassed by those two paths $\Delta\Omega$ the P-B phase φ_{PB} can be determined through [Bom02]

$$\varphi_{PB} = \frac{1}{2}\Delta\Omega \quad (3.7)$$

To explain the origin of this additional phase, we focus on the tilted nanorod by the angle θ with respect to the x -axis. This rod is illuminated with light with a general polarization state. For each polarization state, the light can be divided into RCP and LCP states. An electric field parallel to the nanorod leads to the highest scattering amplitude. Hence, the polarization of the light has to be rotated by an angle ϑ to generate a strong reaction of the tilted nanorod. To be parallel to the nanorod the RCP state therefore has to be rotated by θ . This means that the LCP state must rotate by $2\pi - \theta$. Hence, the difference of the two circular polarization states is 2θ . As the nanorods can be tilted by angles between 0 and π , one can achieve complete control over the full 2π range and the transmission amplitude remains steady [Lin14].

In the past few years many metasurface applications have been successfully demonstrated for the linear regime. Those metasurfaces, which consist of spatially variant meta-atoms, enable those before explained abrupt phase changes and can therefore manipulate the wavefront of transmitted or reflected light at the subwavelength scale. Various functional metasurfaces use this technique e. g. for anomalous refraction and reflection [Ni12], beam shaping [Che12, Li13, Ker15] and optical holography [Hua13].

3.2.2 Nonlinear P-B phase

The concept of the linear P-B phase has been successfully transferred to metasurfaces that operate in the nonlinear regime [Li15, Noo16, Tym15]. If a plasmonic (or dielectric), nanostructure is illuminated with an incident light beam with a circular polarization state σ the phase of the nonlinear light can be controlled by the orientation of the nano antenna. The generated electric field can be described by [Li15]

$$\vec{E}^\sigma = E_0(\hat{e}_x + i\sigma\hat{e}_y)/\sqrt{2} \quad (3.8)$$

with $\pm\sigma$ as right and left circular polarization states, respectively. The corresponding nonlinear dipole moment is given by

$$\vec{P}_0^{n\omega} = \alpha_\theta (\vec{E}^\sigma)^n \quad (3.9)$$

α_θ is the n 'th harmonic nonlinear polarizability tensor of the nanostructure with an orientation angle θ and ω is the angular frequency of the fundamental beam. We now introduce a second coordinate system next to the laboratory frame to analyze the dependence of the nonlinear dipole moment on the orientation angle of the nanostructure. In the local coordinate system of the nanostructure or local frame (see Figure 3.14) the local coordinate (x', y') axes are rotated by an angle θ . As described before the fundamental wave acquires a P-B phase [Li17]

$$\vec{E}_L^\sigma = \vec{E}^\sigma e^{i\sigma\theta} \quad (3.10)$$

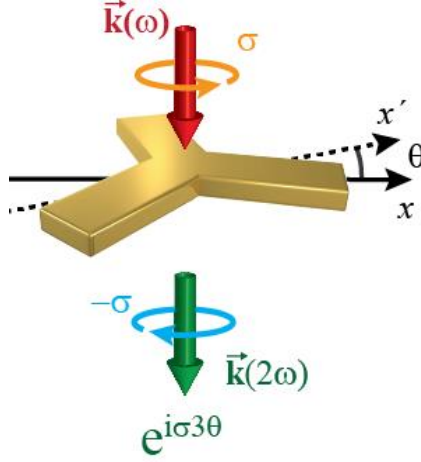


Figure 3.14: C3 antenna in local (x', y') and laboratory (x, y) frame that is illuminated with circular polarized light $(\vec{k}(\omega), \sigma)$ and generates SHG with the inverse circular polarization state $(\vec{k}(2\omega), -\sigma)$ [Li17].

The index L refers to the local frame of the nanostructure. In this frame the n 'th harmonic nonlinear polarizability is $\alpha_\theta = \alpha_\theta|_{\theta=0}$. Hence, the nonlinear dipole moment in this frame is

$$\vec{P}_{\theta,L}^{n\omega} = \alpha_0 (\vec{E}_L^\sigma)^n = \alpha_0 (\vec{E}^\sigma)^n e^{in\sigma\theta} \quad (3.11)$$

Using both circular polarization states σ and $-\sigma$ the nonlinear dipole moment can be separated into two dipoles that rotate in plane

$$\vec{P}_{\theta,L}^{n\omega} = \vec{P}_{\theta,L,\sigma}^{n\omega} + \vec{P}_{\theta,L,-\sigma}^{n\omega} \text{ with } \vec{P}_{\theta,L,\sigma}^{n\omega}, \vec{P}_{\theta,L,-\sigma}^{n\omega} \sim e^{in\sigma\theta} \quad (3.12)$$

In the laboratory frame the two rotating dipoles are therefore

$$\vec{P}_{\theta,\sigma}^{n\omega} = \vec{P}_{\theta,L,\sigma}^{n\omega} e^{-i\sigma\theta} \sim e^{i(n-1)\sigma\theta} \quad (3.13)$$

$$\vec{P}_{\theta,-\sigma}^{n\omega} = \vec{P}_{\theta,L,-\sigma}^{n\omega} e^{i\sigma\theta} \sim e^{i(n+1)\sigma\theta} \quad (3.14)$$

This leads to the expression of the nonlinear polarizabilities, which are given by

$$\alpha_{\theta,\sigma,\sigma}^{n\omega} \sim e^{i(n-1)\sigma\theta} \quad (3.15)$$

$$\alpha_{\theta,-\sigma,\sigma}^{n\omega} \sim e^{i(n+1)\sigma\theta} \quad (3.16)$$

Here, the nonlinear P-B phases $(n-1)\sigma\theta$ and $(n+1)\sigma\theta$ are introduced into the nonlinear polarizabilities of the n 'th harmonic generation with either the same or the

opposite circular polarization state in comparison to that of the incident beam. Due to selection rules, as described in chapter 2.5, only harmonic orders of $n = lm \pm 1$ are allowed (equation (2.65)) [Li15].

In the following we are working with three-folded rotation symmetric (C3) structures (as seen in Figure 3.14), hence, the concentration on their behavior. For SHG, the selection rule for C3 structures only works for $2 = 1 * 3 - 1$ (see Table 2.3). The " -1 " means that the polarization state of the SHG is opposite to that of the fundamental light. According to equation (3.16) the PB phase is then $3\sigma\theta$. In the following this phase is used to fabricate a nonlinear metasurface for optical image encoding.

3.2.3 Nonlinear optical image encoding

As the security of optical information gains more and more importance, nonlinear optical encryption, which uses nonlinear frequency conversion for decoding and encoding, is a new approach. In this chapter a nonlinear photonic metasurface that consist of C3 meta-atoms is introduced. This metasurface hides optical images under illumination with the fundamental wave but the image can be read out from the SHG waves [Wal17].

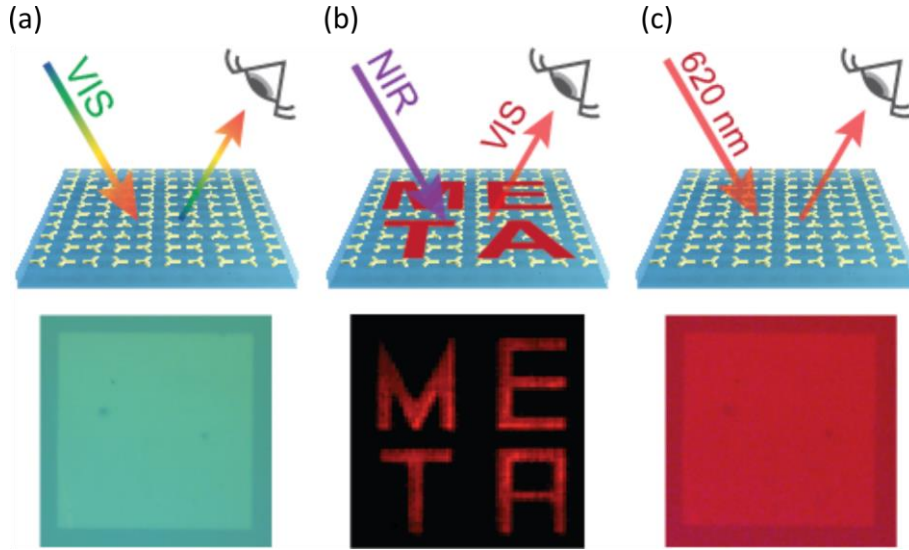


Figure 3.15: Working principle of the nonlinear metasurface under various illumination conditions
 (a) Under illumination with incoherent and unpolarized white light no image can be seen.
 (b) Using circularly polarized NIR light at 1240 nm to illuminate the metasurface, the encoded image with the characters "META" appear at the SHG wavelength 620 nm.
 (c) Illuminating the sample with light at the SHG wavelength of the NIR light at 620 nm, the encoded image cannot be read out anymore.

Figure 3.15 demonstrates the basic working principle of the metasurface. A real space image with the wording "META" is encoded into it. Under incoherent and unpolarized white light illumination in the visible spectral regime no image can be detected (a). Due to the higher reflectivity of the gold compared to the substrate, the metasurface appears slightly brighter (see Figure 3.15 (a) bottom). If illuminated with coherent near infrared

(NIR) laser light at a wavelength close to the resonance wavelength of the nano antennas, one can observe an image at the SHG wavelength with the opposite circular polarization. Hence, the encoded image can be read out in the visible regime (b). Under illumination with incoherent and unpolarized light at the SHG wavelength of the NIR light, again, no encoded image is observable (c). This confirms that the information is only encoded in the nonlinear optical process but not in the linear one.

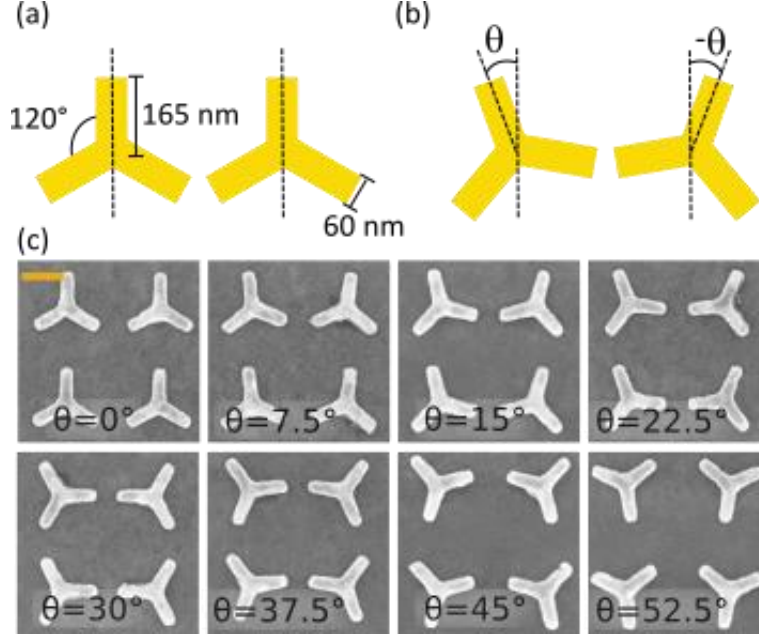


Figure 3.16: Design of the meta-atoms. (a) Schematic of the meta-atoms with a C3 symmetry. The metasurface is arranged periodically with a periode of 500 nm in x- and y-direction. The arms of the meta-atom ware 165 nm long, 60 nm wide and 30 nm. (b) The rotation angle θ of two neighboring meta-atoms (one virtual pixel) varies from 0° to 60° in steps of 7,5°. (c) SEM images of fabricated meta-atoms with various rotation angles (scale bar: 200 nm).

This idea of optical image encoding in the nonlinear process is experimentally verified with a metasurface consisting of C3 gold meta-atoms (see Figure 3.16 (a)). As mentioned before, only SHG with the reversed polarization ($-\sigma$) is generated for a wave propagating along the rotational axis of the antennas with circular polarized light (σ). Therefore, an additional P-B phase of $3\sigma\theta$ arises, with the in-plane orientation angle θ . By placing two meta-atoms into one unit cell, the SHG signals of both interfere in the far field. If they have different orientations, the intensity of the SHG becomes angle dependent. If both have the same orientation angle θ , the interference of the two SHG waves is constructive, which corresponds to the maximum of the SHG intensity. For all the other configurations with different orientation angles, the SHG intensity is reduced. This means, that by controlling the orientation of the meta-atoms on the metasurface, it is possible to gain spatially variant control over the SHG signal. As simplification, the two meta-atoms of a unit cell have orientation angles of θ and $-\theta$ relative to the virtual line in Figure 3.16 (b).

As already discussed the electrical field of the SHG is proportional to $(i\sigma 3\theta)$ and therefore the SHG from each unit cell is given by

$$I(\theta) \sim |\exp(i \cdot 3\theta) + \exp(-i \cdot 3\theta)|^2 \sim \cos^2(3\theta) \quad (3.17)$$

3.2.3.1 Experiment

Based on the above-described design, nine gold meta-atom arrays with an area size of $100 \times 100 \mu m^2$ are fabricated on an ITO/glass substrate via EBL and lift-off technique as described in chapter 2.5.1. The orientation angle θ of the meta-atoms in each array varies from 0° to 60° in steps of $7,5^\circ$. Figure 3.5 (c) shows scanning electron microscopy images of all the different angles except 60° as this equals 0° . The meta-atoms are designed to be resonant in the NIR regime. The arm length, arm width and height of the antennas are 165, 60, and 30 nm, respectively. Both in x - and y -direction the period is 500 nm.

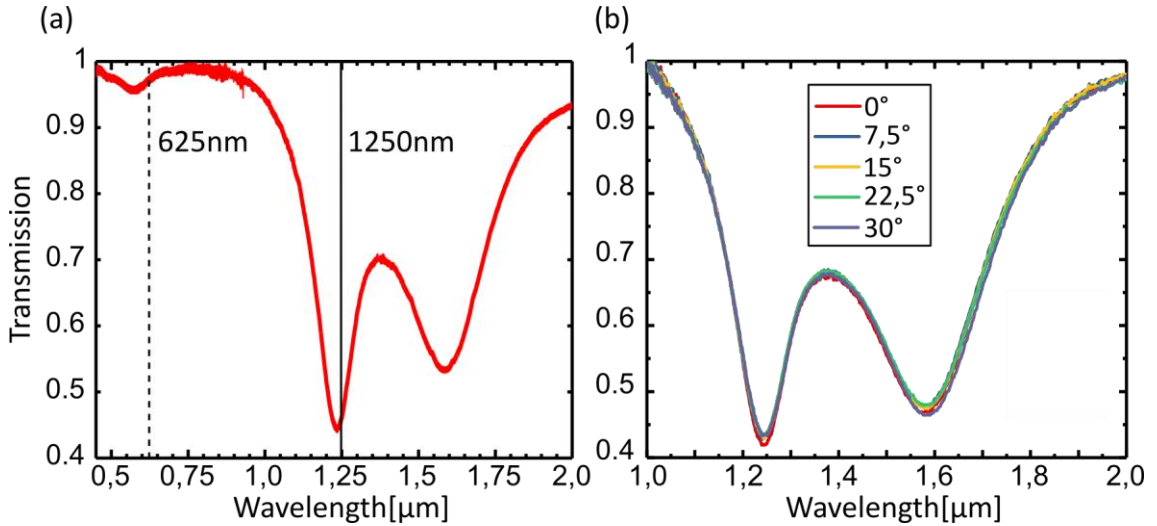


Figure 3.17: Linear optical properties of the metasurfaces. (a) Measured transmission spectrum of metasurface made of C3 meta-atoms with unpolarized light. The dip at a wavelength of 1240 nm corresponds to the localized plasmon resonance of the meta-atoms. The marked lines show the spectral position of the used fundamental laser wavelength and the corresponding SHG. (b) Measured transmission of metasurfaces with varying orientation angles of the meta-atoms from 0° to 30° .

In the regime between 1000 and 2000 nm the linear transmission of the metasurfaces is characterized with FTIR as described in chapter 2.5.2. In the range from 450 to 1000 nm the characterization is performed using a home-built white light transmission setup. The pronounced dip in Figure 3.17 (a) at 1240 nm results from the plasmonic resonance of the C3 meta-atoms. At the SHG wavelength of 617 nm no resonance appears. Figure 3.17 (b) displays the FTIR measurements of fields with different orientation angles θ from 0° to 30° . For each angle the transmission is equally strong due to the meta-atoms' isotropic linear optical properties caused by their C3 symmetry. That means that neither the phase nor the scattering of the fundamental wave depends on the orientation angle. For the

encoding of the image only in the SHG signal the meta-atoms need a C3 rotational symmetry. This symmetry group generates an isotropic linear response with no additional P-B phase to the scattered light field. However, for circular polarized light C3 structures generate SHG and this SHG signal contains a nonlinear P-B phase due to the rotation angle. Therefore, it is possible to encode an image in the orientation of the C3 structures without influencing the linear scattering properties.

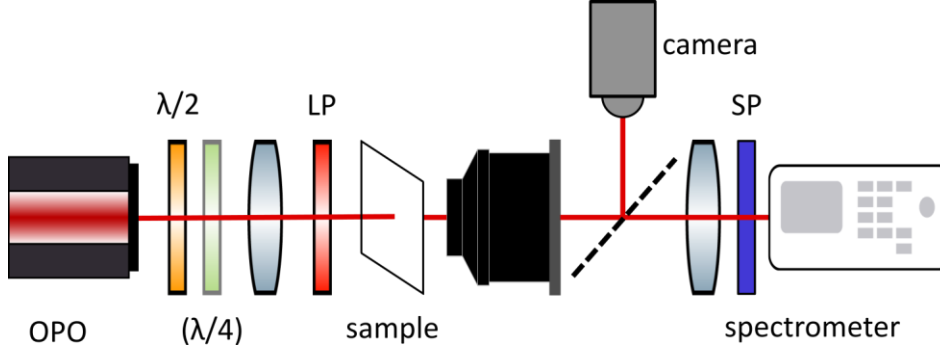


Figure 3.18: Setup for SHG transmission measurement. After passing a half-wave plate and if circularly polarized light is needed a quarter wave plate, the light is focused onto the sample. To eliminate possible generated harmonic signals of optical components in front of the sample a long pass filter is placed after the focusing lens. An objective collects the light after the sample, which passes a short pass filter and is then coupled into a spectrometer. A hinged mirror behind the objective and a CCD camera form an imaging system to locate the laser spot on the sample.

To experimentally verify the capability of controlling the intensity of the generated SHG signal from nine different meta-surfaces with varying orientation angles the sample is illuminated with circular polarized light. As the resonance frequency lies in the infrared regime, again the Ti:sapphire laser pumped OPO (chapter 2.2.2) is used and set to 1250 nm . The laser beam first passes a linear polarizer (Pol) and then a quarter wave plate ($\lambda/4$) (see Figure 3.18) which generates either left or right circularly polarized light depending on the angle in reference to the linear polarizer. After that, a lens with a focus length of $f = 100 \text{ mm}$ focuses the light onto the metasurface. A long pass filter (LP) (cut off wavelength $\lambda = 1000 \text{ nm}$) filters out all possible generated nonlinear signals by other optical components than the metasurface. The SHG from the metasurface is then collected in transmission direction by a 20x microscope objective and after passing a circular polarization analyzer ($\lambda/4$ and Pol) the SHG is focused onto a EMCCD detector (spectrometer) that analyzes the SHG wave. To get rid of other signals, the light is passing a short pass filter (SP) (cut of wavelength $\lambda = 730 \text{ nm}$) as well in front of the spectrometer. A hinged mirror enables the user to check the laser position on the sample with a CCD camera.

The SHG intensity from the virtual pixels of nine different metasurfaces with varying orientation angles θ from 0° to 60° is then characterized at a wavelength of 1250 nm . Figure 3.19 (a) shows the expected SHG intensity function $\cos^2(3\theta)$ next to the

experimentally found results. The experiment follows the theory exactly. For $\theta = 0^\circ$ or 60° the SHG intensity reaches a maximum, whereas for $\theta = 30^\circ$ it reaches its minimal value. As described in chapter 2.5 the selection rule for SHG generated by C3 meta-atoms only allows SHG signals with circular polarization opposite to that of the fundamental wave ($L \rightarrow R$ and $R \rightarrow L$). The SHG with the same polarization state as the fundamental one ($L \rightarrow L$ and $R \rightarrow R$) is forbidden. The experimental results shown in Figure 3.19 (a) verify this selection rule. Only the converted polarization shows a pronounced SHG signal. As each linear polarization state can be described as a superposition of right and left circular polarized light, the SHG intensity follows the same function of $\cos^2(3\theta)$. Under illumination with any linearly polarized light, the SHG intensity of the metasurface therefore follows the same curve (Figure 3.19 (b)). Hence, the polarization of the fundamental wave does not influence the nonlinear encoding.

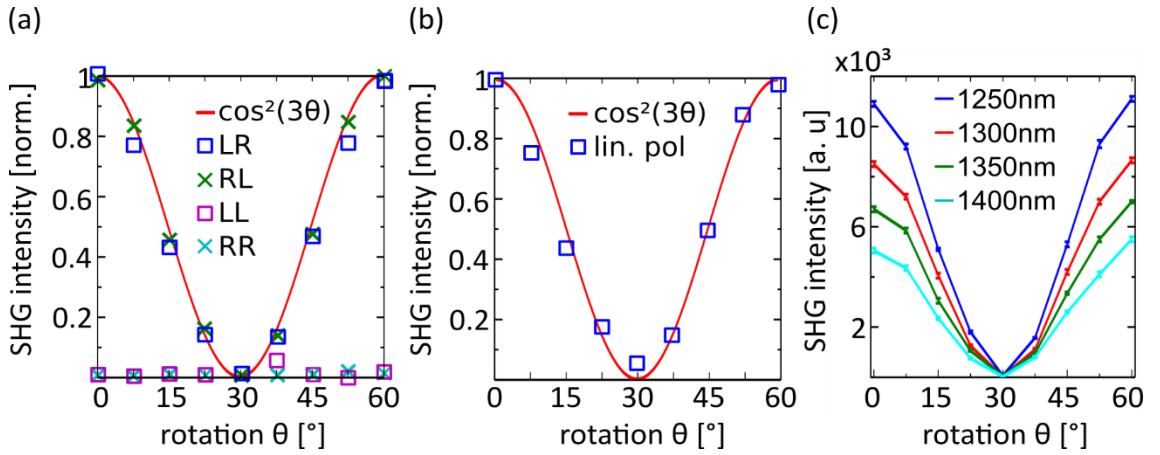


Figure 3.19: SHG intensities of the metasurfaces. (a) Angle dependent SHG measurement for excitation with a fundamental wavelength of 1250 nm for various circular polarization schemes. In the legend the first letter describes the polarization state of the fundamental wave and the second letter the one for the SHG signal. (L, left circular polarization; R, right circular polarization). The red line shows the expected behavior of the SHG intensity, due to interference effects. (b) Angle dependent SHG intensity for linear polarized light with a fundamental wavelength of 1250 nm and the expected behavior (red line) (c) Measured angle dependent right circular polarized SHG intensity for a left circular polarized fundamental wave at four different wavelengths from 1250 to 1400 nm.

This orientation angle dependent measurement is repeated for different fundamental wavelengths from 1250 to 1400 nm in steps of 50 nm. As a simplification only the measurements for left circular polarized excitation and right circular polarized SHG are performed. Figure 3.19 (c) shows that the orientation angle dependent SHG intensity modulation is independent of the excitation wavelength. That means it shows a dispersionless behavior for all wavelengths. As it is closest to the plasmonic resonance wavelength of the meta-atoms, the excitation at a wavelength of 1250 nm shows the highest intensity. Increasing the fundamental wavelength from 1250 to 1400 nm,

decreases the SHG intensity continuously. Still the minimal value of the SHG signal is obtained for an orientation angle of $\theta = 30^\circ$.

As the measurements show, it is possible to precisely control the SHG intensity for homogenous and periodically arranged meta-atom pairs. This concept is now applied to encode the letters “META” into a metasurface. Each character consists of C3 meta-atom pairs with an orientation angle $\theta = 0^\circ$ and the background with $\theta = 30^\circ$ respectively. Figure 3.20 (a) shows the schematic of the $100 \times 100 \mu\text{m}^2$ metasurface. Under illumination with circular polarized fundamental light in the NIR regime, the background (red, $\theta = 30^\circ$) is supposed to generate no SHG signal and therefore appears dark whereas the letters (blue, $\theta = 0^\circ$) are supposed to show a bright SHG emission. In this way, the encoded characters “META” become visible through the SHG process from the meta-atoms. However, the letters remain hidden if no SHG process is utilized.

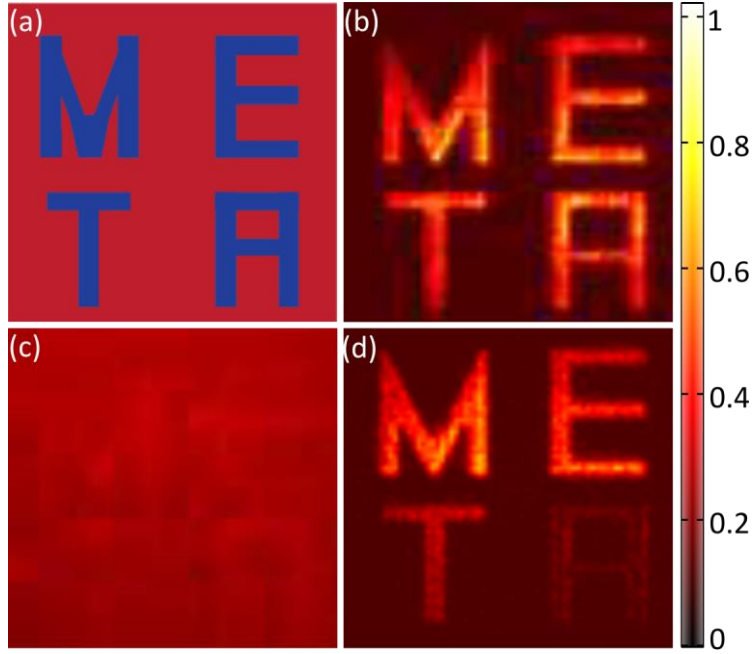


Figure 3.20: Schematic and real space images of the metasurface. (a) Spatial map of the orientation angle θ of the meta-atom pairs. The color red corresponds to an angle $\theta = 30^\circ$ between the two C3 structures, whereas blue indicates $\theta = 0^\circ$. (b) Experimentally measured image at the SHG wavelength for an excitation at the resonance wavelength of 1250 nm, showing the characters “META” (c) obtained image at the fundamental pump wavelength (1250 nm), showing no characters. (d) Image at the SHG wavelength each letter consists of meta-atom pairs with a different orientation angle $\theta = 0^\circ; 7,5^\circ; 15^\circ; 22,5^\circ$ respectively, which leads to an intensity modulation.

For the measurements, the spectrometer in the setup in Figure 3.18 is changed with a CCD camera. Figure 3.20 (b) shows the experimentally measured SHG image with bright “META” letters on a dark background for a fundamental wavelength of 1250 nm. If the short pass filter in front of the detector is changed with a long pass filter (cutoff wavelength $\lambda = 1000 \text{ nm}$) only the fundamental light is detected. As explained before,

the light scattering in the linear regime is unaffected by the orientation angel, that is why the encoded letters “META” disappear in the nearly homogeneous background (Figure 3.20 (c)).

As a demonstration of the potential of this approach to tailor the SHG intensity in an encoded image continuously, another sample is fabricated, in which each character of the word “META” consist of meta-atom pairs with different orientation angles, which leads to different brightnesses. The letter “M” is the brightest letter and therefor the orientation angle is $\theta = 0^\circ$, whereas the letter “A” has the lowest SHG intensity and therefore corresponds to $\theta = 22,5^\circ$. As the background is still supposed to generate no SHG signal and appear dark, the corresponding orientation angle is $\theta = 30^\circ$. Figure 3.20 (d) depicts the measured SHG image. The Gaussian intensity profile of the beam causes the SHG intensity of the letters to appear brighter towards the center of the image in Figure 3.20 (b) as well as in (d). However, a clear SHG intensity change of the four letters is visible.

Using the same concept of tailored SHG intensities one can simply invert the SHG images of Figure 3.20 (b) and (d). Therefore, the orientation angle of the background is set to $\theta = 0^\circ$ and the one for the letters is $\theta = 30^\circ$. This leads to the negative version of Figure 3.20 (b) shown in Figure 3.21 (a). Here the letters appear dark on a bright background. By using different orientation angles for each letter a similar inverted result is obtained for the SHG image of Figure 3.20 (d), here shown in Figure 3.21 (b).

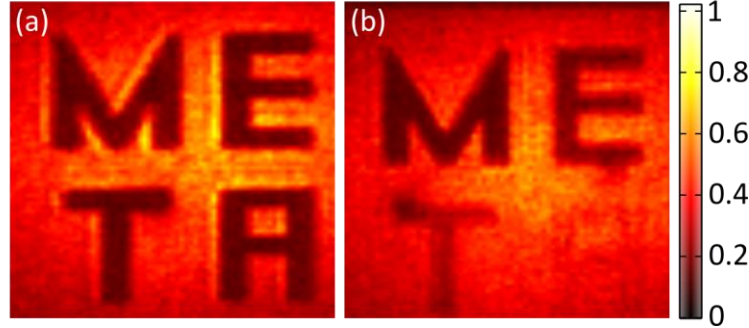


Figure 3.21: Inverted real space SHG images (a) Measured real space SHG image for the inverse design of Figure 4a. Now $\theta=0^\circ$ is used for the background and the character is made with $\theta=30^\circ$. (b) Measured real space SHG image for the inverse design of Figure 4a.

3.2.3.2 Discussion of results

A possibility to encode information of an optical image into a nonlinear metasurface is to use the concept of local interference of two neighboring C3 gold antennas. By varying the orientation of those antennas, they exhibit different geometric Pancharatnam-Berry phases for the SHG wave. With this technique, the interference and therefore the intensity of the SHG signal can be tailored.

Using these antennas it is possible to give each pixel, which consist of two neighboring C3 antennas a different intensity. Therefore, it is possible to create a gray scale image, which

can only be read out through the SHG signal and is not observable for the fundamental wavelength.

Combining this metasurface with highly nonlinear materials such as semiconductor multi quantum wells, the SHG efficiency can be drastically enhanced [Lee14]. Therefore, the real space encoding with nonlinear metasurfaces opens possibilities for information encryption, nonlinear imaging and information security.

4 CONCLUSION

Metasurfaces made of plasmonic nanoantennas provide a great variety of possible applications. They can operate in the linear as well as in the nonlinear regime, and therefore can combine plasmonics with nonlinear optics. This work analyzes different metasurfaces for a selection of applications. Some, which make use of the enhancement of the electric near field, as well as others that generate nonlinear signals themselves. Furthermore, metasurfaces that use the ability to generate phase changes of the incoming light are investigated.

The property of plasmonic nanoantennas to enhance their electric near field can be used to increase the nonlinear signal intensity in nonlinear media. To use a PIN diode as an infrared detector they are placed on top of it, as the PIN diode generates a current under illumination with light in the visible range, in our case at around 950 nm . Unfortunately, the diode produced high currents under illumination of areas that are not even part of the connected diode. This makes it difficult to analyze the measured data, as the generated current is strongly dependent on the area that is illuminated.

If the nanoantennas, however, are placed on a thin ZnO substrate, which is already highly nonlinear, the generated SHG signal can be drastically enhanced. Without nanoantennas, the substrate hardly generates any nonlinear signal under perpendicular illumination. Nanoantennas can change this, as they produce an electrical near field with components in all directions. This can be even improved by using double resonant nanoantennas that consist of one long antenna, which is resonant at the fundamental wavelength and one short antenna that is resonant at the SHG wavelength. This design enables a better decoupling of the SHG signal into the electric far field. This leads to an enhanced nonlinear signal, which is two times stronger compared to single resonant antennas.

Plasmonic nanoantennas cannot only enhance nonlinear signal generated by other materials, but furthermore, they can also generate it themselves. Under illumination with circularly polarized light, the order of this nonlinear signal depends on the rotational symmetry of the nanoantennas. This behavior can be described by selection rules, which say that e.g. for a fourth harmonic signal antennas with a five fold (C_5) symmetry are necessary. Not only the antenna symmetry, but also the symmetry of the antenna arrangement can influence the nonlinear generation. The produced sample with C_5 nanoantennas arranged either quadratically or in a Penrose lattice like symmetry, however, does not produce any measurable fourth harmonic signal. With increasing order, the nonlinear signal becomes weaker as more photons are needed. However, the antennas are made of noble metals in this case silver, to avoid the interband transitions of gold, and they tend to melt at high exciting powers. That means the laser power that can be applied without melting the antennas, is not high enough to generate a fourth harmonic signal. One solution is to use a laser with shorter pulses (shorter than 200 fs), with which the unproblematic exciting power is increased.

To use plasmonic structures as metasurfaces, an important part is not only to enhance other signals, but also to be able to modulate the phase, as this is what many optical components do. This work demonstrates that this can be via optical scatters that cause phase discontinuities at interfaces between two materials. Another approach is the geometric Pancharatnam-Berry phase. For that, the antennas are rotated and generate a local phase while illuminated with circularly polarized light. This technique works in the linear as well as in the nonlinear regime.

A locally adjustable phase enables the fabrication of metasurfaces that can generate holograms. In this work, it is demonstrated that it is possible to generate so called active holograms. This means that the metasurface generates a different hologram depending on the surrounding atmosphere. The nanoantennas of the metasurface consist of gold and magnesium, and the magnesium reacts to MgH_2 in a hydrogen environment. Other than magnesium, MgH_2 does not have plasmonic properties and therefore the generated local phases of the antennas change. With the right antenna arrangement, it is now possible to generate the hologram of a horse when the metasurface resides in air and the hologram of a deer, when residing in hydrogen. As the arrangement of gold and magnesium of the shown sample is not perfect, the hybrid antennas generate both holograms as this imperfect arrangement does not produce the correct phase but a smaller one. The magnesium needs palladium as a catalyst to react to MgH_2 and as this layer is too thin, the hydrogenation process is not complete and the hologram of the deer does not disappear completely. However, it is shown that the generated hologram does change with changing atmosphere.

If the nanoantennas already generate a nonlinear signal, for example C3 structures that generate SHG, the local phase of this signal can be controlled as well, via the nonlinear Pancharatnam-Berry phase. In this work it is demonstrated, how two nanoantennas or meta-atoms that form one pixel, can control the intensity of the SHG signal locally. As the generated geometric phase is angle dependent, the antennas are rotated and the SHG signal of the two meta-atoms interfere. By controlling the phase of both, it is possible to control the intensity of the interference. This technique offers a simple way to encode optical information into metasurfaces, by designing a gray-scale image based on the rotation angle of the meta-atoms. Combining this metasurface with highly nonlinear materials, for example ZnO or multiple quantum wells, as here the SHG is greatly enhanced, opens new application for optical image security and nonlinear imaging.

Over all this work shows many various application possibilities based on the various properties of plasmonic nanoantennas. Still some of them need further investigation or improvement of the design, but others already show their great potential. However, further combination with nonlinear materials as substrates could even improve these. It is obvious that metasurfaces made of plasmonic nanoantennas build a good foundation for various future optical components. The enhancement of nonlinear signals and the possibility of controlling phase and intensity offer many interesting applications.

5 REFERENCES

- [Alm16] Almeida, E.; Bitton, O.; Prior, Y.: Nonlinear metamaterials for holography. In Nat. Commun. (Nature Communications), 2016, 7; S. 12533.
- [Alo98] Alon, O. E.; Averbukh, V.; Moiseyev, N.: Selection Rules for the High Harmonic Generation Spectra. In Physical Review Letters, 1998, 80; S. 3743–3746.
- [Bal09] Baldi, A.; Gonzalez-Silveira, M.; Palmisano, V.; Dam, B.; Griessen, R.: Destabilization of the Mg-H system through elastic constraints. In Physical review letters, 2009, 102; S. 226102.
- [Bar03] Barnes, W. L.; Dereux, A.; Ebbesen, T. W.: Surface plasmon subwavelength optics. In Nature, 2003, 424; S. 824–830.
- [Ber84] Berry, M. V.: Quantal Phase Factors Accompanying Adiabatic Changes. In Proceedings of the Royal Society A: Mathematical, Physical and Engineering Sciences, 1984, 392; S. 45–57.
- [Bha72] Bhagavantam, S.; SC, F. A.; Chandrasekhar, P.: HARMONIC GENERATION AND SELECTION. In Proc. Indian Acad. Sci. A, 1972; S. 13–20.
- [Blo99] Bloembergen, N.: Surface nonlinear optics. A historical overview. In Applied Physics B: Lasers and Optics, 1999, 68; S. 289–293.
- [Bom02] Bomzon, Z.; Biener, G.; Kleiner, V.; Hasman, E.: Space-variant Pancharatnam–Berry phase optical elements with computer-generated subwavelength gratings. In Optics Letters, 2002, 27; S. 1141.
- [Boy08] Boyd, R. W.: Nonlinear optics. Elsevier/Academic Press, Amsterdam, 2008.
- [Cel15] Celebrano, M.; Wu, X.; Baselli, M.; Großmann, S.; Biagioni, P.; Locatelli, A.; Angelis, C. de; Cerullo, G.; Osellame, R.; Hecht, B.; Duò, L.; Ciccacci, F.; Finazzi, M.: Mode matching in multiresonant plasmonic nanoantennas for enhanced second harmonic generation. In Nature nanotechnology, 2015, 10; S. 412–417.
- [Che12] Chen, X.; Huang, L.; Mühlenbernd, H.; Li, G.; Bai, B.; Tan, Q.; Jin, G.; Qiu, C.-W.; Zhang, S.; Zentgraf, T.: Dual-polarity plasmonic metalens for visible light. In Nature communications, 2012, 3; S. 1198.
- [Che14a] Chen, W. T.; Yang, K.-Y.; Wang, C.-M.; Huang, Y.-W.; Sun, G.; Chiang, I.-D.; Liao, C. Y.; Hsu, W.-L.; Lin, H. T.; Sun, S.; Zhou, L.; Liu, A. Q.; Tsai, D. P.: High-efficiency broadband meta-hologram with polarization-controlled dual images. In Nano letters, 2014, 14; S. 225–230.
- [Che14b] Chen, S.; Li, G.; Zeuner, F.; Wong, W. H.; Pun, E. Y. B.; Zentgraf, T.; Cheah, K. W.; Zhang, S.: Symmetry-selective third-harmonic generation from plasmonic metacrystals. In Physical review letters, 2014, 113; S. 33901.
- [Dre62] Dresselhaus, M. S.; Dresselhaus, G.: Interband Transitions for Metals in a Magnetic Field. In Physical Review, 1962, 125; S. 499–508.
- [Dru00] Drude, P.: Zur Elektronentheorie der Metalle. In Annalen der Physik, 1900, 306; S. 566–613.

-
- [Fet08] Feth, N.; Linden, S.; Klein, M. W.; Decker, M.; Niesler, F. B.; Zeng, Y.; Hoyer, W.; Liu, J.; Koch, S. W.; Moloney, J. V.: Second-harmonic generation from complementary split-ring resonators. In *Optics letters*, 2008, 33; S. 1975–1977.
 - [Fra61] Franken, P. A.; Hill, A. E.; Peters, C. W.; Weinreich, G.: Generation of Optical Harmonics. In *Physical Review Letters*, 1961, 7; S. 118–119.
 - [Hae05] Haes, A. J.; Haynes, C. L.; McFarland, A. D.; Schatz, G. C.; van Duyne, R. P.; Zou, S.: Plasmonic materials for surface-enhanced sensing and spectroscopy. In *MRS bulletin*, 2005, 30; S. 368–375.
 - [Har12] Harutyunyan, H.; Volpe, G.; Quidant, R.; Novotny, L.: Enhancing the nonlinear optical response using multifrequency gold-nanowire antennas. In *Physical review letters*, 2012, 108; S. 217403.
 - [Höv93] Hövel, H.; Fritz, S.; Hilger, A.; Kreibig, U.; Vollmer, M.: Width of cluster plasmon resonances: bulk dielectric functions and chemical interface damping. In *Physical Review B*, 1993, 48; S. 18178.
 - [Hua13] Huang, L.; Chen, X.; Mühlenbernd, H.; Zhang, H.; Chen, S.; Bai, B.; Tan, Q.; Jin, G.; Cheah, K.-W.; Qiu, C.-W.; Li, J.; Zentgraf, T.; Zhang, S.: Three-dimensional optical holography using a plasmonic metasurface. In *Nature Communications*, 2013, 4; S. 759323.
 - [Jac83] Jach, T.; Cowan, P. L.: PIN diodes as detectors in the energy region 500 eV–10 keV. In *Nuclear Instruments and Methods in Physics Research*, 1983, 208; S. 423–425.
 - [Jac99] Jackson, J. D.: *Classical electrodynamics*. Wiley, New York NY u.a., 1999.
 - [Joh72] Johnson, P. B.; Christy, R. W.: Optical Constants of the Noble Metals. In *Physical Review B*, 1972, 6; S. 4370–4379.
 - [Kau12] Kauranen, M.; Zayats, A. V.: Nonlinear plasmonics. In *Nature Photonics*, 2012, 6; S. 737–748.
 - [Ker12] Kern, J.; Grossmann, S.; Tarakina, N. V.; Häckel, T.; Emmerling, M.; Kamp, M.; Huang, J.-S.; Biagioni, P.; Prangsma, J. C.; Hecht, B.: Atomic-scale confinement of resonant optical fields. In *Nano letters*, 2012, 12; S. 5504–5509.
 - [Ker15] Keren-Zur, S.; Avayu, O.; Michaeli, L.; Ellenbogen, T.: Nonlinear Beam Shaping with Plasmonic Metasurfaces. In *ACS Photonics*, 2015, 3; S. 117–123.
 - [Kle06] Klein, M. W.; Enkrich, C.; Wegener, M.; Linden, S.: Second-harmonic generation from magnetic metamaterials. In *Science*, 2006, 313; S. 502–504.
 - [Ko11] Ko, K. D.; Kumar, A.; Fung, K. H.; Ambekar, R.; Liu, G. L.; Fang, N. X.; Toussaint, K. C.: Nonlinear optical response from arrays of Au bowtie nanoantennas. In *Nano letters*, 2011, 11; S. 61–65.
 - [Lam97] Lambrecht, B.; Leitner, A.; Aussenegg, F. R.: Femtosecond decay-time measurement of electron-plasma oscillation in nanolithographically designed silver particles. In *Applied Physics B: Lasers and Optics*, 1997, 64; S. 269–272.
 - [Lar12] Larouche, S.; Tsai, Y.-J.; Tyler, T.; Jokerst, N. M.; Smith, D. R.: Infrared metamaterial phase holograms. In *Nature materials*, 2012, 11; S. 450–454.

-
- [Lee14] Lee, J.; Tymchenko, M.; Argyropoulos, C.; Chen, P.-Y.; Lu, F.; Demmerle, F.; Boehm, G.; Amann, M.-C.; Alù, A.; Belkin, M. A.: Giant nonlinear response from plasmonic metasurfaces coupled to intersubband transitions. In *Nature*, 2014, 511; S. 65–69.
 - [Li13] Li, G.; Kang, M.; Chen, S.; Zhang, S.; Pun, E. Y.-B.; Cheah, K. W.; Li, J.: Spin-enabled plasmonic metasurfaces for manipulating orbital angular momentum of light. In *Nano letters*, 2013, 13; S. 4148–4151.
 - [Li15] Li, G.; Chen, S.; Pholchai, N.; Reineke, B.; Wong, P. W. H.; Pun, E. Y. B.; Cheah, K. W.; Zentgraf, T.; Zhang, S.: Continuous control of the nonlinearity phase for harmonic generations. In *Nature materials*, 2015, 14; S. 607–612.
 - [Li17] Li, G.; Zhang, S.; Zentgraf, T.: Nonlinear photonic metasurfaces. In *Nature Reviews Materials*, 2017, 2; S. 17010.
 - [Lin12] Linden, S.; Niesler, F. B.; Förstner, J.; Grynko, Y.; Meier, T.; Wegener, M.: Collective effects in second-harmonic generation from split-ring-resonator arrays. In *Physical review letters*, 2012, 109; S. 15502.
 - [Lin14] Lin, D.; Fan, P.; Hasman, E.; Brongersma, M. L.: Dielectric gradient metasurface optical elements. In *Science (New York, N.Y.)*, 2014, 345; S. 298–302.
 - [Lin16] Linnenbank, H.; Grynko, Y.; Förstner, J.; Linden, S.: Second harmonic generation spectroscopy on hybrid plasmonic/dielectric nanoantennas. In *Light: Science & Applications*, 2016, 5; e16013-e16013.
 - [Liu09] Liu, R.; Ji, C.; Mock, J. J.; Chin, J. Y.; Cui, T. J.; Smith, D. R.: Broadband ground-plane cloak. In *Science (New York, N.Y.)*, 2009, 323; S. 366–369.
 - [Mai07] Maier, S. A.: *Plasmonics. Fundamentals and applications*. Springer, New York, NY, 2007.
 - [Mar10] Marder, M. P.: *Condensed matter physics*. Wiley & Sons, Hoboken NY, 2010.
 - [Mat04] Matoba, O.; Javidi, B.: Secure holographic memory by double-random polarization encryption. In *Appl. Opt.*, 2004, 43; S. 2915–2919.
 - [McM06] McMahon, M. D.; Lopez, R.; Haglund, R. F.; Ray, E. A.; Bunton, P. H.: Second-harmonic generation from arrays of symmetric gold nanoparticles. In *Physical Review B*, 2006, 73; S. 3030.
 - [Mie08] Mie, G.: Beiträge zur Optik trüber Medien, speziell kolloidaler Metallösungen. In *Annalen der physik*, 1908, 330; S. 377–445.
 - [Mol87] Mollenauer, L.F.; White, J.C.; Cheng, K. Hrsg.: *Tunable lasers*. Springer, Berlin, 1987.
 - [Moo69] Mooradian, A.: Photoluminescence of Metals. In *Physical Review Letters*, 1969, 22; S. 185–187.
 - [Neu85] Neumann, F.E. Hrsg.: *Vorlesungen über die Theorie der Elasticität der festen Körper und des Lichtäthers: gehalten an der Universität Königsberg*. Teubner, Leipzig, 1885.
 - [Ni12] Ni, X.; Emani, N. K.; Kildishev, A. V.; Boltasseva, A.; Shalaev, V. M.: Broadband light bending with plasmonic nanoantennas. In *Science (New York, N.Y.)*, 2012, 335; S. 427.
 - [Noo16] Nookala, N.; Lee, J.; Tymchenko, M.; Sebastian Gomez-Diaz, J.; Demmerle, F.; Boehm, G.; Lai, K.; Shvets, G.; Amann, M.-C.; Alu, A.; Belkin, M.: Ultrathin gradient nonlinear metasurface with a giant nonlinear response. In *Optica*, 2016, 3; S. 283.

-
- [Nov07] Novotny, L.: Effective wavelength scaling for optical antennas. In *Physical review letters*, 2007, 98; S. 266802.
 - [Nov11] Novotny, L.; van Hulst, N.: Antennas for light. In *Nature Photonics*, 2011, 5; S. 83–90.
 - [Pan56] Pancharatnam, S. Hrsg.: *Generalized theory of interference and its applications*. Springer, 1956.
 - [Ram08] Ramírez-Jiménez, F. J.; Castilla-Valdez, H.; Miranda, O.; Santos, E.: PIN Diode Detectors: AIP Conference Proceedings. AIP, 2008; S. 213–226.
 - [Roc06] Rockstuhl, C.; Lederer, F.; Etrich, C.; Zentgraf, T.; Kuhl, J.; Giessen, H.: On the reinterpretation of resonances in split-ring-resonators at normal incidence. In *Optics Express*, 2006, 14; S. 8827.
 - [Sal91] Saleh, B. E. A.; Teich, M. C.; Goodman, J. W.: *Fundamentals of Photonics*. John Wiley & Sons, Inc, New York, USA, 1991.
 - [Sch06] Schurig, D.; Mock, J. J.; Justice, B. J.; Cummer, S. A.; Pendry, J. B.; Starr, A. F.; Smith, D. R.: Metamaterial electromagnetic cloak at microwave frequencies. In *Science* (New York, N.Y.), 2006, 314; S. 977–980.
 - [Sha12] Sharma, B.; Frontiera, R. R.; Henry, A.-I.; Ringe, E.; van Duyne, R. P.: SERS. Materials, applications, and the future. In *Materials Today*, 2012, 15; S. 16–25.
 - [Smi11] Smith, B. C.: *Fundamentals of fourier transform infrared spectroscopy*, 2011.
 - [Sön02] Sönnichsen, C.; Franzl, T.; Wilk, T.; Plessen, G. von; Feldmann, J.: Plasmon resonances in large noble-metal clusters. In *New Journal of Physics*, 2002, 4; S. 93.
 - [Sou11] Soukoulis, C. M.; Wegener, M.: Past achievements and future challenges in the development of three-dimensional photonic metamaterials. In *Nature Photonics*, 2011, 5; S. 523–530.
 - [Ste15] Sterl, F.; Strohfeldt, N.; Walter, R.; Griessen, R.; Tittl, A.; Giessen, H.: Magnesium as Novel Material for Active Plasmonics in the Visible Wavelength Range. In *Nano letters*, 2015, 15; S. 7949–7955.
 - [Stu12] Stutzman, W. L.; Thiele, G. A.: *Antenna theory and design*. John Wiley & Sons, 2012.
 - [Thy12] Thyagarajan, K.; Rivier, S.; Lovera, A.; Martin, O. J. F.: Enhanced second-harmonic generation from double resonant plasmonic antennae. In *Optics express*, 2012, 20; S. 12860–12865.
 - [Tuo02] Tuovinen, H.; Kauranen, M.; Jefimovs, K.; Vahimaa, P.; Vallius, T.; Turunen, J.; Tkachenko, N. V.; Lemmetyinen, H.: Linear and second-order nonlinear optical properties of arrays of noncentrosymmetric gold nanoparticles. In *Journal of Nonlinear Optical Physics & Materials*, 2002, 11; S. 421–432.
 - [Tym15] Tymchenko, M.; Gomez-Diaz, J. S.; Lee, J.; Nookala, N.; Belkin, M. A.; Alù, A.: Gradient Nonlinear Pancharatnam-Berry Metasurfaces. In *Physical review letters*, 2015, 115; S. 207403.
 - [Via05] Vial, A.; Grimault, A.-S.; Macías, D.; Barchiesi, D.; La Chapelle, M. L. de: Improved analytical fit of gold dispersion. Application to the modeling of extinction spectra with a finite-difference time-domain method. In *Physical Review B*, 2005, 71; R11.

-
- [Wal13] Walsh, G. F.; Dal Negro, L.: Enhanced second harmonic generation by photonic-plasmonic Fano-type coupling in nanoplasmonic arrays. In *Nano letters*, 2013, 13; S. 3111–3117.
 - [Wal17] Walter, F.; Li, G.; Meier, C.; Zhang, S.; Zentgraf, T.: Ultrathin Nonlinear Metasurface for Optical Image Encoding. In *Nano letters*, 2017, 17; S. 3171–3175.
 - [Web17] Weber, N.; Protte, M.; Walter, F.; Georgi, P.; Zentgraf, T.; Meier, C.: Double resonant plasmonic nanoantennas for efficient second harmonic generation in zinc oxide. In *Physical Review B*, 2017, 95; S. 116.
 - [Wil07] Willets, K. A.; van Duyne, R. P.: Localized surface plasmon resonance spectroscopy and sensing. In *Annu. Rev. Phys. Chem.*, 2007, 58; S. 267–297.
 - [Wok81] Wokaun, A.; Bergman, J. G.; Heritage, J. P.; Glass, A. M.; Liao, P. F.; Olson, D. H.: Surface second-harmonic generation from metal island films and microlithographic structures. In *Physical Review B*, 1981, 24; S. 849–856.
 - [Xu07] Xu, T.; Jiao, X.; Zhang, G. P.; Blair, S.: Second-harmonic emission from sub-wavelength apertures: Effects of aperture symmetry and lattice arrangement. In *Optics express*, 2007, 15; S. 13894–13906.
 - [Ye16a] Ye, W.; Zeuner, F.; Li, X.; Reineke, B.; He, S.; Qiu, C.-W.; Liu, J.; Wang, Y.; Zhang, S.; Zentgraf, T.: Spin and wavelength multiplexed nonlinear metasurface holography. In *Nat. Commun. (Nature Communications)*, 2016, 7; S. 11930.
 - [Ye16b] Ye, W.; Li, X.; Liu, J.; Zhang, S.: Phenomenological modeling of nonlinear holograms based on metallic geometric metasurfaces. In *Opt. Express*, 2016, 24; S. 25805–25815.
 - [Yu11] Yu, N.; Genevet, P.; Kats, M. A.; Aieta, F.; Tetienne, J.-P.; Capasso, F.; Gaburro, Z.: Light propagation with phase discontinuities. Generalized laws of reflection and refraction. In *Science (New York, N.Y.)*, 2011, 334; S. 333–337.
 - [Yu14] Yu, N.; Capasso, F.: Flat optics with designer metasurfaces. In *Nature materials*, 2014, 13; S. 139–150.
 - [Zay05] Zayats, A. V.; Smolyaninov, I. I.; Maradudin, A. A.: Nano-optics of surface plasmon polaritons. In *Physics reports*, 2005, 408; S. 131–314.
 - [Zhe15] Zheng, G.; Mühlenbernd, H.; Kenney, M.; Li, G.; Zentgraf, T.; Zhang, S.: Metasurface holograms reaching 80% efficiency. In *Nature nanotechnology*, 2015, 10; S. 308–312.
 - [Zho13] Zhou, F.; Liu, Y.; Cai, W.: Plasmonic holographic imaging with V-shaped nanoantenna array. In *Optics express*, 2013, 21; S. 4348–4354.

6 LIST OF FIGURES

Figure 2.1: Imaginary ε_2 and real part ε_1 of the dielectric function of gold, silver and copper[Joh72.].....	7
Figure 2.2: Dielectric function of gold, calculated with the Drude-Sommerfeld model and the Drude model and experimental data(Johnson & Christi) [Via05].	8
Figure 2.3: Schematic figure of excitation of LSPP.	8
Figure 2.4: Dependence of the resonance to the form of a silver nanoparticle in vacuum. Every particle has got the same volume, in which the sphere has a diameter of 50 nm [Hae05].	9
Figure 2.5: Experimentally found line widths of resonances compared to the Mie theory [Sön02.]	11
Figure 2.6: Homogenous sphere placed in an electric field.	11
Figure 2.7: Absolute value and phase of the polarizability α of a metal nanoparticle with $d \ll \lambda$ dependent on the frequency of the incident field (here expressed in energy units). [Mai07]. $\varepsilon\omega$ is given here by a Drude fit to the dielectric function of silver[Joh72].	13
Figure 2.8: CST simulation of the electric field enhancement (a) of a gold nanoantennas with a length $l = 230 \text{ nm}$, a width $w = 60 \text{ nm}$ and a height of $h = 30 \text{ nm}$ on a glass substrate (b) of two nano antennas with the same size parameters as in (a) that are separated by a gap of 50 nm	14
Figure 2.9: Photon diagram for SHG. Destruction of two photons with frequency ω and simultaneous generation of a photon with the doubled frequency 2ω	15
Figure 2.10: Photon diagram for difference frequency generation.	17
Figure 2.11: Schematic of pump laser head used in the experiments of this work (Chameleon Ultra II).....	17
Figure 2.12: Design of double resonant antenna consisting of a long fundamental and a short SHG antenna with a small gap in between. Both are made of gold.	20
Figure 2.13: Schematic of the two different sample designs. On the left the gold antennas are put on a bulk ZnO substrate and on the right on a 230 nm thin ZnO layer on top of a silicone substrate.....	20
Figure 2.14: Experimental data of the measured and normalized extinction spectra over the wavelength and in dependence of the length of the fundamental antenna on bulk ZnO. For each array there appear two resonance, one for the fundamental antenna (which changes as the length changes) and one for the SHG antenna (which does not change) [Web17]	21

-
- Figure 2.15:** Experimental setup for the nonlinear measurements. The beam of the OPP passes a linear polarizer and is focused onto the antenna fields of the sample. A long pass filter in front of the sample filters out all the possible harmonic generation light, which is generated by other optical components beside the sample. Then a 20x objective collects the light, that is coupled into a spectrometer in the end..... 22
- Figure 2.16:** (a) Experimental data of the nonlinear measurements of antennas on a ZnO bulk substrate.[Web17] 23
- Figure 2.17:** Comparison of SHG intensities from single dipole nanorods to double resonant nanoantennas (black squares). The double resonant antennas increase the intensity by a factor of two due to the second resonance of the short antenna at around 700 nm. The corresponding Lorentz fit is depicted by the two solid lines [Web17]. 24
- Figure 2.18:** Design of the Pin diode and the nanoantennas (a) Cross section of the layers of the diode, the Si doped GaAs is the negative part of the diode and the C doped the positive one.(b) SEM image of the surface of the diode. The diode itself is 414 μm long and 324 μm wide. On the right a gold patch is visible which contacts the p-doped layer. On the left the sample is etched to the n-layer what enables contacting of the n-doped layer. The orange square in the middle of the diode depicts the nano antenna field, which is fabricated on top. (c) Exemplary SEM images of used gold nano antenna arrays (dipoles, L-shaped and split rings) (scale bar: 200 nm) 26
- Figure 2.19:** Measurement box opened and closed. The sample is placed in the middle of the box and the contacts on the sample are bonded to the contacts seen on the outside of the box. A whole in the lid enables the laser beam to illuminate the sample. 27
- Figure 2.20:** Measurement setup. With a half-wave plate and a linear polarizer, it is possible to control the power of the passing laser beam. A lens focuses the light onto the sample surface. A long pass filter ensures that only light with a wavelength above 1000 nm passes to the sample. An imaging system consisting of another lens and a CCD camera enables the user to align the laser on the antenna arrays. With a foldable mirror (dotted line), it is possible to measure the beam power..... 28
- Figure 2.21:** FTIR spectra of different antenna arrays on PIN diodes. (a) Spectrum of dipole antennas with light polarized along the long (x-direction) and short (y-direction) axis (b) spectrum of L-shaped antennas in both polarization directions along the arms (c) spectrum of split-ring antennas with linear polarized light in two directions..... 29
- Figure 2.22:** Power dependent measurement of L-shaped antennas. (a) at an incident wavelength of 1200 nm (b) at 1500 nm. 30
- Figure 2.23:** Fitted power dependent current measurements. (a) Current measurements of the L-shaped antennas on a PIN diode with linear polarized light in x-direction with fundamental wavelengths 1200 and 1500 nm fitted with $y = a \cdot x^b$ (b) The same measurements fitted with $y = ax + bx^2$ (c) Measurement with linear polarized visible light at 635 nm fitted linearly, which is performed at power intensities three orders of magnitudes lower than the measurements of (a) and (b) 31

Figure 2.24: Current measurement of local scan over PIN diode including contacts and antenna field (a) Scan from n-type contact to p-type contact (b) scan perpendicular to previous one.....	32
Figure 2.25: Current measurement scan over two diodes (blue areas). Only the diode on the right is contacted. The black areas are etched to the n-type GaAs. The grey areas on the blue diodes are gold contacts.....	33
Figure 2.26: Schematic of the EBL and lift off process for the fabrication of the C5 gold antennas on a glass/ITO substrate.....	40
Figure 2.27: SEM images of quadratically arranged C5 gold antennas on a glass/ITO substrate (a) antennas with a period of 1 μm in x- and y direction. (b) and (c) Close up of 240 nm long gold antennas with different arm width (45 and 65 nm).....	41
Figure 2.28: Schematic of the used FTIR setup, a combination of the Bruker Hyperion 1000 and the Vertex 70. The dotted lines refer to foldable mirrors, that serve to adjust the beam path.	42
Figure 2.29: Measured transmission spectra of C5 nano-antennas (a) made of gold with an arm width of 65 nm and (b) made of silver with an arm width of 80 nm on a glass/ITO substrate.....	43
Figure 2.30: Plasmon resonance wavelength over the arm length of C5 nano antennas with an arm width of 45 and 65 nm. The squares depict the experimentally determined results and the lines the corresponding linear fit.	44
Figure 2.31: Schematic experimental setup for the nonlinear characterization of the C5 nano antennas.....	45
Figure 2.32: Experimental data of the nonlinear characterization of C5 gold nano antennas with an arm length of 240 nm and width of 45 nm (a) for different excitation wavelengths (b) compared to the signal of the pure substrate and the lase itself.....	46
Figure 2.33: (a)Experimental data of the nonlinear characterization of C5 silver nano antennas with an arm length of 200 nm and width of 85 nm with left and right circular polarized light at an excitation wavelength of 1980 nm for different antenna arrangements (b) damaged silver antennas after an exposure with an excitement power of 100 mW.....	47
Figure 3.1: Schematics to derive the generalized Snell's law The structured metasurface introduces an abrupt phase shift [Yu14].	50
Figure 3.2: V-shaped antennas can be described by their arm length h and the enclosed vector Δ . They support symmetric and antisymmetric modes, which can be excited by components of the incident electrical field along the unit vector axis s and a [Yu11].h	51
Figure 3.3: Design of v-shaped antennas made of gold and Mg. (a) In air the complete antenna behaves like metal, but putting it into a hydrogen environment, the Mg part of the	

antenna becomes dielectric and only the here shown short antenna stays actively plasmonic. This leads to a phase shift of the scattered light of $\pi/2$. (b) Side view of antenna. Short antenna is made of 2 nm Cr adhesion layer and 50 nm Au. Dynamic part of the antenna consist of a 2 nm Ti adhesion layer, 50 nm Mg, another 2 nm Ti layer and 5 nm of Pd. The Ti layer between Mg and Pd prevents the two from alloying (c) SEM image of short Au antennas with Mg extension.....	52
Figure 3.4: Flow chart of the used iterative algorithm to simulate the metasurface and the generated hologram.	53
Figure 3.5: Real and imaginary part of the dielectric function of magnesium.	54
Figure 3.6: Simulation of (a) the amplitude of v-shaped antennas with different length L and angles θ (b) of the phase of the same antennas (c) Designs for short and long antennas with different geometric P-B phases from π to $-\pi/4$ and $\pi + \pi/2$ to $-\pi/4 + \pi/2$, respectively.....	55
Figure 3.7: Funcionality principle of metasurface. (a) pure gold short antennas generate a hologram that depicts a horse (b) additional Mg at the ends of the antenna adds a phase of $+\pi/2$ and the hologram image changes to a deer (c) Putting the metasurface in a hydrogen turns the Mg into MgH_2 with dielectric properties. Only the short gold part of the antenna behaves plasmonic and the hologram depicts a horse again. ..	56
Figure 3.8: Transmission spectra of hologram metasurfaces, one consisting of hybrid antennas made of Mg and Au, the other only of pure Au antennas, both fabricated on a glass/ITO substrate.	57
Figure 3.9: Hologram measurement setup. x -polarized light is focused onto the sample that resides in a gas cell. The scattered light then passes another linear polarizer, through which only y -polarized light can pass. On a screen behind the polarizer the image occurs and is captured by an IR camera. An additional hinged mirror behind the sample, enables an imaging setup to locate the laser beam spot on the sample.....	58
Figure 3.10: Images of holograms of two different metasurfaces (a) Metasurface only consisting of short gold antennas, which generate a hologram of a horse. (b) Active hologram of metasurface of hybrid antennas made of gold and magnesium in air. (c) Hologram after the hybrid metasurface of (b) resided 25 min in hydrogen.	58
Figure 3.11: Simulation of generated hologram by a metasurface with hybrid antennas for different additional phases caused by improper alignment of the two parts of the hybrid antennas. From top middle to bottom right the additional phase increases from $0,2 \cdot 2\pi$ to $0,5 \cdot 2\pi$. On the top left, the simulation with no additional phase is shown.....	59
Figure 3.12: Images of the hologram taken for four different incident wavelength (1300, 1400, 1490 and 1540 nm) The metasurface works broadband , but due to the scattering properties and the resonance of the nanoantennas, the hologram appears in different sizes and intensities	60

Figure 3.13: P-B phase depicted on a Poincaré sphere.	62
Figure 3.14: C3 antenna in local (x', y') and laboratory (x, y) frame that is illuminated with circular polarized light $(k\omega, \sigma)$ and generates SHG with the inverse circular polarization state $(k2\omega, -\sigma)$ [Li17].	64
Figure 3.15: Working principle of the nonlinear metasurface under various illumination conditions (a) Under illumination with incoherent and unpolarized white light no image can be seen (b) Using circularly polarized NIR light at 1240 nm to illuminate the metasurface, the encoded image with the characters “META” appear at the SHG wavelength 620 nm (c) Illuminating the sample with light at the SHG wavelength of the NIR light at 620 nm, the encoded image cannot be read out anymore.	65
Figure 3.16: Design of the meta-atoms. (a) Schematic of the meta-atoms with a C3 symmetry. The metasurface is arranged periodically with a periode of 500 nm in x - and y -direction. The arms of the meta-atom ware 165 nm long, 60 nm wide and 30 nm. (b) The rotation angle θ of two neighboring meta-atoms (one virtual pixel) varies from 0° to 60° in steps of 7,5°. (c) SEM images of fabricated meta-atoms with various rotation angles (scale bar: 200 nm).	66
Figure 3.17: Linear optical properties of the metasurfaces. (a) Measured transmission spectrum of metasurface made of C3 meta-atoms with unpolarized light. The dip at a wavelength of 1240 nm corresponds to the localized plasmon resonance of the meta-atoms. The marked lines show the spectral position of the used fundamental laser wavelength and the corresponding SHG. (b) Measured transmission of metasurfaces with varying orientation angles of the meta-atoms from 0° to 30° . .	67
Figure 3.18: Setup for SHG transmission measurement	68
Figure 3.19: SHG intensities of the metasurfaces. (a) Angle dependent SHG measurement for excitation with a fundamental wavelength of 1250 nm for various circular polarization schemes. In the legend the first letter describes the polarization state of the fundamental wave and the second letter the on for the SHG signal. (L, left circular polarization; R, right circular polarization). The red line shows the expected behavior of the SHG intensity, due to interference effects. (b) Angle dependent SHG intensity for linear polarized light with a fundamental wavelength of 1250 nm and the expected behavior (red line) (c) Measured angle dependent right circular polarized SHG intensity for a left circular polarized fundamental wave at four different wavelengths from 1250 to 1400 nm.	69
Figure 3.20: Schematic and real space images of the metasurface. (a) Spatial map of the orientation angle θ of the meta-atom pairs. The color red corresponds to an angle $\theta = 30^\circ$ between the two C3 structures, whereas blue indicates $\theta = 0^\circ$. (b) Experimentally measured image at the SHG wavelength for an excitation at the resonance wavelength of 1250 nm, showing the characters “META” (c) obtained image at the fundamental pump wavelength (1250 nm), showing no characters. (d) Image at the SHG wavelength each letter consists of meta-atom pairs with a different orientation angle $\theta = 0^\circ; 7,5^\circ; 15^\circ, 22,5^\circ$ respectively, which leads to an intensity modulation.	70

Figure 3.21: Inverted real space SHG images (a) Measured real space SHG image for the inverse design of Figure 4a. Now $\theta=0^\circ$ is used for the background and the character is made with $\theta=30^\circ$. (b) Measured real space SHG image for the inverse design of Figure 4a.	71
--	----

7 LIST OF TABLES

- Table 2.1:** Presence (+) or absence (0) for 32 crystal classes under illumination with linear polarized light [Bha72.]. “X” signifies elliptical polarization. After the harmonics of the order $p + 1$ results repeat themselves.36
- Table 2.2:** Presence (same polarizaiton “+”, opposite polarization “−”) or absence (0) for 32 crystal classes under illumination with circular polarized light [Bha72]. “X” signifies elliptical polarization. After the harmonics of the order $p + 1$ results repeat themselves.....38
- Table 2.3:** Possible harmonic generations for different antennas symmetries under illumination with circular polarized light [Li15].39
- Table 3.1:** Lengths for short and long antennas for antennas that generate different phase shifts. The numbers 1 - 8 correspond to the antennas and phases shown in Figure 3.5. The angle θ needs to be unchanged for short and long antennas, as this is given by the design of the metasurface.....55

8 LIST OF SCIENTIFIC CONTRIBUTIONS

- D. A. Gollmer, **F. Walter**, C. Lorch, J. Novak, R. Banerje, J. Dieterle, G. Santoro, F. Schreiber, D. P. Kern, M. Fleischer, *Fabrication and characterization of combined metallic nanogratings and ITO electrodes for organic photovoltaic cells*, Microelectronic Engineering 119 (2014) 122–126
- **F. Walter**, G. Li, C. Meier, S. Zhang, T. Zentgraf., *Ultrathin Nonlinear Metasurface for Optical Image Encoding*, Nano letters, 17 (2017) 3171–3175.
- N. Weber, M. Protte, **F. Walter**, P. Georgi, T. Zentgraf, C. Meier, *Double resonant plasmonic nanoantennas for efficient second harmonic generation in zinc oxide*, Physical Review B, 95; (2017) 116-120

Outstanding:

- L. Huang, **F. Walter**, T. Zentgraf, *Binary Switchable phase holography with hybrid v-shaped nanoantennas*

Conference Contributions:

- *Fabrication and investigation of plasmonic nano gratings for photovoltaic devices*, **F. Walter**, D. A. Gollmer, C. Lorch, J. Novak, F. Schreiber, D. P. Kern, M. Fleischer, DPG Spring Meeting, Regensburg, 2013
- *Plasmonic metasurface enhanced non-linear optical effects in LiNbO₃ optical waveguides*, **F. Walter**, A. Hildebrandt, N. Weber, J. Förstner, C. Meier, T. Zentgraf, DPG Spring Meeting, Regensburg, 2016
- *Ultrathin nonlinear metasurface for optical image encoding*, **F. Walter**, G. Li, C. Meier, S. Zhang, T. Zentgraf, CLEO/Europe-EQEC, München, 2017
- *Ultrathin nonlinear metasurface for optical image encoding*, **F. Walter**, G. Li, T. Zentgraf, DPG Spring Meeting, Berlin, 2018

DANKSAGUNG

Ich möchte mich bei folgenden Personen bedanken ohne deren Hilfe diese Arbeit nicht möglich gewesen wäre:

Bei Prof. Dr. Thomas Zentgraf für die Möglichkeit der Promotion und die hervorragende Betreuung während der letzten vier Jahre.

Bei meinen Arbeits- und Bürokollegen Bernhard Reineke, Daniel Frese, Franziska Zeuner, Christian Schlickriede, Holger Mühlenbernd, Florian Spreyer und Philip Georgi für eine großartige Zusammenarbeit, wertvolle Tipps und viele lustige Abende.

Auch bei der restlichen Arbeitsgruppe Zentgraf für die sehr entspannte Arbeitsatmosphäre.

Bei Nils Meier für die endlosen Stunden zusammen im Optiklabor und bei André Hildebrand für die dafür notwendigen Simulationen.

Bei Linling Huang und ihrem Team für die bereitgestellten Simulationen zur Holographie.

Bei meiner Familie, meinem Partner und meinen Freunden für die Unterstützung während der gesamten Schaffensphase.